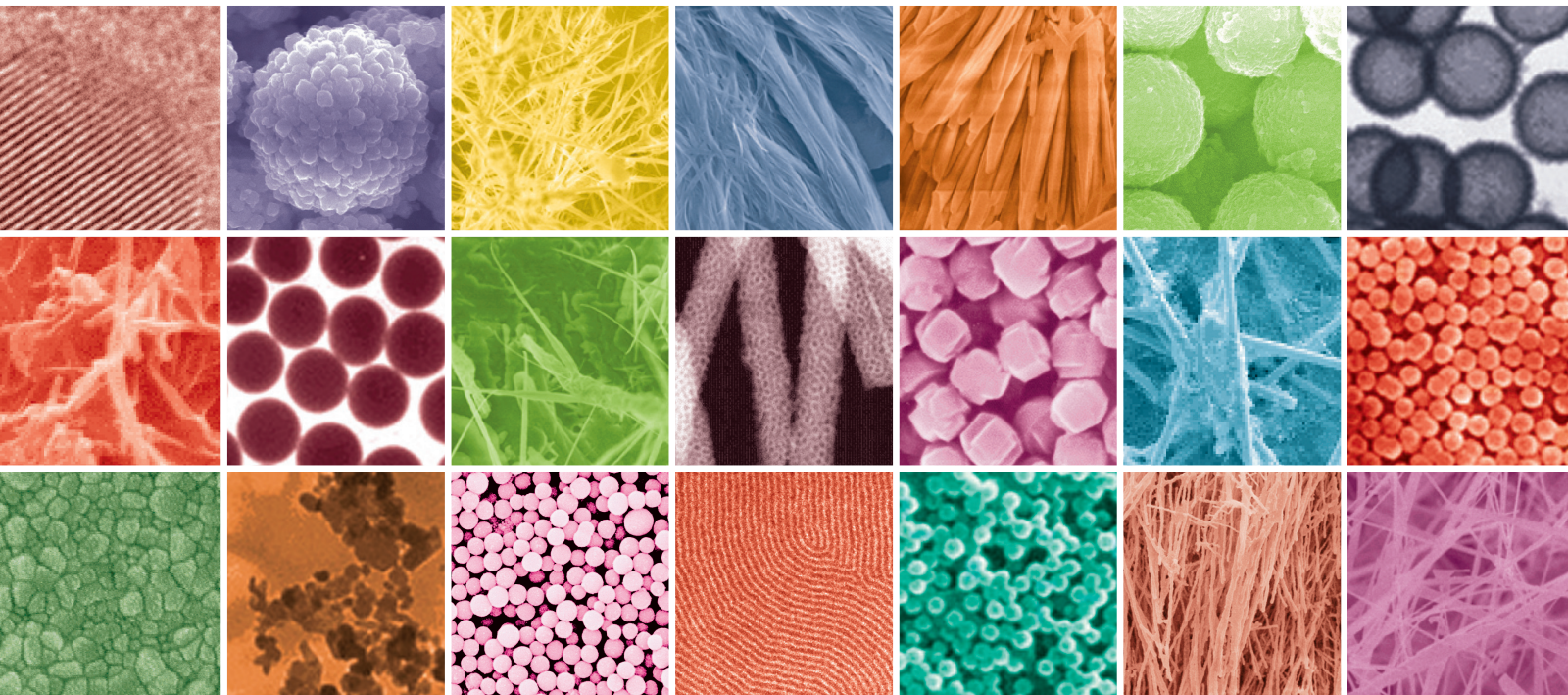


Polymer Nanocomposite Processing, Characterization, and Applications 2013

Guest Editors: Gaurav Mago, Suprakas Sinha Ray, Meisha L. Shofner,
Shanfeng Wang, and Jin Zhang





**Polymer Nanocomposite Processing,
Characterization, and Applications 2013**

Journal of Nanomaterials

**Polymer Nanocomposite Processing,
Characterization, and Applications 2013**

Guest Editors: Gaurav Mago, Suprakas Sinha Ray,
Meisha L. Shofner, Shanfeng Wang, and Jin Zhang



Copyright © 2014 Hindawi Publishing Corporation. All rights reserved.

This is a special issue published in "Journal of Nanomaterials." All articles are open access articles distributed under the Creative Commons Attribution License, which permits unrestricted use, distribution, and reproduction in any medium, provided the original work is properly cited.

Editorial Board

Katerina E. Aifantis, Greece
Nageh K. Allam, USA
Margarida Amaral, Portugal
Xuedong Bai, China
Lavinia Balan, France
Enrico Bergamaschi, Italy
Theodorian Borca-Tasciuc, USA
C. Jeffrey Brinker, USA
Christian Brosseau, France
Xuebo Cao, China
Shafiq Chowdhury, USA
Kwang-Leong Choy, UK
Cui ChunXiang, China
M. A. Correa-Duarte, Spain
Shadi A. Dayeh, USA
Claude Estourns, France
Alan Fuchs, USA
Lian Gao, China
Russell E. Gorga, USA
Hongchen Chen Gu, China
Mustafa O. Guler, Turkey
John Zhanhu Guo, USA
Smrati Gupta, Germany
Michael Harris, USA
Zhongkui Hong, China
Michael Hu, USA
David Hui, USA
Y.-K. Jeong, Republic of Korea
Sheng-Rui Jian, Taiwan
Wanqin Jin, China
Rakesh K. Joshi, UK
Zhenhui Kang, China
Fathallah Karimzadeh, Iran
Alireza Khataee, Iran
Do Kyung Kim, Republic of Korea

Alan K. T. Lau, Hong Kong
Burtrand Lee, USA
Benxia Li, China
Jun Li, Singapore
Xing-Jie Liang, China
Shijun Liao, China
Gong Ru Lin, Taiwan
J. -Y. Liu, USA
Tianxi Liu, China
Songwei Lu, USA
Daniel Lu, China
Jue Lu, USA
Ed Ma, USA
Gaurav Mago, USA
Santanu K. Maiti, India
Sanjay R. Mathur, Germany
Vikas Mittal, United Arab Emirates
Weihai Ni, Germany
Sherine Obare, USA
Atsuto Okamoto, Japan
Abdelwahab Omri, Canada
Edward Andrew Payzant, USA
Kui-Qing Peng, China
Anukorn Phuruangrat, Thailand
Mahendra Rai, India
Suprakas Sinha Ray, South Africa
Ugur Serincan, Turkey
Huaiyu Shao, Japan
Donglu Shi, USA
Vladimir Sivakov, Germany
Marinella Striccoli, Italy
Bohua Sun, South Africa
Saikat Talapatra, USA
Nairong Tao, China
Titipun Thongtem, Thailand

Somchai Thongtem, Thailand
Alexander Tolmachev, Ukraine
Valeri P. Tolstoy, Russia
Tsung-Yen Tsai, Taiwan
Takuya Tsuzuki, Australia
Raquel Verdejo, Spain
Mat U. Wahit, Malaysia
Shiren Wang, USA
Yong Wang, USA
Ruiping Wang, Canada
Cheng Wang, China
Zhenbo Wang, China
Jinquan Wei, China
Ching-Ping Wong, Hong Kong
Xingcai Wu, China
Guodong Xia, Hong Kong
Zhi Li Xiao, USA
Ping Xiao, UK
Shuangxi Xing, China
Yangchuan Xing, USA
N. Xu, China
Doron Yadlovker, Israel
Yingkui Yang, China
Khaled Youssef, USA
Kui Yu, Canada
William W. Yu, USA
Haibo Zeng, China
Tianyou Zhai, Japan
Renyun Zhang, Sweden
Bin Zhang, China
Yanbao Zhao, China
Lianxi Zheng, Singapore
Chunyi Zhi, Hong Kong

Contents

Polymer Nanocomposite Processing, Characterization, and Applications 2013, Gaurav Mago, Suprakas Sinha Ray, Meisha L. Shofner, Shanfeng Wang, and Jin Zhang
Volume 2014, Article ID 403492, 2 pages

Three-Phase Carbon Fiber Amine Functionalized Carbon Nanotubes Epoxy Composite: Processing, Characterisation, and Multiscale Modeling, Kamal Sharma and Mukul Shukla
Volume 2014, Article ID 837492, 10 pages

Triple-Component Drug-Loaded Nanocomposites Prepared Using a Modified Coaxial Electrospinning, Wei Qian, Deng-Guang Yu, Ying Li, Xiao-Yan Li, Yao-Zu Liao, and Xia Wang
Volume 2013, Article ID 826471, 7 pages

Mechanical Properties of Natural Rubber Nanocomposites Filled with Thermally Treated Attapulgit, Jihu Wang and Dajun Chen
Volume 2013, Article ID 496584, 11 pages

Ultrasonication Technique: A Method for Dispersing Nanoclay in Wood Adhesives, Alireza Kaboorani, Bernard Riedl, and Pierre Blanchet
Volume 2013, Article ID 341897, 9 pages

Polyethylene/Clay Nanocomposites Produced by *In Situ* Polymerization with Zirconocene/MAO Catalyst, Pimpatima Panupakorn, Ekrachan Chaichana, Piyasan Prasertthdam, and Bunjerd Jongsomjit
Volume 2013, Article ID 154874, 9 pages

Effects of Chitosan Alkali Pretreatment on the Preparation of Electrospun PCL/Chitosan Blend Nanofibrous Scaffolds for Tissue Engineering Application, Fatemeh Roozbahani, Naznin Sultana, Ahmad Fauzi Ismail, and Hamed Nouparvar
Volume 2013, Article ID 641502, 6 pages

Editorial

Polymer Nanocomposite Processing, Characterization, and Applications 2013

Gaurav Mago,¹ Suprakas Sinha Ray,² Meisha L. Shofner,³ Shanfeng Wang,⁴ and Jin Zhang⁵

¹ *Lubrizol Advanced Materials, Inc., Avon Lake, OH 44012, USA*

² *DST/CSIR Nanotechnology Innovation Centre, National Centre for Nano-Structured Materials, Pretoria 0001, South Africa*

³ *School of Materials Science and Engineering, Georgia Institute of Technology, Atlanta, GA 30332, USA*

⁴ *Department of Materials Science and Engineering, The University of Tennessee, Knoxville, TN 37996, USA*

⁵ *Department of Chemical and Biochemical Engineering, University of Western Ontario, London, ON, Canada N6A 5B9*

Correspondence should be addressed to Gaurav Mago; gauravmago2001@gmail.com

Received 23 December 2013; Accepted 23 December 2013; Published 26 February 2014

Copyright © 2014 Gaurav Mago et al. This is an open access article distributed under the Creative Commons Attribution License, which permits unrestricted use, distribution, and reproduction in any medium, provided the original work is properly cited.

Nanoparticles, such as carbon nanotubes, nanoclays, and graphenes, are widely used in the polymer nanocomposites to alter the chemical, mechanical, electrical, optical, and thermal properties. However, a number of critical issues need to be addressed before the full potential of polymer nanocomposites can actually be realized. The improvements in mechanical, thermal, electrical, and rheological properties of polymers by addition of nanoparticles depend upon a number of factors, such as processing technique, interfacial interaction between nanoparticles and host polymers, and state of nanoparticle dispersion. While a number of advances have recently been made in the area of polymer nanocomposites, the studies on understanding of the effects of processing parameters on the structure, morphology, and functional properties of polymer nanocomposites are deficient. The relationships between the structural distributions and the ultimate properties of the polymer nanocomposites also need to be elucidated. There is a need for better characterization techniques to quantify the concentrations and distributions of nanoparticles as well as to assess the nature of the interface between the polymer and nanoparticles. Also, there is a critical need for the development of better models with the ability to predict the mechanical properties of the polymer nanocomposites as functions of relevant factors including nanoparticle orientation, the type of functional groups, and the molecular weight of polymer chain.

Considering the challenges in the area of development of adequate methods of processing for nanocomposites, this special issue was devoted to the emerging polymer nanocomposite processing techniques. Also, this special issue intended to cover the entire range of basic and applied materials research focusing on rheological characterization, nanoparticle dispersion, and functional properties of polymer nanocomposites for sensors, actuators, and other multifunctional applications. This special issue with a total of six papers covers a wide range of areas related to fabrication of triple-component drug-loaded nanocomposites using a modified coaxial electrospinning; three-phase carbon fiber amine functionalized carbon nanotubes epoxy composite; processing, characterization, and multiscale modeling; use of ultrasonication technique for dispersing nanoclay in wood adhesives; effect of chitosan alkali pretreatment on the preparation of electrospun poly(ϵ -caprolactone)/chitosan blend nanofibrous scaffolds for tissue engineering application; polyethylene/clay nanocomposites produced by in situ polymerization with zirconocene/methylaluminoxane catalyst; and, finally, mechanical properties of natural rubber nanocomposites filled with thermally treated attapulgite.

It is hoped that this special issue will help readers with a wide range of backgrounds to understand the impact of various processing methods as well as nanoparticles on the polymer nanocomposite properties and their multifunctional applications.

Acknowledgments

The editors would like to acknowledge the invited and contributing authors and reviewers.

*Gaurav Mago
Suprakash Sinha Ray
Meisha L. Shofner
Shanfeng Wang
Jin Zhang*

Research Article

Three-Phase Carbon Fiber Amine Functionalized Carbon Nanotubes Epoxy Composite: Processing, Characterisation, and Multiscale Modeling

Kamal Sharma¹ and Mukul Shukla^{1,2}

¹ Mechanical Engineering Department, Motilal Nehru National Institute of Technology, Allahabad, Uttar Pradesh 211004, India

² Department of Mechanical Engineering Technology, University of Johannesburg, Room 4131, B3 Lab 208, John Orr Building, Beit Street, Doornfontein, P.O. Box 17011, Johannesburg 2028, South Africa

Correspondence should be addressed to Kamal Sharma; sharmakamal1978@gmail.com

Received 19 July 2013; Revised 7 December 2013; Accepted 15 December 2013; Published 2 February 2014

Academic Editor: Gaurav Mago

Copyright © 2014 K. Sharma and M. Shukla. This is an open access article distributed under the Creative Commons Attribution License, which permits unrestricted use, distribution, and reproduction in any medium, provided the original work is properly cited.

The present paper discusses the key issues of carbon nanotube (CNT) dispersion and effect of functionalisation on the mechanical properties of multiscale carbon epoxy composites. In this study, CNTs were added in epoxy matrix and further reinforced with carbon fibres. Predetermined amounts of optimally amine functionalised CNTs were dispersed in epoxy matrix, and unidirectional carbon fiber laminates were produced. The effect of the presence of CNTs (1.0 wt%) in the resin was reflected by pronounced increase in Young's modulus, inter-laminar shear strength, and flexural modulus by 51.46%, 39.62%, and 38.04%, respectively. However, 1.5 wt% CNT loading in epoxy resin decreased the overall properties of the three-phase composites. A combination of Halpin-Tsai equations and micromechanics modeling approach was also used to evaluate the mechanical properties of multiscale composites and the differences between the predicted and experimental values are reported. These multiscale composites are likely to be used for potential missile and aerospace structural applications.

1. Introduction

The discovery of carbon nanotubes (CNTs) of exceptional mechanical properties combined with low density has led to their novel use as a reinforcing nanofiller in composite materials [1, 2]. The high strength and stiffness of CNTs leads to improved tensile, shear, and flexural properties of multiscale composites [3]. The effectiveness of CNT reinforcement can be proven by the fact that even smaller amounts (<5 wt%) of loading of CNTs result in significant improvements in their mechanical and physical properties. A number of studies have been performed on developing high-performance CNT/polymer composites containing CNTs ranging between 0.1 and 5 wt% [4, 5]. However, the homogeneous and consistent dispersion of CNTs in different polymers is found to be a major difficulty, which often degrades the properties of composites. Another important issue is the poor interfacial adhesion, which is mainly responsible for efficient load

transfer from the CNTs to the matrix [6]. Experimental determination of the interfacial strength of CNT/polymer composites still remains a challenge. Zhang et al. [7] reported that the interfacial shear strength of an epoxy composite reinforced using a CNT/carbon fibre (T300) hybrid is as high as 106.55 MPa, almost 150% higher than that of non-CNT reinforced composites. Limited success has been achieved on the experimental side however; reasonable success has been obtained in theoretical predictions [6]. The interfacial shear stress transfer from the matrix to the reinforcement takes place via the interface, which can be largely improved by chemical functionalisation of the CNT surfaces [8].

Multiscale composites (with CNTs, fibres, and matrix) have drawn significant attention in the field of advanced, high-performance materials. Only a limited number of studies involving three-phase composites have been reported [9–13]. Gojny et al. [9] reported an increase in interlaminar shear strength (ILSS) by 20% due to the amine functionalisation of

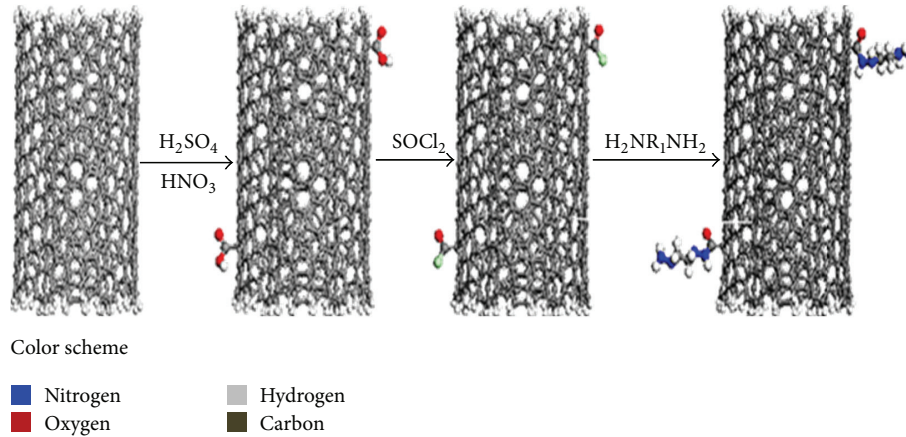


FIGURE 1: Procedure used for functionalisation of MWCNTs.

CNT surfaces. Zhihang et al. [10] reported a 30% increase in ILSS by incorporating CNTs perpendicular to the fibre surface. Thostenson et al. [12] introduced the idea of growing CNTs on the surface of carbon fibres to increase adhesion to the matrix, which was later confirmed experimentally by De Riccardis et al. [13]. Godara et al. [14] conducted tensile testing of unidirectional laminates reinforced with carbon fibre in different directions. They observed a systematic decrease in longitudinal tensile strength by up to 20% in comparison to the laminates produced using pristine CNTs.

An equally exciting, recent, research area is modeling of CNT composites and multiscale (microscale fibres and nanoscale tubes) composites to predict the mechanical properties and behaviour. Currently, for CNT/polymer composites, the Halpin-Tsai equations [15–17] and the Mori-Tanaka method [18–21] are being widely used. Qian et al. [17] considered multiwalled CNTs (MWCNTs)/polystyrene composite films as randomly oriented discontinuous fibre lamina and calculated the tensile modulus of the composite using the Halpin-Tsai equations. Yeh et al. [22] proposed modifying the Halpin-Tsai equations to evaluate the tensile modulus and strength of MWCNT/phenolic composites by adopting orientation and exponential shape factors. Kim et al. [23] obtained the tensile modulus of three-phase woven laminates theoretically as well as experimentally. They found that the theoretical tensile modulus is larger than the measured value by 11.8%; this discrepancy is attributed due to the assumptions made in the theoretical models.

The present research aimed to enhance the understanding of the practical and theoretical aspects related to the processing of three-phase multiscale CNT composites and the influence of the addition of CNTs. The objective of the present work is to obtain a homogeneous dispersion of amine functionalised multiwalled carbon nanotubes (AFMWCNTs) into epoxy, as well as producing a strong interface between them by means of functionalisation of CNTs. Also, several dispersion techniques have been tested in order to get a more homogenous dispersion. This study is also focused on evaluating the effect of CNT functionalisation on mechanical properties of multiscale composites.

TABLE 1: Types of fabricated three-phase composites.

Code	CNT wt%	Description
CFEC	0	Carbon fibre/epoxy composite
1CNTCFEC	0.25	0.25 wt% CNT three-phase composites
2CNTCFEC	0.5	0.5 wt% CNT three-phase composites
3CNTCFEC	1.0	1.0 wt% CNT three-phase composites
4CNTCFEC	1.5	1.5 wt% CNT three-phase composites

2. Experimental

2.1. Materials. AFMWCNTs (diameter: 20–30 nm; length: 20–30 μm ; density: 1.8 g/cc; Young's modulus: 400 GPa) were obtained from Chemapol Industries (Mumbai, India). Diethylamine is used for functionalisation in 7.2 : 120 weight ratios of resin. The selection of Diethyl group for amine functionalisation was based on the results of Gojny et al. and Shen et al. [3, 24]. Shen et al. [24] concluded that the Diethyl group of amines is the most effective in enhancing the mechanical properties of CNT epoxy composites. The procedure used for functionalisation of MWCNTs and their chemical structure functionalised has been shown in Figure 1. The Araldite LY 556 epoxy resin obtained from Chemapol Industries (Mumbai, India) has been cured with the aromatic anhydride hardener HY5200. The glass transition temperature of the neat resin was 130–141°C (Chemapol Industries, Mumbai, India) and density was 1.15–1.20 g/cc. Different amounts (0.25, 0.50, 1.0, and 1.50 wt%) of AFMWCNTs were dispersed in epoxy matrix using an advanced ultrasonic probe sonication method. The details of the sonicator used in this study have been presented in the next section. Finally the three-phase multiscale composites were prepared by the hand layup technique for 60% carbon fibre and for different CNT loading, as listed in Table 1. Carbon fibre T700 grade (Toray Co., USA) containing 600 filaments per tow was used in this study. T700 fibre has a high tensile strength (approximately 5000 MPa) with a standard modulus of 230 GPa.

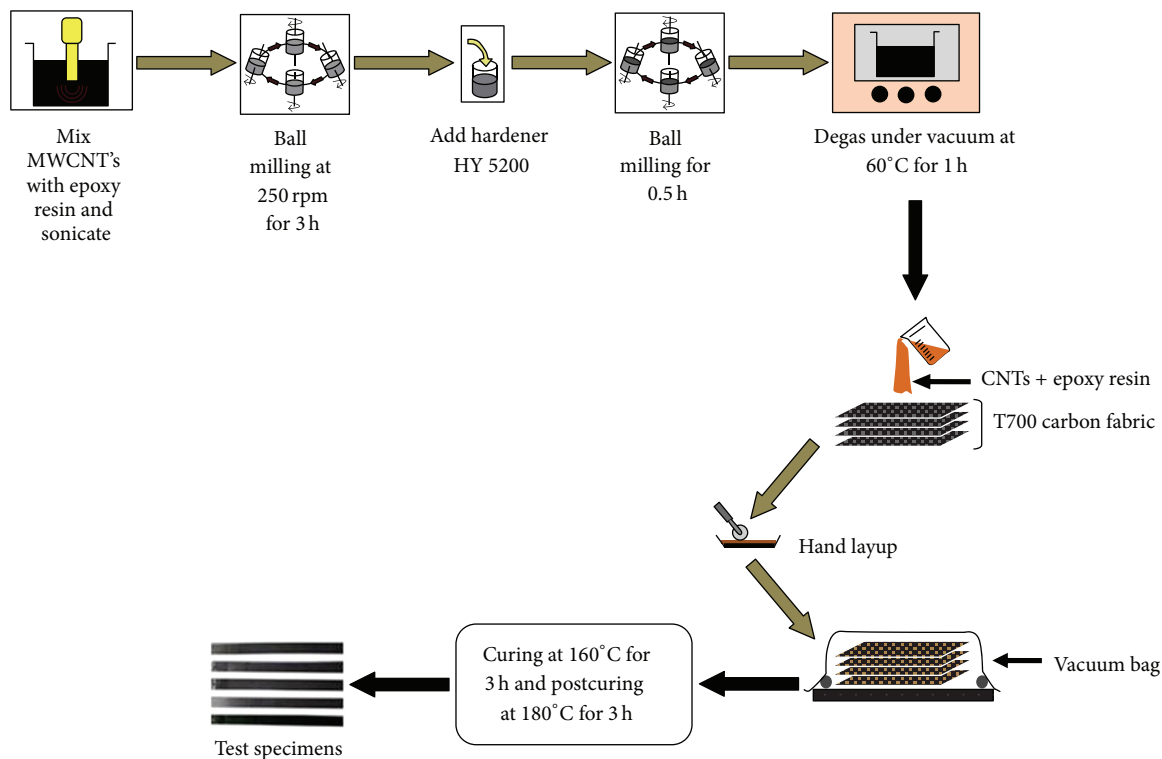


FIGURE 2: Fabrication process of carbon fibre/CNT/epoxy three-phase composites.

2.2. Fabrication Process. Precalculated amounts of AFMWCNTs and curing agent were weighed and mixed together with epoxy in a beaker, such that the weight fraction of CNTs was 0.3% with respect to resin and curing agent. Horn Sonicator 3000 ultrasonic probe sonication was employed for 18 min to uniformly disperse the CNTs in the curing agent. Horn Sonicator 3000 has 3.2 mm tip diameter, 100 watts maximum power output, and 22.5 kHz operating frequency. Following this, the epicure AFMWCNT mixture was combined with epoxy and the three component mixture was ball milled at 250 rpm for 3 h for homogeneous dispersion of AFMWCNTs. Next, the hardener HY5200 was mixed and the mixture was further ball milled for 30 min at 250 rpm. The mixture was then degassed in a vacuum oven for 1 h at 60°C and subsequently preheated before spreading uniformly on the carbon fibre, using the hand layup process. Once the carbon fibre had been infiltrated with the LY556/epicure W/MWCNT mixture, it was allowed to cure at 110°C for 2 h and post cure at 180°C for 3 h in a vacuum oven. In this study, the following five carbon fibre reinforced laminates were fabricated: one for neat resin and four with 0.25, 0.50, 1.0, and 1.50 wt% AFMWCNTs dispersed. A schematic illustration of the process used for the fabrication of carbon fibre/CNT/epoxy three-phase composites has been shown in Figure 2. Finally, six samples each were cut in the dimensions set up by the ASTM D 3039 standard for tensile tests and the ASTM D 790 standard for flexural tests.

2.3. Sample Characterisation

2.3.1. FTIR Spectroscopy. A Fourier transform infrared (FTIR) spectrum was recorded using the SHIMADZU, Kyoto, Japan, IRAffinity-1 spectrometer with the range of 2100 cm^{-1} peak to peak at the maximum resolution of 0.5 cm^{-1} . The IRAffinity-1 offers the highest S/N ratio in its class (30,000:1, 1-minute accumulation neighbourhood of 2100 cm^{-1} peak to peak) and compact dimensions. The interferometer is continuously optimized by a dynamic alignment mechanism and a built-in auto dryer.

2.3.2. Mechanical Testing. Carbon fibre/CNT/epoxy composites test specimens were cut in the desired dimensions (Figure 3(a)) out of the laminate panel (Figure 3(b)). The sample dimensions were $180 \times 10.30 \times 1.44$ mm. Both pure CF-epoxy and three-phase (CNT reinforced) composites were tested according to the ASTM D 3039 standard for tensile properties. A table top model STM series Universal Testing Machine of 50 kN load cell (United Calibration Corporation) was used for tensile testing. The crosshead speed was set at 3.5 $\text{mm}\cdot\text{min}^{-1}$. Flexural modulus tests were also conducted according to the ASTM D 790 standard on the same machine at a crosshead speed of 10 $\text{mm}\cdot\text{min}^{-1}$ at room temperature, with the sample span of 30 mm. The average values of six test results have been reported here.

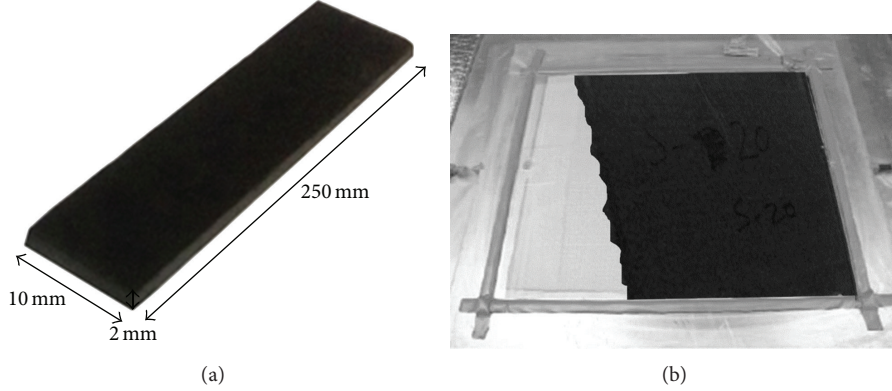


FIGURE 3: (a) Test specimen cut in the desired dimensions from (b) laminate panel sheets.

Morphology of the fractured composite samples surfaces was observed under the JEOL JXA-8100 scanning electron microscope (SEM) in order to investigate the fibre-matrix interface. Further detailed micro- and nanostructural study was carried out using a transmission electron microscope (TEM) (CM 200 from Philips and Tecnai G² from FEI) with LaB₆ filament operated at 200 kV. The high resolution imaging was done using the JEOL TEM equipped with a field emission gun operated at 200 kV, capable of providing a point to point resolution. The TEM image for aligned bundles and isolated AFMWCNTs is shown in Figures 4(a) and 4(b), respectively. A fine powder was prepared from the AFMWCNTs sample which was subsequently added to methanol and kept in an ultrasonic bath for 15 min to obtain a uniformly dispersed solution. For carrying out the TEM analysis a small drop from this solution was taken in a capillary tube and poured onto a 300 mesh carbon coated grid of 3 mm diameter and then dried under IR lamp.

2.4. Micromechanics Modeling. To predict the mechanical properties of three-phase composites, the Halpin-Tsai equations and theory of micromechanics were applied in hierarchy. First, the Halpin-Tsai equations were applied to calculate the mechanical properties of two-phase CNT/epoxy nanocomposites. The two-phase nanocomposite properties were then applied to compute the mechanical properties of three-phase multiscale composites using the micromechanics rule of mixtures. In the rule of mixtures, the properties of CNT/epoxy composites were used as the properties of the matrix.

2.4.1. Halpin-Tsai Equations. One of the primary requirements for obtaining the mechanical properties of three-phase multiscale composites was to compute the material properties of the CNT/epoxy composite. In this study, the results were analyzed with the Halpin-Tsai model for randomly oriented long fibres. This model was developed by Halpin and Kardos [15] to account for the Young's modulus of composites based on polymer matrices filled with particles of high aspect ratio. It produces favourable interactions between the matrix and the filler as well as good filler distribution.

The selected Halpin-Tsai equation, correlating the relative Young's modulus of a composite to the morphological and mechanical properties of its constituents, and the specific geometric characteristics of AFMWCNTs are represented as follows:

$$\begin{aligned}
 E_c = & \frac{3}{8} \left[1 + 2 \left\{ \frac{l}{d} \right\} \left\{ \frac{(E_{CNT}/E_{EP}) - (d/4t)}{(E_{CNT}/E_{EP}) + (l/2t)} \right\} \varphi_{CNT} \right] \\
 & \times \left[1 - \left\{ \frac{(E_{CNT}/E_{EP}) - (d/4t)}{(E_{CNT}/E_{EP}) - (d/2t)} \right\} \varphi_{CNT} \right] E_{EP} \\
 & + \frac{5}{8} \left[1 + 2 \left\{ \frac{(E_{CNT}/E_{EP}) - (d/4t)}{(E_{CNT}/E_{EP}) + (l/2t)} \right\} \varphi_{CNT} \right] \\
 & \times \left[1 - \left\{ \frac{(E_{CNT}/E_{EP}) - (d/4t)}{(E_{CNT}/E_{EP}) + (d/2t)} \right\} \varphi_{CNT} \right]^{-1} E_{EP}, \quad (1)
 \end{aligned}$$

where E_c = Young's modulus of nanocomposite, E_{EP} = Young's modulus of neat epoxy, E_{CNT} = Young's modulus of AFMWCNTs, l/d = aspect ratio of dispersed AFMWCNTs, d = diameter of AFMWCNTs, l = length of AFMWCNTs, t = thickness of graphite layer (3.4 Å), and φ_{CNT} = volume fraction of AFMWCNTs given by the following equation:

$$\varphi_{CNT} = \frac{1}{[(\rho_{CNT}/\rho_{EP}) \times (M_{EP}/M_{CNT})] + 1}, \quad (2)$$

where ρ_{CNT} is density of CNT, ρ_{EP} is density of epoxy, M_{EP} is mass volume fraction of epoxy, and M_{CNT} is mass fraction of CNTs, calculated to be 0.143% based on the CNT and epoxy densities of 2.1 and 1.2 g/cc, respectively [25, 26]. The estimated diameter, length and modulus of AFMWCNTs are 20 nm, 30 μm and 400 GPa, respectively. Calculated tensile modulus equal to 3.10 GPa of neat epoxy and (1) yields the CNT/epoxy composite tensile modulus of 3.46 GPa at 0.25 wt% CNT loading, which translates to a 11.61% increase over the neat epoxy modulus. In the calculations, the CNT composites were regarded as isotropic as the AFMWCNTs which were assumed to be uniformly distributed and randomly oriented throughout the matrix. As the amount of CNTs was small, the Poisson's ratio of the CNT

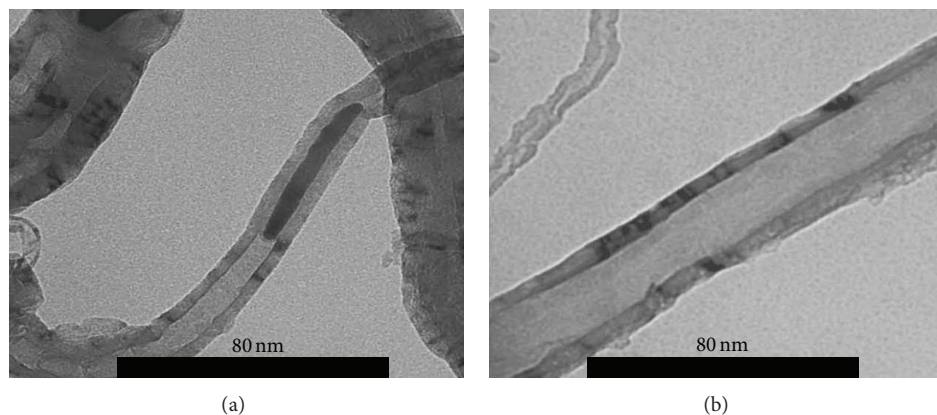


FIGURE 4: TEM image of AFMWCNTs showing (a) aligned bundles and (b) isolated MWCNT.

composite was assumed to be the same as that of epoxy, that is, 0.35 [27]. Considering isotropy, the shear modulus can be calculated using the following equation:

$$G_C = \frac{E_C}{2(1 + \nu)}, \quad (3)$$

where G_C is shear modulus and ν is Poisson's ratio of CNT/epoxy composites. Table 2 shows the results of elastic properties of CNT/epoxy composites for varying percentage of CNTs. At 0.25 wt% CNT loading the shear modulus increased by 11.30%. Table 3 shows the elastic properties of ICFCFEC and CNTCFEC multiscale three-phase composites. For multiscale composites, the mechanical properties of CNT composites were used as matrix properties. The composite was considered to be unidirectional fibre reinforced and the mechanical properties were calculated by CADEC, a micromechanics software by Barbero [27]. The composites have been theoretically tested for longitudinal Young's modulus up to 5 wt% of CNT reinforcement; this is because of the continuously increasing trend of modulus. The mechanical reinforcement of different wt% CNTs in epoxy matrix shows an improvement of 25.83% in longitudinal tensile modulus, while moderate improvement has been observed in transverse tensile modulus and in-plane shear modulus. This can be attributed to CNT reinforcement in the longitudinal direction that is fiber dominated.

3. Experimental Results and Discussion

First, the functionalisation of AFMWCNTs was verified using FTIR spectroscopy, and in the second phase, five specimens of each type of composites have been tested and analyzed. For multiscale composites tensile, flexural and shear tests were performed and the results are discussed in this section.

3.1. Effect of Functionalisation. FTIR spectroscopy has shown limited ability to probe the structure of AFMWCNTs owing to their poor infrared transmittance. Because of their black character, the AFMWCNTs exhibit a strong absorbance and often are unable to be distinguished from the background noise, making it necessary to use a very weak concentration

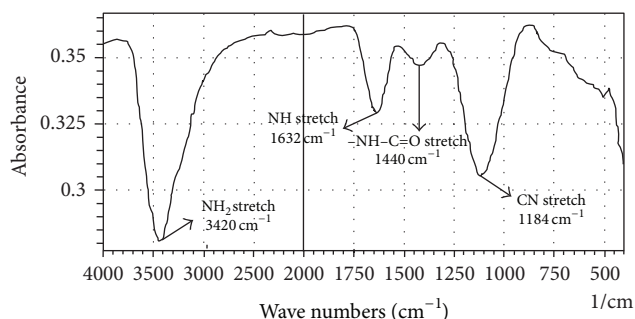


FIGURE 5: FTIR spectrum of AFMWCNTs.

of the nanotubes in potassium bromide (KBr) powder. As shown in Figure 5, the peak at 3420 cm^{-1} corresponds to the NH_2 stretch and peaks at 1632 and 1184 cm^{-1} correspond to the NH in-plane and C-N bond stretching, respectively, in AFMWCNTs. The 3420 cm^{-1} peak produced by the flexible fluctuation of primary amine ensures the presence of amine group in MWCNTs.

3.2. Tensile Test. Figure 6 shows the fractured specimen after tensile testing. Five test specimens were tested for each composite type as listed in Table 1. Figure 7(a) shows the typical stress-strain plots for different compositions while Figures 7(b) and 7(c) show the mean values (along with standard deviation error bars) of tensile modulus and tensile strength, respectively, of different multiphase composites. In general, the longitudinal tensile modulus and tensile strength of unidirectional multiphase composites exhibit a fibre dominated behaviour. This is clearly observed for longitudinal tensile modulus plotted in Figure 7(b). Figure 7(c) demonstrates that the tensile strength of the three-phase composite increases from 1.25 GPa (CFEC) to 1.90 GPa (3CNTCFEC), that is, 51.46%, but for 4CNTCFEC it decreases. This may be attributed to the formation of the covalent bond between AFMWCNTs and epoxy matrix, leading to more effective stress transfer.

TABLE 2: Tensile properties of neat epoxy and CNT/epoxy composites.

% CNT in CNT/epoxy composite	Tensile modulus E (GPa)	Poisson's ratio ν	Shear modulus G (GPa)
0.0% CNT (neat epoxy)	3.10	0.35	1.15
0.25%	3.46	0.35	1.28
0.50%	3.83	0.35	1.42
1.00%	4.26	0.35	1.58
1.50%	4.41	0.35	1.63

TABLE 3: Elastic properties of carbon fibre/epoxy and carbon fibre/CNT/epoxy multiscale composites.

Composite description	Longitudinal tensile modulus E_{11} (GPa)	Transverse tensile modulus E_{22} (GPa)	In-plane Poisson's ratio ν_{12}	In-plane shear modulus G_{12} (GPa)
CFEC	98.92	7.59	0.284	2.75
1CNTCFEC	124.48	8.46	0.284	3.07
2CNTCFEC	128.94	9.34	0.284	3.39
3CNTCFEC	138.35	10.36	0.284	3.77
4CNTCFEC	142.58	10.72	0.284	3.89

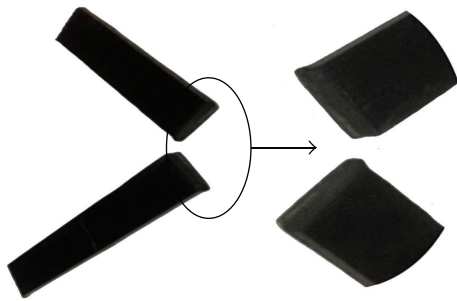


FIGURE 6: Fractured specimen of multiscale composites.

Young's modulus has been increased by 40.4% for 1CNTCFEC when compared with CFEC, as shown in Figure 7(c). This is because of the fact that the longitudinal tensile modulus and tensile strength for unidirectional composite laminates in general show fibre dominated behaviour. The AFMWCNTs prove to be even more effective due to the alignment of the polymer chains along the CNTs in the axial direction. This may be due to the presence of $-\text{NH}_2$ functional groups at the surface of CNTs. This results in reduction in the average free polymer chain length and improvement cross-linking of the polymer chains with CNTs, leading to an obvious increase in the tensile strength and longitudinal tensile modulus. However, a decrease was observed for the 4CNTCFEC (reinforcement above 1.0 wt%); this may be due to the enhancement in stress which has been built up around the fibres.

In case of CFEC, the theoretical tensile modulus was found to be larger than the experimental value by approximately 16%, as shown in Figure 8. This may be attributed to the assumptions implicated in the Halpin-Tsai equations, namely, perfect fibre-matrix bonding, good dispersion, and high l/d ratio. The carbon fibre/CNT/epoxy interface was investigated by observing the morphology of the fractured

surface using SEM. The specimen investigated by SEM was initially coated with gold before examination under the microscope. The SEM images shown in Figures 9(a) and 9(b) illustrate weak bonding at the fibre-matrix interface.

3.3. Shear Test. Figure 10 shows the specimen after testing in shear. For the shear test, five test specimens were tested for each composite type. The experimental results in Figure 11 are the mean values of the five test specimens with standard deviation bars. The test results show a systematic increase in ILSS up to 3CNTCFEC and further decrease of 38.76% on addition of more CNTs. This was increased by 27% for 3CNTCFEC as compared to CFEC. The increase in ILSS by addition of AFMWCNTs is due to surface modification, which results in a strong interfacial interaction. Similar results were also reported by Gojny et al. [9] and Zhihang et al. [10]; however, they used a different matrix (name it here). Godara et al. [14] reported an ILSS value of 68 MPa for modified MWCNTs which was 13.33% higher than the unmodified MWCNTs.

The other possible reasons are less damaged CNT surface, maintained aspect ratio, and the optimized level (up to 10%) of $-\text{NH}_2$ functional groups added during the CNT functionalisation process. Additional factors like step time and temperature can also influence the grafting of a number of functionalised groups at the CNT surface. Park et al. [25] reported such an influence on the CNT/epoxy composite in terms of decreased matrix toughness, with an increase in temperature. They also elaborated the importance of the optimisation of CNT surface functionalisation, as it strongly influences the polarity and level of interaction of CNT surface with the matrix. In addition, Ci and Bai [26] explained the minimum influence of CNT reinforcement on the properties of composite if the matrix is extremely tough. Therefore, it is difficult to observe any effect on the strength of the epoxy matrix for any CNT type. They also revealed that soft and

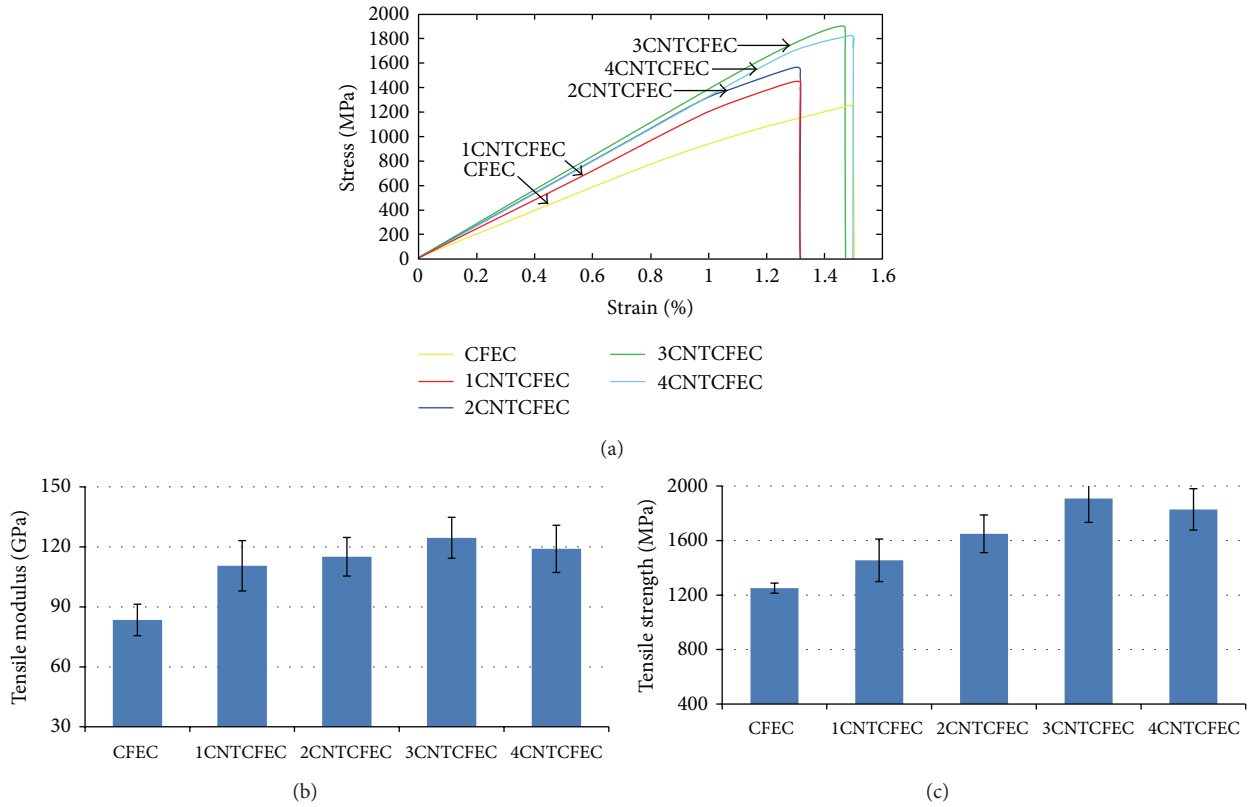


FIGURE 7: (a) Stress-strain plots, (b) tensile modulus, and (c) tensile strength of different multiphase composites.

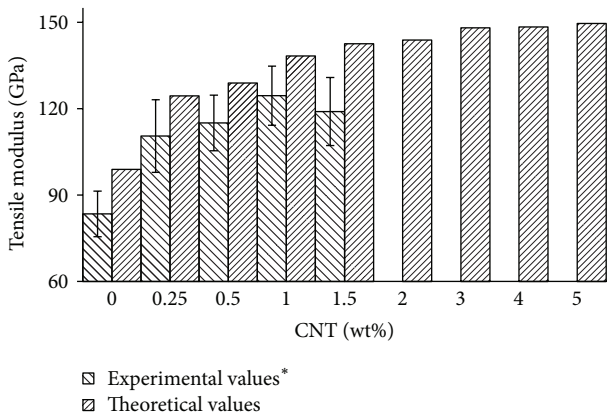


FIGURE 8: Comparison of theoretical and experimental longitudinal tensile modulus. *Experimental values were determined only up to 1.5 wt% of CNT reinforcement.

ductile matrices allow better interface adjoining, whereas the interfacial interaction is poor due to complete cross-linking of polymer molecules surrounding the CNTs in the stiff matrix. The matrix used to fabricate laminates in the present study has a modulus of about 3.10 GPa, which is well above the limit mentioned by Ci and Bai [26].

The significant decrease of ILSS for 4CNTCFEC is attributed to a combination of higher matrix rigidity and higher interfacial interaction. Such a behaviour suggests

an optimisation of the inert sites of the CNT surface for the optimal level of interaction with matrix. The surface modification using amine functionalisation shows positive effects in comparison with the CFEC composite system. As expected, the increased physical affinity between the AFMWCNTs and epoxy resin system worked positively in this case.

3.4. Flexural Test. Figure 12 shows the improvement in flexural strength of multiscale composite with increased content of CNTs. When compared with CFEC, the 2CNTCFEC and 3CNTCFEC composites showed a 24.69% and 38.04% increase in flexural strength, respectively. This enhancement was due to the reinforcing effect of the CNTs, as flexural properties are matrix dominated rather than being fibre dominated. The reduced flexural strength of 4CNTCFEC, when compared to 3CNTCFEC, can be inferred from the fact that there exists a more dominant factor than the degree of CNT dispersion that governs the matrix dominated mechanical properties. Another comparing factor may be the degree of cure of the epoxy resin at the time of infusion. Incomplete fibre wetting due to high viscosity of the mixture tends to weaken the crosslinking between polymer molecules to conform to the fibre preform and infiltrate the interfilament spaces. In addition to this, heat buildup during prolonged sonication and ball milling may contribute to premature curing, and this possibility warrants further investigation [23]. However, a maximum enhancement in flexural modulus

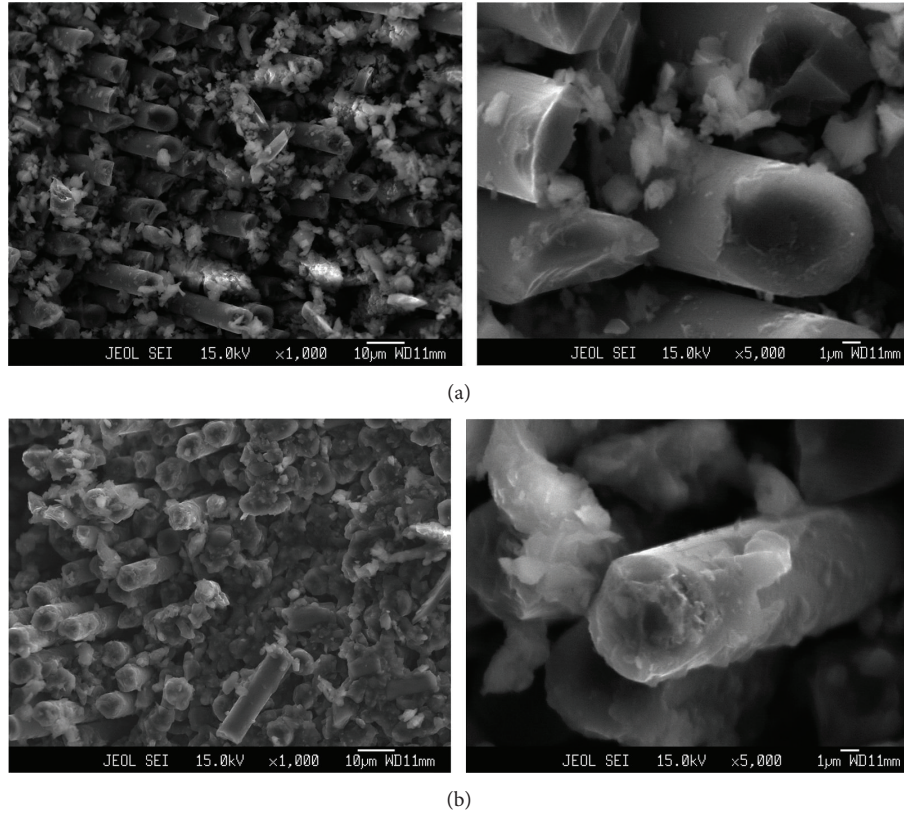


FIGURE 9: SEM images of carbon fibre epoxy interface showing debonding and void in (a) 2CNTCFEC and (b) 3CNTCFEC sample.



FIGURE 10: Shear tested specimen of multiscale composite.

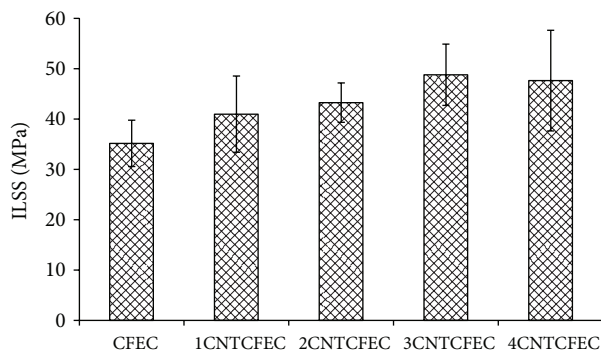


FIGURE 11: ILSS variation with CNT concentration (wt%).

by 35% and a 5% improvement in flexural strength have been shown by [28] for small addition of CNTs (0.025, 0.05, and 0.1 wt%) in epoxy resin.

For optimising the advantage of reinforcing effect of CNTs, it is crucial to achieve a strong interface between the CNTs and the matrix. In particular, it is important to reinforce the interface between the carbon fibre and the matrix using CNTs so that the load can be transferred from the fibre to the matrix, and at the same time, the gap between the highly mismatched properties of the matrix and the fibre can be bridged [9]. Optimized functionalisation of the CNT surfaces may be the most effective solution for successful load transfer between the CNTs and matrix, results of which increase the mechanical properties of multiscale composites considerably.

4. Conclusion

Carbon fibre/CNT/epoxy multiscale composites were fabricated and characterised in this research. A detailed analysis of the experimental results obtained has been presented in this paper. Good dispersion and perfect bonding were the two major issues for significant improvement of the mechanical properties of carbon fibre/CNT/epoxy three-phase composites. AFMWCNTs were uniformly distributed in the carbon fibre-epoxy matrix using ultrasonic treatment assisted or combined with high speed mechanical steering or stirring. The dispersion technique used for AFMWCNTs led to a significant improvement in the mechanical properties of the three-phase multiscale composites. Dispersion of only 1.0% AFMWCNTs in the matrix improved the Young's modulus and tensile strength of carbon fiber/epoxy composites by

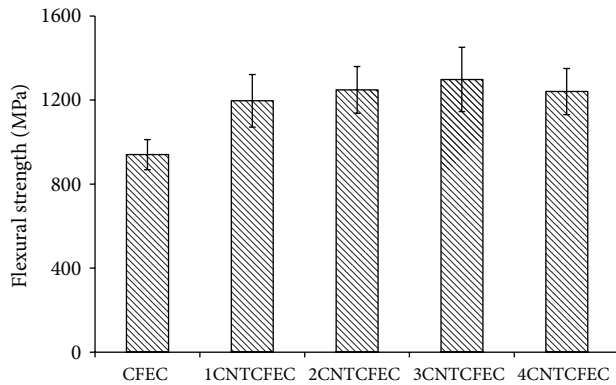


FIGURE 12: Flexural strength variation with CNT concentration (wt%).

49% and 52%, respectively. Similarly, the ILSS and flexural strength improved by 37% and 38%, respectively. Improved mechanical properties of multiscale composites are attributed to the formation of strong interface between the carbon fibres and the epoxy matrix in the presence of AFMWCNTs.

Three-phase composite modeling was performed in parallel to predict the tensile properties. The Halpin-Tsai equations and conventional micromechanics rule of mixtures were combined to calculate Young's modulus of three-phase composites. Theoretical Young's modulus of carbon fiber/epoxy composites was higher by 16% than the experimental Young's modulus. This may be attributed to the assumptions implicated in the Halpin-Tsai equations, namely, perfect fibre-matrix bonding, good dispersion, and high l/d ratio.

Conflict of Interests

The authors declare that there is no conflict of interests regarding the publication of this paper.

Acknowledgments

The authors are grateful to the Advanced System Laboratory (ASL) DRDO, Hyderabad, India, for their technical and financial support. The authors are also grateful to Mr. Alex Daniel and Mr. I. Srikanth of ASL who assisted in with the laminate fabrication and mechanical testing, respectively. Thanks are also due to Mrs. Rohini Devi and Mr. Anil Kumar of ASL for their overall support.

References

- [1] J. Njuguna, K. Pielichowski, and J. R. Alcock, "Epoxy-based fibre reinforced nanocomposites," *Advanced Engineering Materials*, vol. 9, no. 10, pp. 835–847, 2007.
- [2] J. Njuguna, K. Pielichowski, and J. R. Alcock, "Polymer nanocomposites for aerospace applications: characterization," *Advanced Engineering Materials*, vol. 6, no. 4, pp. 204–210, 2004.
- [3] F. H. Gojny and K. Schulte, "Functionalisation effect on the thermo-mechanical behaviour of multi-wall carbon nanotube/epoxy-composites," *Composites Science and Technology*, vol. 64, no. 15, pp. 2303–2308, 2004.
- [4] K. Lau and S. Shi, "Failure mechanisms of carbon nanotube/epoxy composites pretreated in different temperature environments," *Carbon*, vol. 40, no. 15, pp. 2965–2973, 2002.
- [5] R. G. de Villoria, A. Miravete, J. Cuartero, A. Chiminelli, and N. Tolosana, "Mechanical properties of SWNT/epoxy composites using two different curing cycles," *Composites B*, vol. 37, no. 4–5, pp. 273–280, 2006.
- [6] M. Abdalla, D. Dean, D. Adibempe, E. Nyairo, P. Robinson, and G. Thompson, "The effect of interfacial chemistry on molecular mobility and morphology of multiwalled carbon nanotubes epoxy nanocomposite," *Polymer*, vol. 48, no. 19, pp. 5662–5670, 2007.
- [7] F. Zhang, R. Wang, X. He, C. Wang, and L. Ren, "Interfacial shearing strength and reinforcing mechanisms of an epoxy composite reinforced using a carbon nanotube/carbon fiber hybrid," *Journal of Materials Science*, vol. 44, no. 13, pp. 3574–3577, 2009.
- [8] A. Eitan, K. Jiang, D. Dukes, R. Andrews, and L. S. Schadler, "Surface modification of multiwalled carbon nanotubes: toward the tailoring of the interface in polymer composites," *Chemistry of Materials*, vol. 15, no. 16, pp. 3198–3201, 2003.
- [9] F. H. Gojny, M. H. G. Wichmann, B. Fiedler, W. Bauhofer, and K. Schulte, "Influence of nano-modification on the mechanical and electrical properties of conventional fibre-reinforced composites," *Composites A*, vol. 36, no. 11, pp. 1525–1535, 2005.
- [10] F. Zhihang, H. S. Michael, and S. Advani, "Interlaminar shear strength of glass fiber reinforced epoxy composites enhanced with multi-walled carbon nanotubes," *Composites A*, vol. 39, no. 3, pp. 540–554, 2008.
- [11] T. Yokozeki, Y. Iwahori, and S. Ishiwata, "Matrix cracking behaviors in carbon fiber/epoxy laminates filled with cup-stacked carbon nanotubes (CSCNTs)," *Composites A*, vol. 38, no. 3, pp. 917–924, 2007.
- [12] E. T. Thostenson, W. Z. Li, D. Z. Wang, Z. F. Ren, and T. W. Chou, "Carbon nanotube/carbon fiber hybrid multiscale composites," *Journal of Applied Physics*, vol. 91, no. 9, pp. 6034–6041, 2002.
- [13] M. F. De Riccardis, D. Carbone, T. D. Makris, R. Giorgi, N. Lisi, and E. Salernitano, "Anchorage of carbon nanotubes grown on carbon fibres," *Carbon*, vol. 44, no. 4, pp. 671–674, 2006.
- [14] A. Godara, L. Mezzo, F. Luizi et al., "Influence of carbon nanotube reinforcement on the processing and the mechanical behaviour of carbon fiber/epoxy composites," *Carbon*, vol. 47, no. 12, pp. 2914–2923, 2009.
- [15] J. C. Halpin and J. L. Kardos, "The Halpin-Tsai equations: a review," *Polymer Engineering and Science*, vol. 16, no. 5, pp. 344–352, 1976.
- [16] S. Peeterbroeck, L. Breugelmans, M. Alexandre et al., "The influence of the matrix polarity on the morphology and properties of ethylene vinyl acetate copolymers-carbon nanotube nanocomposites," *Composites Science and Technology*, vol. 67, no. 7–8, pp. 1659–1665, 2007.
- [17] D. Qian, E. C. Dickey, R. Andrews, and T. Rantell, "Load transfer and deformation mechanisms in carbon nanotube-polystyrene composites," *Applied Physics Letters*, vol. 76, no. 20, pp. 2868–2870, 2000.

- [18] X. Li, H. Gao, W. A. Scrivens et al., "Reinforcing mechanisms of single-walled carbon nanotube-reinforced polymer composites," *Journal of Nanoscience and Nanotechnology*, vol. 7, no. 7, pp. 2309–2317, 2007.
- [19] G. D. Seidel and D. C. Lagoudas, "Micromechanical analysis of the effective elastic properties of carbon nanotube reinforced composites," *Mechanics of Materials*, vol. 38, no. 8–10, pp. 884–907, 2006.
- [20] B. Jiang, C. Liu, C. Zhang, B. Wang, and Z. Wang, "The effect of non-symmetric distribution of fiber orientation and aspect ratio on elastic properties of composites," *Composites B*, vol. 38, no. 1, pp. 24–34, 2007.
- [21] T. Mori and K. Tanaka, "Average stress in matrix and average elastic energy of materials with misfitting inclusions," *Acta Metallurgica*, vol. 21, no. 5, pp. 571–574, 1973.
- [22] M. Yeh, N. Tai, and J. Liu, "Mechanical behavior of phenolic-based composites reinforced with multi-walled carbon nanotubes," *Carbon*, vol. 44, no. 1, pp. 1–9, 2006.
- [23] M. Kim, Y. Park, O. I. Okoli, and C. Zhang, "Processing, characterization, and modeling of carbon nanotube-reinforced multiscale composites," *Composites Science and Technology*, vol. 69, no. 3–4, pp. 335–342, 2009.
- [24] J. Shen, W. Huang, L. Wu, Y. Hu, and M. Ye, "Study on amino-functionalized multiwalled carbon nanotubes," *Materials Science and Engineering A*, vol. 464, no. 1–2, pp. 151–156, 2007.
- [25] S. Park, H. Jeong, and C. Nah, "A study of oxyfluorination of multi-walled carbon nanotubes on mechanical interfacial properties of epoxy matrix nanocomposites," *Materials Science and Engineering A*, vol. 385, no. 1–2, pp. 13–19, 2004.
- [26] L. Ci and J. Bai, "The reinforcement role of carbon nanotubes in epoxy composites with different matrix stiffness," *Composites Science and Technology*, vol. 66, no. 3–4, pp. 599–603, 2006.
- [27] E. Barbero, *Introduction to Composite Materials Design*, vol. 17, pp. 29–35, Taylor & Francis, 1999.
- [28] T. Peijs, F. Inam, D. W. Y. Wong, and M. Kuwata, "Multiscale hybrid micro-nanocomposites based on carbon nanotubes and carbon fibers," *Journal of Nanomaterials*, vol. 2010, Article ID 453420, 12 pages, 2010.

Research Article

Triple-Component Drug-Loaded Nanocomposites Prepared Using a Modified Coaxial Electrospinning

Wei Qian,¹ Deng-Guang Yu,¹ Ying Li,¹ Xiao-Yan Li,¹ Yao-Zu Liao,² and Xia Wang¹

¹ School of Materials Science & Engineering, University of Shanghai for Science and Technology,
516 Jungong Road, Yangpu District, Shanghai 200093, China

² School of Chemistry, University of Bristol, Bristol BS8 1TS, UK

Correspondence should be addressed to Deng-Guang Yu; ydg017@usst.edu.cn and Xia Wang; wangxia@163.com

Received 17 June 2013; Accepted 27 November 2013

Academic Editor: Gaurav Mago

Copyright © 2013 Wei Qian et al. This is an open access article distributed under the Creative Commons Attribution License, which permits unrestricted use, distribution, and reproduction in any medium, provided the original work is properly cited.

Triple-component nanocomposites for improved sustained drug release profiles are successfully fabricated through a modified coaxial electrospinning process, in which only organic solvent N,N-dimethylacetamide was used as sheath fluid. Using polyacrylonitrile (PAN) as filament-forming matrix, ibuprofen (IBU) as functional ingredient, and polyvinylpyrrolidone (PVP) as the additional component, the IBU/PVP/PAN triple-component nanocomposites had uniform structure and an average diameter of 620 ± 120 nm and 650 ± 120 nm when the contents of PVP in the nanofibers were 10.5% and 22.7%, respectively. The optimal sheath-to-core flow rate ratio was 0.11 under a total sheath and core fluid flow rate of 1.0 mL/h. Compared with the IBU/PAN composite nanofibers, the triple-component composites could release 92.1% and 97.8% of the contained IBU, significantly larger than a value of 73.4% from the former. The inclusion of PVP in the IBU/PAN could effectively avoid the entrapment of IBU in the insoluble PAN molecules, facilitating the *in vitro* release of IBU. The modified coaxial process and the resulted multiple component nanocomposites would provide new way for developing novel drug sustained materials and transdermal drug delivery systems.

1. Introduction

Electrospinning is a one-step straightforward nanofiber fabrication process, in which electrical energy is exploited to dry and solidify microfluid jets directly [1–4]. The processes produce nanosized fibers very rapidly, often at approximately 10^{-2} s. As a result, the physical state of the components in the liquid solutions is often propagated into the solid nanofibers to generate solid dispersions at a molecular scale or polymer-based composites, with few discerned nanoparticles resulted from phase separation [5, 6]. There exist numerous reports of electrospinning being used to produce polymer-based nanocomposite in the form of nanofibers. By virtue of the advantageous properties of nanofibers (e.g., high surface area, high porosity, and continuous web structure), these composites usually display improved functional performance [7–11].

Significant progress has been made in this process throughout the past few years and electrospinning has advanced its applications in many fields, including pharmaceuticals. Electrospun nanofibers show great promise for developing many types of novel drug delivery systems (DDS) due to their special characteristics and the simple but useful and effective top-down fabricating process. For controlled release of active pharmaceutical ingredients, electrospun nanofibers are reported to provide a series of controlled drug release profiles, such as immediate, pulsatile, delayed, sustained, and biphasic releases [12, 13]. Among them, sustained drug release is gaining considerable attention as a method of administering and maintaining desired drug concentrations in the blood within a specified therapeutic window, or in target tissues within a desired duration of drug delivery [14, 15]. The first study on the application of electrospun nanofibers in pharmaceuticals focused on the sustained release of tetracycline hydrochloride

using poly(lactic acid) and poly(ethylene-co-vinyl acetate), as well as their blend as filament-forming polymeric matrices [16].

It has been broadly reported that drug-loaded nanofibers are fabricated through electrospinning of a codissolving solution of a guest pharmaceutical active ingredient and a host polymer. For these nanofibers, the initial burst effect is inevitable because of the large nanofiber surfaces, drug distribution on the nanofiber surfaces, and also the amorphous status of the drug. Yu et al. has reported a modified coaxial electrospinning process, by which a blank polymer layer was coated on the nanofibers to offer a zero-order drug release profile [14, 15]. However, there is still another problem waiting to be solved for electrospun two-component composites for providing fine sustained drug release profiles. The problem is that the encapsulated drug in the nanofibers was often not completely released into the dissolution medium owing to the entrapment of drug molecules by the filament-forming polymer molecules or gave an undesirable long time period of “leveling-off” release processes [17]. This phenomenon is even severe when the polymer matrix is insoluble and nondegradable, in which only about 70% of the contained drug could be effectively released out *in vitro* dissolution [17, 18].

Building on the previous discussion, this study investigates the addition of a third auxiliary component in the electrospun drug-loaded nanofibers, by which the drug release profiles can be efficaciously improved. Polyacrylonitrile (PAN) and ibuprofen (IBU) were selected as the model filament-forming matrix and drug, respectively. Polyvinylpyrrolidone (PVP), a hydrophilic polymer, was selected as the additional third component. Polyacrylonitrile (PAN) is a synthetic, semicrystalline organic polymer resin, with the linear formula $(C_3H_3N)_n$. It is a versatile polymer used to produce large variety of products including ultrafiltration membranes, hollow fibers for reverse osmosis, fibers for textiles, oxidized flame retardant fibers, carbon fiber, and medicated nanofibers [19]. For biomedical applications, PAN has been exploited as filament-forming matrix to generate medicated fibers through traditional wet-spinning, dry-spinning [20, 21], and also electrospinning [22]. However, the drug release profiles of drug-loaded PAN fibers are unsatisfied due to poor drug controlled release property [20–22]. A modified coaxial electrospinning process, characterized by an unspinnable solvent as sheath fluid, was exploited to generate the triple-component nanocomposites. This process has been used to realize several new possibilities, such as controlling the size of nanoparticles self-assembled from electrospun nanofibers, preparing ultrafine structures from concentrated polymer solutions previously thought unspinnable, improving systematically polymer nanofiber quality, and generating high quality carbon nanofiber precursors [12–15].

2. Experimental

2.1. Materials. PAN powders ($\overline{M}_w = 80,000$) were provided by Jinshan Petrochemistry Co., Ltd. (Shanghai, China). PVP K30 ($\overline{M}_w = 58,000$) was obtained from Shanghai Yunhong

Pharmaceutical Aids and Technology Co., Ltd. (Shanghai, China). IBU was purchased from Wuhan Fortuna Chemical Co., Ltd. (Hubei, China). Methylene blue, N, N-dimethylacetamide (DMAc) were obtained from the Sinopharm Chemical Reagent Co., Ltd. (Shanghai, China). All reagents were analytical grade and were used without further purification. Water was double distilled just before use.

2.2. Modified Coaxial Electrospinning. The three types of core electrospinnable PAN solutions were prepared by first dissolving 15.0 g of PAN and 2 g of IBU in 100 mL DMAc, and then 0, 2, and 5 g PVP K30 were codissolved in them. For digital observation and optimization of sheath-to-core flow rate ratio, 5 ppm of methylene blue was added to the second solutions with a PVP content of 10.5% $[2/(15+2+2) \times 100\%]$. The sheath fluid was pure DMAc.

Two syringe pumps (KDS100 and KDS200, Cole-Parmer, IL, USA), a high-voltage power supply (ZGF 60 kV/2 mA, Shanghai Sute Corp., Shanghai, China), and a homemade concentric spinneret were used to conduct the electrospinning process. Following some optimizations, the applied voltage was fixed at 18 kV and the fibers were collected on an aluminum foil at a distance of 20 cm. All electrospinning processes were carried out under ambient conditions ($24 \pm 2^\circ\text{C}$; relative humidity, $57\% \pm 5\%$). The electrospinning process was recorded using a digital video recorder (PowerShot A490, Canon, Tokyo, Japan). The other parameters are listed in Table 1.

2.3. Characterization. The morphology of the nanofiber mats was assessed using a Quanta FEG450 scanning electron microscope (SEM) (FEI Corporation, The Netherlands). Prior to the examination, the samples were rendered electrically conductive by gold sputter coating under a nitrogen atmosphere. The average fiber diameter was determined by measuring their diameters in the FESEM images at more than 100 different locations using the Image J software (National Institutes of Health, MD, USA).

X-ray diffraction (XRD) patterns were obtained on a D/Max-BR diffractometer (RigaKu, Tokyo, Japan) with $\text{CuK}\alpha$ radiation within the 2θ range of 5° – 60° at 40 mV and 30 mA. Differential scanning calorimetry (DSC) analyses were carried out using an MDSC 2910 differential scanning calorimeter (TA Instruments Co., New Castle, DE, USA). Sealed samples were heated at $10^\circ\text{C min}^{-1}$ from 50 to 300°C under a nitrogen gas flow of 40 mL/min. Fourier transform infrared (FTIR) analyses were performed on a Nicolet-Nexus 670 FTIR spectrometer (Nicolet Instrument Corporation, WI, USA) from 500 cm^{-1} to 4000 cm^{-1} at a resolution of 2 cm^{-1} .

In vitro dissolution tests were carried out according to the Chinese Pharmacopoeia (2005 ed.) Method II, a paddle method in which an RCZ-8A dissolution apparatus (Tianjin University Radio Factory, Tianjin, China) was used. About 200 mg of drug-loaded nanofibers were placed in 900 mL of physiological saline (PS; 0.9 wt%) at $37 \pm 1^\circ\text{C}$. The instrument was then set to 50 rpm, providing sink conditions in which $C < 0.2C_s$. At predetermined time points, 5.0 mL samples

TABLE 1: Parameters of the electrospinning processes and their products.

No.	Electrospinning	PVP content (%)	Flow rate (mL/h)			Morphology ^b	Diameter (nm)
			Sheath fluid ^a	Core fluid	Ratio		
F1	Single	10.5	0.0	1.0	0	Linear/thick fibers	780 ± 210
F2	Coaxial	10.5	0.1	0.9	0.11	Linear	620 ± 120
F3	Coaxial	10.5	0.2	0.8	0.25	Beads-on-a-string	440 ± 140
F4	Coaxial	0	0.1	0.9	0.11	Linear	610 ± 110
F5	Coaxial	22.7	0.1	0.9	0.11	Linear	650 ± 120

^aSheath fluid was DMAc.

^bIn this column, "linear" morphology refers to nanofibers with few beads or spindles on them.

were withdrawn from the dissolution medium and replaced with fresh medium to maintain a constant volume. After filtration through a 0.22 μm membrane (Millipore, MA, USA) and appropriate dilution with PS, the samples were analyzed at $\lambda_{\text{max}} = 264 \text{ nm}$ using a UV-vis spectrophotometer (UV-2102PC, Unico Instrument Co. Ltd., Shanghai, China). The cumulative amount of IBU released at each time point was reverse calculated from the data obtained against a predetermined calibration curve. Experiments were carried out six times and the results are presented as mean values.

3. Results and Discussion

3.1. The Modified Coaxial Electrospinning. A schematic diagram of the modified coaxial electrospinning process with solvent as sheath fluid is shown in Figure 1(a). A homemade concentric spinneret was used to carry out the modified process (Figure 1(b)). The critical voltage applied to a fluid to initiate Taylor cone formation and the straight thinning jet (V_c) have a close relationship with the diameter of sheath part of the concentric spinneret [12], as indicated by

$$V_c \sim \sqrt{\frac{\gamma d^2}{\epsilon R}}, \quad (1)$$

where V_c is the critical voltage for a jet emanating from the meniscus tip, d is the electrode separation, ϵ is the permittivity, γ is the surface tension, and R is the principal curvature of the liquid meniscus. A small diameter of the spinneret's orifice means a big value of R , and thus a small V_c to imitate the coaxial electrospinning process. The homemade spinneret used in the study has an outer and inner diameter of 1.2 and 0.3 mm, respectively (Figure 1(b)), facilitating the coaxial electrospinning process. In addition, the inner capillary projects a little from the surface of the outer capillary, which is expected to make the sheath DMAc well encompass the core codissolving spinnable solutions.

When the modified coaxial electrospinning was carried out to prepare the composite nanofibers, two syringe pumps were used to drive the sheath and core fluids independently (Figure 2(a)). An alligator clip was used to connect the inner stainless steel capillary with the high voltage supply (Figure 2(b)). With DMAc as sheath fluid and under a sheath-to-core flow rate ratio of 0.11, the arrangement produced a typical fluid jet trajectory, in which a Taylor cone is followed by a straight fluid jet and a bending and whipping instability

region (Figure 2(c)). As the applied voltage was boosted from 0 kV to 18 kV, the core-shell droplet was quickly transformed from a round shape (Figure 2(d)) to a cone shape, that is, the well-known Taylor cone (Figure 2(e)). The compound Taylor cone is clearly composed of two parts with the sheath solvent well surrounding the core polymer solutions, as indicated by the methylene blue in Figure 2(e). Although the modified coaxial process could not create core-sheath nanostructure, the surrounding solvent did facilitate a stable, continuous, and smooth electrospinning process, and it was expected to produce monolithic nanofibers with higher quality in terms of smaller diameters and smoother surfaces and with more uniform structures [23].

3.2. Morphology of the Nanofibers. In the modified coaxial electrospinning process, one of the most important parameters is the sheath-to-core flow rate ratio. To select a suitable value of the sheath flow rate, three different types of sheath-to-core flow rate ratios with a fixed total flow rate through the spinneret (1.0 mL/h, Table 1), that is, 0, 0.11, and 0.25, were taken to fabricate different triple-component nanofibers. Their FESEM images are shown in Figure 3. All the three kinds of nanofiber take linear structure. But when the electrospinning was carried out with a sheath flow rate of 0 (i.e., a single fluid electrospinning), very thick fibers (about several microns and a result of clogging of spinneret from time to time) exist in the nanofibers F1 (Figure 3(a)) although they have an average diameter of $780 \pm 210 \text{ nm}$. When the sheath flow rate was increased to 0.25, there are many beads/spindles in the nanofibers (Figure 3(c)) although a thinner nanofiber with an average diameter of $440 \pm 140 \text{ nm}$ was achieved. In contrast, a suitable sheath-to-core flow rate ratio of 0.11 resulted in nanofibers with higher quality. The nanofibers F2 have smaller diameters and a narrower distribution of $620 \pm 120 \text{ nm}$ than F1 and a better linear structure than F3 (without any beads/spindles or very thick fibers within them). Based on these results, a sheath-to-core flow rate ratio of 0.11 was taken in the present study to generate nanofibers with different content of PVP in the IBU-loaded PAN nanofibers.

Shown in Figure 4 are FESEM images of nanofibers with different contents of PVP in them. All the three types of nanofibers have fine linear structure with few spindles or beads in them. With the increase of PVP in the nanofibers F4 (Figure 4(a)), F2 (Figure 4(b)), and F5 (Figure 4(c)), their

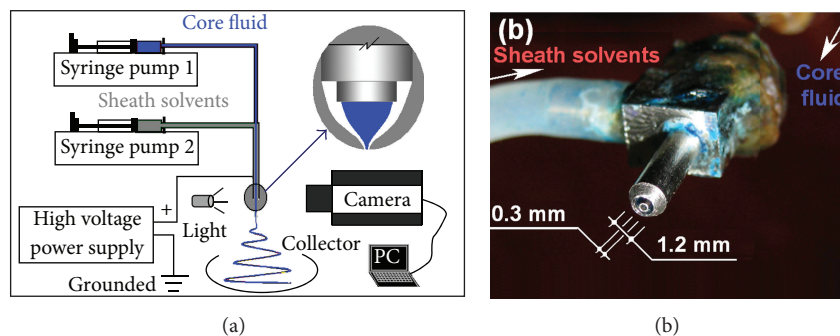


FIGURE 1: A diagram of the modified coaxial electrospinning (a) and the concentric spinneret (b).

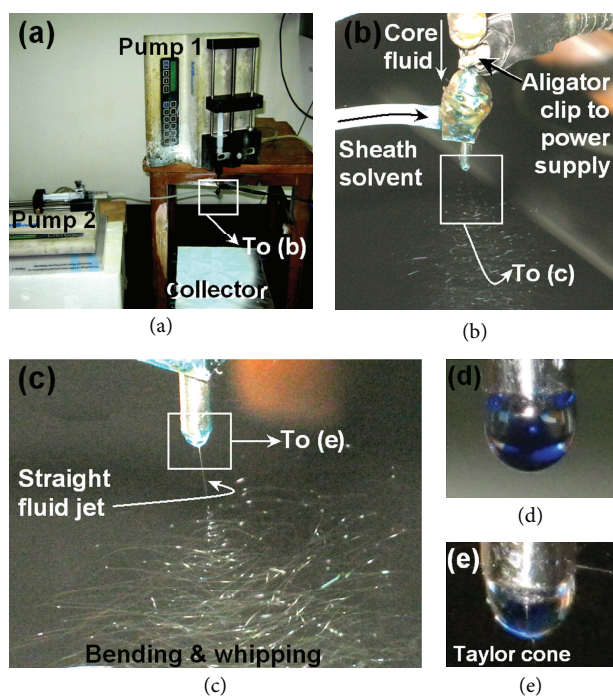


FIGURE 2: Observations of the modified coaxial electrospinning processes: (a) the arrangement of apparatus, (b) the connection of the concentric spinneret with the syringe pumps and the power supply, (c) a typical coaxial electrospinning process with DMAC as sheath fluid and under a sheath-to-core flow rate ratio of 0.11, (d) the core-shell droplet, and (e) the compound Taylor cone under an applied voltage of 18 kV.

average diameters were slightly increased from 610 ± 110 to 620 ± 120 and 650 ± 120 nm, respectively.

3.3. The Physical Status of the Components in the Nanofibers.

The presence of numerous distinct peaks (Figure 5) in the X-ray diffraction patterns indicates that IBU was present as a crystalline material. The spectrum of amorphous PVP K30 was characterized by the complete absence of any diffraction peak. The PAN existed in a half-crystalline status, as demonstrated by the diffraction angle of 2θ at 16.71° . From Figure 5, it is clear that the characteristic diffraction peaks of IBU are completely absent for the three types of composite

nanofibers. This result suggests that all the IBU in the double-component nanofibers F4 and triple-component composite nanofibers F2 and F5 was amorphous.

All DSC thermograms are shown in Figure 6. The DSC curve of pure IBU exhibited a single endothermic response corresponding to the melting point of IBU at 76°C ($\Delta H_f = -125\text{J/g}$). The profile for PAN did not demonstrate any fusion peak or phase transition before it decomposed at peak temperature around 300°C . As an amorphous polymer, PVP K30 did not show any fusion peaks but had a broad endotherm due to dehydration, which lies between 80°C and 120°C and with a peak at 86°C . PVP is a polymer and can be present in a glassy or rubber state. The change from one state to the other can be detected as a small glass transition around $160\text{--}180^\circ\text{C}$, as indicated by "A" in Figure 6 and also verified in the literature [24]. DSC thermograms of all the nanofibers (F2, F4, and F5) similarly did not give a melting peak of IBU and thus indicating that all incorporated drug was no longer present as a crystalline material. The results of DSC concurred with those of XRD that the original structure of IBU was lost and it was completely converted into an amorphous state in all the nanofibers regardless of one or two polymer matrices.

The FTIR spectra of PAN, PVP, IBU, and their composite nanofibers were shown in Figure 7. The existence of PAN in the composite nanofibers was confirmed by the typical absorption at 2243 cm^{-1} ($-\text{C}\equiv\text{N}$). By comparing the spectrum of IBU-loaded PAN nanofibers F4 and IBU-loaded PAN/PVP nanofibers F2 and F5, it is obvious that the IBU spectra has three typical peaks at 1570 , 1610 , and 1725 cm^{-1} , whereas all the nanofibers had only one peak at 1720 cm^{-1} . And all the peaks in the figure region of IBU spectra disappeared in the nanofibers' spectra. These results suggest that there are favorite secondary interactions among the components in the composite nanofibers. From the previously mentioned results and the molecular structure of IBU, PAN, and PVP, it can be speculated that in the double-component composite nanofibers of IBU/PAN, hydrogen bonding interactions may occur between IBU ($-\text{OH}$) and PAN ($-\text{C}\equiv\text{N}$), where IBU acted as H donor, and that in the triple-component composite nanofibers of F2 and F5, hydrogen bonding interactions could occur between IBU ($-\text{OH}$) and PAN ($-\text{C}\equiv\text{N}$) and also between IBU ($-\text{OH}$) and PVP ($>\text{C}=\text{O}$). These hydrogen bondings would take their role in keeping the IBU molecules evenly and stably distributed

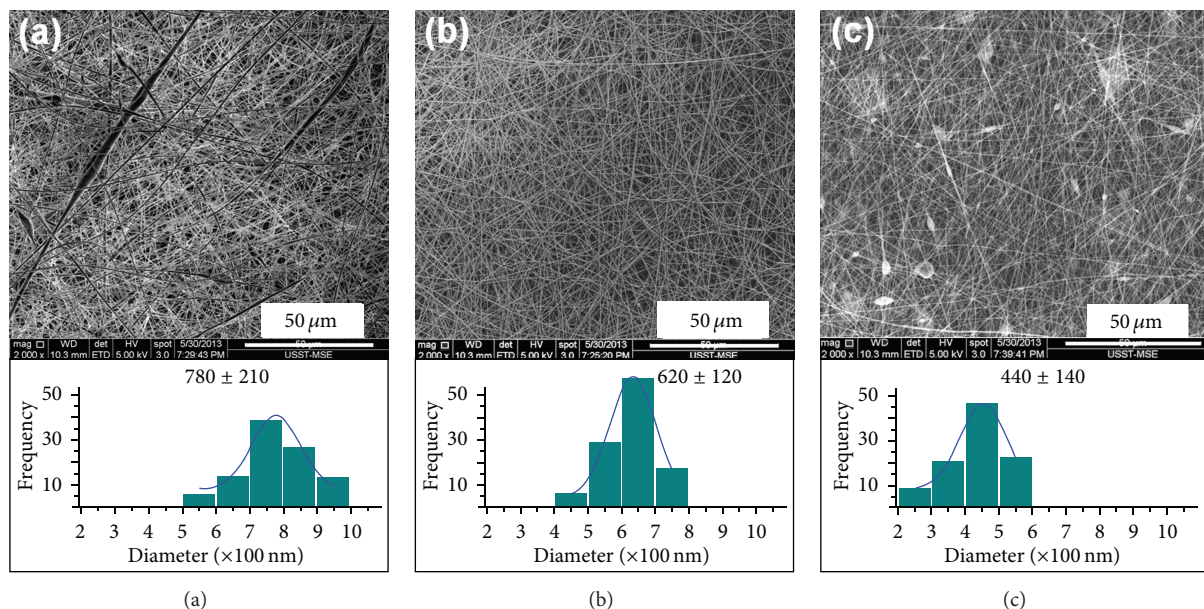


FIGURE 3: The FESEM images of nanofibers F1 (a), F2 (b), and F3 (c), which were generated under different sheath-to-core flow rate ratio of 0, 0.11, and 0.25, respectively. The total flow rate of sheath and core fluid was 1.0 mL/h.

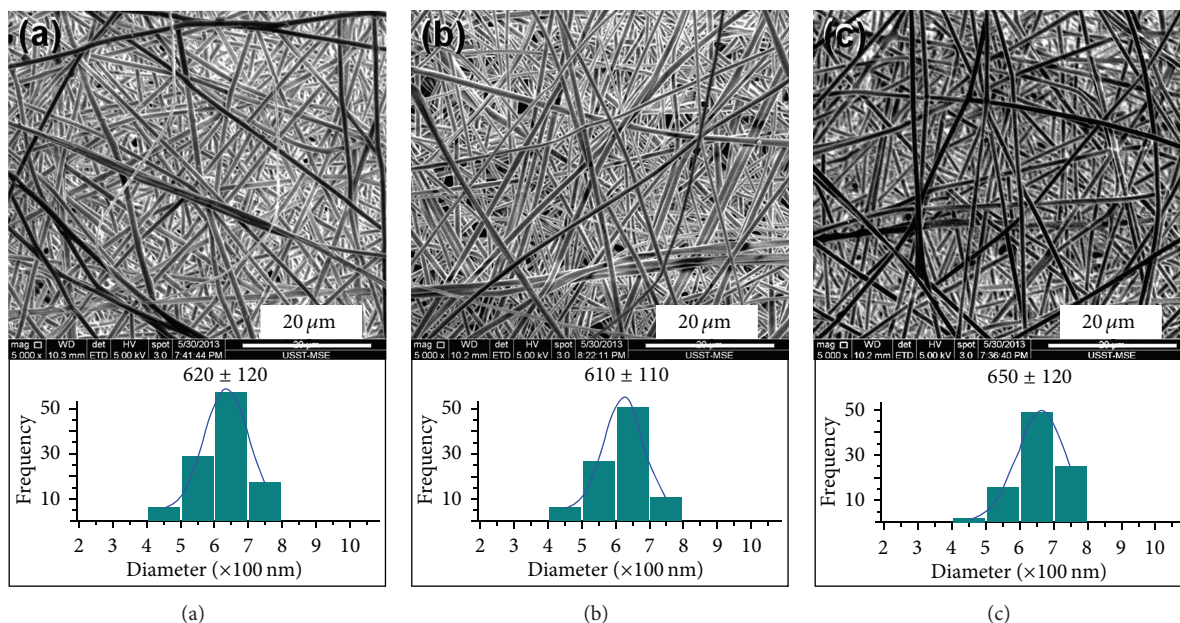


FIGURE 4: The FESEM images of nanofibers F2 (a), F4 (b), and F5 (c), which were generated under a sheath-to-core flow rate ratio of 0.11 and a total flow rate from the spinneret of 1.0 mL/h.

than in the double and triple-component nanofibers. Certainly, hydrophobic interactions could be speculated to be formed between PAN and PVP due to long carbon chains. Additionally, the typical peak of PAN at 2243 cm^{-1} gradually diminished with the content of PVP which increased from 0% to 22.7%, as indicated by the ellipse in Figure 7.

3.4. The In Vitro Drug Release Profiles. The *in vitro* release profiles of IBU from the composite nanofibers are shown in

Figure 8. In the first hour, 36.3%, 35.7%, and 37.7% of the loaded IBU were released from the composite nanofibers F2, F4, and F5, respectively. The initial burst effect of the triple-components composite nanofibers F2 and F5 was slightly larger than that of double-component nanofibers, which should be attributed to the hydrophilic property and easy dissolution of PVP.

After 10 h *in vitro* dissolution tests, 83.7%, 68.3%, and 87.4% of the contained IBU was released into the dissolution medium for nanofibers F2, F4, and F5, respectively. And

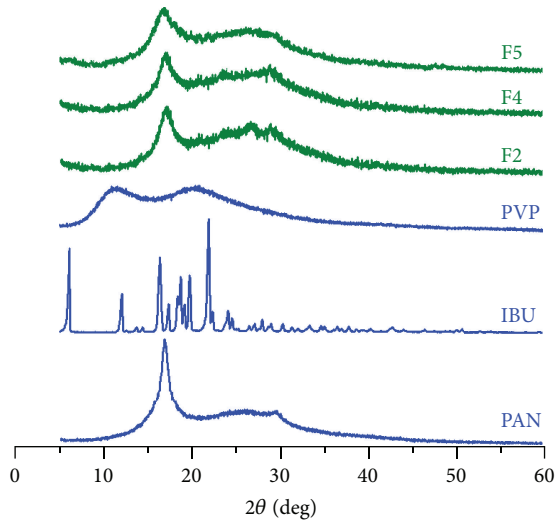


FIGURE 5: XRD patterns of the raw materials and their composite nanofibers.

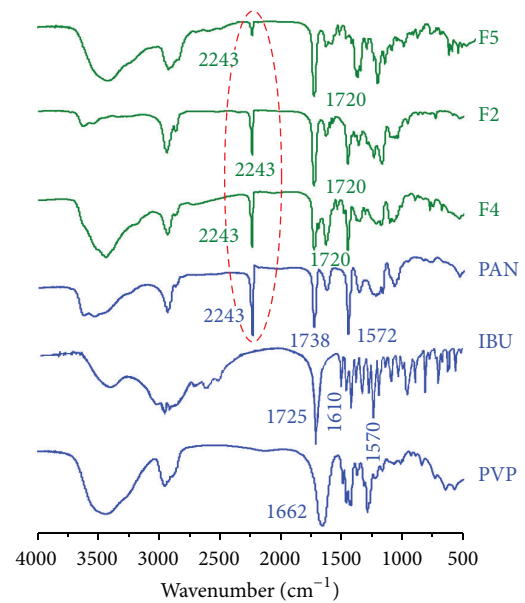


FIGURE 7: FTIR spectra of the raw materials and their composite nanofibers.

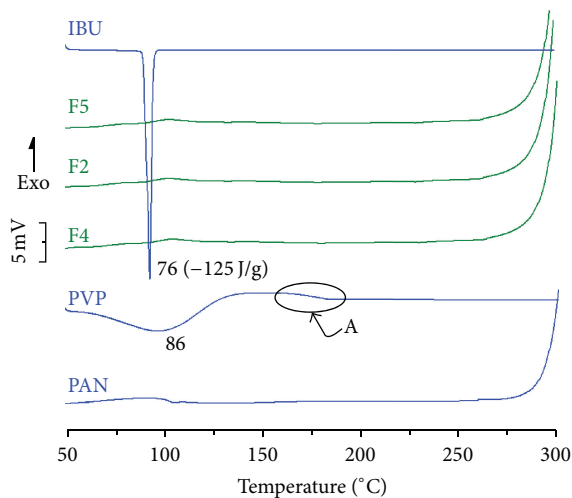


FIGURE 6: DSC thermograms of the components and their composite nanofibers.

after 36 h *in vitro* dissolution tests, 92.1%, 73.4%, and 97.8% of the contained IBU were released out for nanofibers F2, F4, and F5, respectively. These results demonstrate that the triple-component composite nanofibers F2 and F5 have advantages over the double-component products F4 in that more active pharmaceutical ingredients can release out from the nanofibers during a certain time period. PVP not only is a hydrophilic polymer but also has good compatibility with the drug IBU (forming hydrogen bonding with IBU) and the electrospinning process (electrospinnable polymer) as well. During the *in vitro* dissolution processes, PVP could act as the pore-forming agent to form passages for the IBU entrapped in the inner part of the fibers to be gradually released out via diffusion mechanisms and thus facilitates the exhaustion process of loaded IBU from the fibers matrix and avoids the total entrapment in the insoluble PAN molecules.

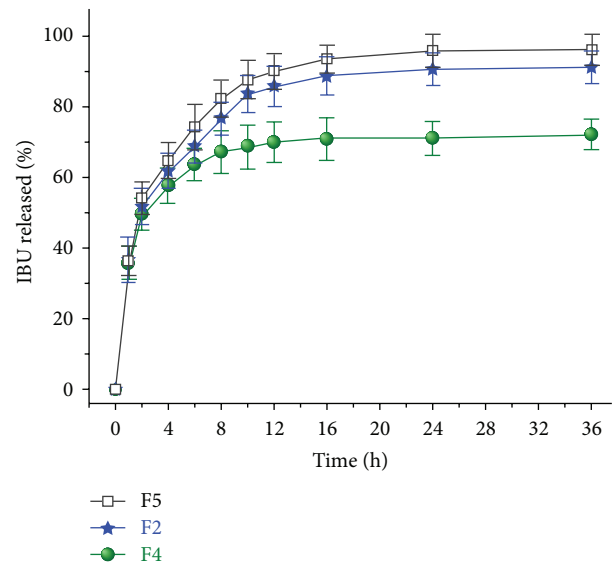


FIGURE 8: *In vitro* drug release profiles.

4. Conclusions

This study experimented a new coaxial electrospinning process on smoothing the preparation of functional nanocomposites composed of multiple components. The sheath-to-core flow rate ratio is a key parameter for successfully carrying out the modified process and generating nanofibers with high quality. Under a condition of a sheath-to-core flow rate ratio of 0.11 and a sheath and core total fluid rate of 1.0 mL/h, IBU/PVP/PAN triple-component nanocomposites with uniform structure and an average diameter of 620 ± 120 nm and 650 ± 120 nm were created when the PVP contents were 10.5% and 22.7%, respectively. Compared

to the IBU/PAN double-component composites, the triple-component composites significantly improved the drug *in vitro* release profiles, efficaciously avoiding the entrapment of IBU in the insoluble PAN molecules in the IBU/PAN nanofibers. The modified coaxial process and the multiple-component nanocomposites would provide new ways for developing novel drug sustained materials and transdermal drug delivery systems.

Acknowledgments

This work was supported by the National Science Foundation of China (nos. 51373101, 51373100, and 51203090), the Natural Science Foundation of Shanghai (nos. 13ZR1428900 and 12ZR1446700), the Key Project of the Shanghai Municipal Education Commission (no. 13ZZ113), and the Innovation project of the University of Shanghai for Science and Technology (no. 13XGM01).

References

- [1] T. Lin and X. Wang, *Encyclopedia of Nanoscience and Nanotechnology*, American Scientific, Los Angeles, Calif, USA, 2nd edition, 2011.
- [2] L. Ji, Z. Lin, M. Alcoutlabi, and X. Zhang, "Recent developments in nanostructured anode materials for rechargeable lithium-ion batteries," *Energy and Environmental Science*, vol. 4, no. 8, pp. 2682–2689, 2011.
- [3] X. Zhang, L. Ji, O. Toprakci, Y. Liang, and M. Alcoutlabi, "Electrospun nanofiber-based anodes, cathodes, and separators for advanced lithium-ion batteries," *Polymer Reviews*, vol. 51, no. 3, pp. 239–264, 2011.
- [4] Y. Su, Q. Su, W. Liu et al., "Controlled release of bone morphogenetic protein 2 and dexamethasone loaded in core-shell PLLACL-collagen fibers for use in bone tissue engineering," *Acta Biomaterialia*, vol. 8, no. 2, pp. 763–771, 2012.
- [5] D.-G. Yu, X.-X. Shen, C. Branford-White, K. White, L.-M. Zhu, and S. W. Annie Bligh, "Oral fast-dissolving drug delivery membranes prepared from electrospun polyvinylpyrrolidone ultrafine fibers," *Nanotechnology*, vol. 20, no. 5, Article ID 055104, 4 pages, 2009.
- [6] X. Y. Li, X. Wang, D. G. Yu et al., "Electrospun Borneol-PVP nanocomposites," *Journal of Nanomaterials*, vol. 2012, Article ID 731382, 8 pages, 2012.
- [7] L. Ji, Z. Lin, A. J. Medford, and X. Zhang, "In-situ encapsulation of nickel particles in electrospun carbon nanofibers and the resultant electrochemical performance," *Chemistry*, vol. 15, no. 41, pp. 10718–10722, 2009.
- [8] H. Niu, J. Zhang, Z. Xie, X. Wang, and T. Lin, "Preparation, structure and supercapacitance of bonded carbon nanofiber electrode materials," *Carbon*, vol. 49, no. 7, pp. 2380–2388, 2011.
- [9] L. Ji, Z. Lin, B. Guo, A. J. Medford, and X. Zhang, "Assembly of carbon-SnO₂ core-sheath composite nanofibers for superior lithium storage," *Chemistry*, vol. 16, no. 38, pp. 11543–11548, 2010.
- [10] X. Wang, H. Niu, X. Wang, and T. Lin, "Needleless electrospinning of uniform nanofibers using spiral coil spinnerets," *Journal of Nanomaterials*, vol. 2012, Article ID 785920, 9 pages, 2012.
- [11] H. Niu and T. Lin, "Fiber generators in needleless electrospinning," *Journal of Nanomaterials*, vol. 2012, Article ID 725950, 13 pages, 2012.
- [12] D. G. Yu, G. R. Williams, X. Wang, X. K. Liu, H. L. Li, and S. W. A. Bligh, "Dual drug release nanocomposites prepared using a combination of electrospinning and electrospinning," *RSC Advances*, vol. 3, no. 14, pp. 4652–4658, 2013.
- [13] D. G. Yu, X. Wang, X. Y. Li, W. Chian, Y. Li, and Y. Z. Liao, "Electrospun biphasic drug release polyvinylpyrrolidone/ethyl cellulose core/sheath nanofibers," *Acta Biomaterialia*, vol. 9, no. 3, pp. 5665–5672, 2013.
- [14] D. G. Yu, X. Y. Li, X. Wang, W. Chian, Y. Z. Liao, and Y. Li, "Zero-order drug release cellulose acetate nanofibers prepared using coaxial electrospinning," *Cellulose*, vol. 20, no. 1, pp. 379–389, 2013.
- [15] D. G. Yu, W. Chian, X. Wang, X. Y. Li, Y. Li, and Y. Z. Liao, "Linear drug release membrane prepared by a modified coaxial electrospinning process," *Journal of Membrane Sciences*, vol. 428, no. 3, pp. 150–156, 2013.
- [16] E.-R. Kenawy, G. L. Bowlin, K. Mansfield et al., "Release of tetracycline hydrochloride from electrospun poly(ethylene-co-vinylacetate), poly(lactic acid), and a blend," *Journal of Controlled Release*, vol. 81, no. 1-2, pp. 57–64, 2002.
- [17] D.-G. Yu, C. Branford-White, L. Li, X.-M. Wu, and L.-M. Zhu, "The compatibility of acyclovir with polyacrylonitrile in the electrospun drug-loaded nanofibers," *Journal of Applied Polymer Science*, vol. 117, no. 3, pp. 1509–1515, 2010.
- [18] H.-M. Chen and D.-G. Yu, "An elevated temperature electrospinning process for preparing acyclovir-loaded PAN ultrafine fibers," *Journal of Materials Processing Technology*, vol. 210, no. 12, pp. 1551–1555, 2010.
- [19] D.-G. Yu, P. Lu, C. Branford-White, J.-H. Yang, and X. Wang, "Polyacrylonitrile nanofibers prepared using coaxial electrospinning with LiCl solution as sheath fluid," *Nanotechnology*, vol. 22, no. 43, Article ID 435301, 7 pages, 2011.
- [20] H.-L. Nie, Z.-H. Ma, Z.-X. Fan et al., "Polyacrylonitrile fibers efficiently loaded with tamoxifen citrate using wet-spinning from co-dissolving solution," *International Journal of Pharmaceutics*, vol. 373, no. 1-2, pp. 4–9, 2009.
- [21] X. Shen, D. Yu, X. Zhang, C. Branford-White, and L. Zhu, "Preparation and characterization of TAM-loaded HPMC/PAN composite fibers for improving drug-release profiles," *Journal of Biomaterials Science*, vol. 22, no. 16, pp. 2227–2240, 2011.
- [22] X. F. Zhang, D. G. Yu, S. J. Zhu, X. X. Shen, C. Branford-White, and L. M. Zhu, "Investigation of electrospun acyclovir-loaded ultrafine fiber mats," *Journal of Textiles Research*, vol. 30, no. 2, pp. 1–4, 2009.
- [23] S. Agarwal, A. Greiner, and J. H. Wendorff, "Functional materials by electrospinning of polymers," *Progress in Polymer Science*, vol. 38, no. 2, pp. 963–991, 2013.
- [24] D.-G. Yu, L.-D. Gao, K. White, C. Branford-White, W.-Y. Lu, and L.-M. Zhu, "Multicomponent amorphous nanofibers electrospun from hot aqueous solutions of a poorly soluble drug," *Pharmaceutical Research*, vol. 27, no. 11, pp. 2466–2477, 2010.

Research Article

Mechanical Properties of Natural Rubber Nanocomposites Filled with Thermally Treated Attapulgite

Jihu Wang^{1,2} and Dajun Chen¹

¹ College of Material Science and Engineering, Donghua University, Shanghai 201620, China

² College of Chemistry and Chemical Engineering, Shanghai University of Engineering Science, Shanghai 201620, China

Correspondence should be addressed to Dajun Chen; cdj@dhu.edu.cn

Received 20 July 2013; Accepted 19 August 2013

Academic Editor: Shanfeng Wang

Copyright © 2013 J. Wang and D. Chen. This is an open access article distributed under the Creative Commons Attribution License, which permits unrestricted use, distribution, and reproduction in any medium, provided the original work is properly cited.

Natural rubber (NR) nanocomposites were prepared in a double-roller plasticator mixer with purified attapulgite (PAT) or modified attapulgite, which was treated at 450°C (PAT-450) and 850°C (PAT-850) for two hours. The structures of the pristine, purified, and modified attapulgite were characterized by FTIR, TEM, XRD, and BET. The results indicated that the structure of attapulgite changed with the increased temperature. The effects of the PAT treatment and content on the mechanical properties of the NR nanocomposites were also investigated. The results showed that AT increased curing process of natural rubber. A significant improvement in the tensile strength, wearability, and solvent resistance of the nanocomposites was observed with the addition of different types of attapulgite as compared to those of pure NR. Scanning electron microscope images showed that the filler was located at the interface, which induced compatibilization in the immiscible blends. Thermogravimetric analysis revealed a significant improvement in the thermal stability of the NR/PAT nanocomposites.

1. Introduction

Polymer nanocomposites have received considerable attention in recent years because of their diverse nanometer-sized filler particles and a series of special performance. Carbon is a traditional filler because of its ability to reinforce rubber [1–3]. Due to the large amount of mill dust produced during the rubber processing and thus its black color, the production application is limited. The other important filler is silica which can improve the performance of polymer nanocomposites [4, 5]. But the price is very high. Thus, nanoscale fillers such as clay particles [6, 7] (e.g., kaolin [8, 9], montmorillonite [10, 11], attapulgite [12–14], mica [15], etc.) have been introduced and subsequently used in the rubber industry.

Attapulgite (AT) is a natural clay mineral with the ideal structural formula of $\text{Mg}_5\text{Si}_8\text{O}_{20}(\text{OH})_2(\text{OH}_2)_4 \cdot 4\text{H}_2\text{O}$; this formula was first proposed by Bradley in 1940 [16]. AT has attracted considerable attention because of its fiber-like structural morphology, particularly in the adsorption of organics on the clay surfaces [17–19]. This nanostructure results in the outstanding attributes of AT as a reinforcement

and improves the mechanical properties of materials [20–22]. To improve the compatibility between inorganic clay and organic polymer, different coupling agents and acids are used to modify AT surface [23–25]. In situ polymerization is another method frequently used to modify AT [26, 27].

Recently, the heat treatment technique is considered a very important way to modify attapulgite which will change the structure of attapulgite. Water, hydroxyl group, and impurities in attapulgite disappeared after being modified at different temperature. The activity of heat treated attapulgite was improved.

Lai et al. [28] reported that thermally treated attapulgite at different temperature was superior to untreated attapulgite in enhancing the wear resistance of Polytetrafluoroethylene (PTFE). They explained that this behavior was attributed to the effect of heat, improving surface properties of attapulgite and removing water in attapulgite, which resulted in strengthening interactive force between attapulgite and PTFE. Lai et al. [29] used palygorskite to prepared silica powder at different temperature. When the optimum calcination temperature was at 560°C, the silica content, the whiteness, and the specific surface area of the product were 85%, 92%,

TABLE 1: Degradation of AT at different temperatures.

$\text{Mg}_8\text{Si}_{12}\text{O}_{30}(\text{OH})_4 \cdot (\text{H}_2\text{O})_4 \cdot 8\text{H}_2\text{O}$	Veronika	Tartaglione	Chen
$\rightarrow \text{Mg}_8\text{Si}_{12}\text{O}_{30}(\text{OH})_4 \cdot (\text{H}_2\text{O})_4 + 8\text{H}_2\text{O}$	$\sim 92^\circ\text{C}$	$T_{\text{max}} = 110^\circ\text{C}$	65°C
$\rightarrow \text{Mg}_8\text{Si}_{12}\text{O}_{30}(\text{OH})_4 \cdot (\text{H}_2\text{O})_2 + 2\text{H}_2\text{O}$	$\sim 130^\circ\text{C}$	$T_{\text{max}} = 325^\circ\text{C}$	98°C
$\rightarrow \text{Mg}_8\text{Si}_{12}\text{O}_{30}(\text{OH})_4 + 2\text{H}_2\text{O}$	$\sim 249^\circ\text{C}$	$T_{\text{max}} = 535^\circ\text{C}$	230 to 481°C
$\rightarrow \text{MgSiO}_3 + 4\text{SiO}_2 + 2\text{H}_2\text{O}$	$\sim 434^\circ\text{C}$	$T > 780^\circ\text{C}$	595°C

and $308 \text{ m}^2/\text{g}$, respectively. The silica still maintained the fibrous morphology of palygorskite besides a few spherical particles of 10–20 nm in diameter. Gan et al. [30] showed that the natural palygorskite was treated by thermal activation over 100–1000°C for 2 h. The thermal activation increased the phosphate sorption capacity, and the highest phosphate sorption capacity occurred at 700°C . Thermal treatment resulted in significant changes in crystal structure and physicochemical properties of palygorskite.

Vágvölgyi et al. [31] studied the thermal decomposition of AT using a combination of dynamic and controlled rate thermal analyses. Lokanatha et al. [32] studied the decomposition of AT. The R.D.F. technique successfully explained the AT structural transformation accompanied dehydration. Frost et al. [33, 34] analyzed the dehydration and dehydroxylation of AT by investigating the thermal degradation via near-infrared and mid-infrared emission spectroscopy over the 100°C to 700°C temperature range. The decomposition processes of attapulgite at different temperatures achieved by Vágvölgyi et al. [31], Tartaglione et al. [35], and Chen et al. [36] are shown in Table 1. The degradation processes and products of AT are the same at different degradation temperatures.

To the best of our knowledge, no study has been conducted on the mechanical properties of natural rubber (NR) nanocomposites filled with AT and modified at different temperatures. In this paper, AT, either purified or modified, was added to NR in different ratios. The properties of the resulting nanocomposites were then investigated. This study aims to determine the effects of AT treatment and filler contents on the mechanical properties of nanocomposites.

2. Experimental Section

2.1. Materials. Attapulgite was provided by Nanjing Yuanda Clay Co. Ltd. Sodium pyrophosphate decahydrate ($\text{Na}_4\text{P}_2\text{O}_7 \cdot 10\text{H}_2\text{O}$) was purchased from Sinopharm Chemical Reagent Co. Ltd. NR was purchased from Hainan. Zinc oxide (ZnO), stearic acid (HSt), 2-mercaptobenzothiazole (accelerator M), diphenyl guanidine (accelerator DM), tetramethylthiuram bisulfide (accelerator TMTD), N-phenyl-2-naphthylamine (antiaging agent D), sulfur (S), and other chemical agents were commercially available.

2.2. Purified and Thermally Treated AT. To remove the impurities in natural AT, 200 g of pulverized pristine AT was immersed in 800 g distilled water to obtain a homogeneous suspension liquid. A total of 6 g of $\text{Na}_4\text{P}_2\text{O}_7 \cdot 10\text{H}_2\text{O}$ was then added to the solution under high mechanical stirring for 30 min. The suspension of the solution was filtered after

24 h at room temperature. The solids were then heated in a vacuum oven for 24 h at 80°C and slowly cooled to room temperature under vacuum to remove moisture. The solids were milled using a ball grinder and subsequently designated as purified attapulgite (PAT).

PAT was treated at 450 and 850°C for 2 h in a muffle furnace. The heat-treated AT was then obtained and pulverized. The samples were designated as PAT-450 and PAT-850.

2.3. Nanocomposite Preparation. In accordance with the experimental formula presented in Table 2, nanocomposites were prepared on a double-roller plasticator with an outside diameter of 470 mm at room temperature. The rotors operated at a speed ratio of 1:1.4. The vulcanization agents were previously added to the elastomer. Different amounts of the filler compatibilizer were then added [0.5, 1, 3, 5, 7, and 10 parts per hundred rubbers (phr)]. Finally, sulfur was added. The nanocomposite of NR/PAT-0.5% means natural rubber filled with 0.5 phr PAT; other nanocomposites were defined similarly.

An oscillating disc rheometer (MDR-2000E, Liyuan, China) was used in a standardized method to measure the curing characteristics of the NR nanocomposites at 150°C . The oscillation exerts a shear strain on the sample, and the torque required to oscillate the sample is proportional to the shear modulus of the rubber. The vulcanization time of the nanocomposites corresponds to the optimum cure time t_{90} , which is derived from the curing curves under 15 MPa pressures on an electrically heated press. The sheeted compounds and abrasion loss samples were placed at 20°C for 24 h prior to testing.

2.4. Characterization. AT combined with oven-dried: spectroscopy grade potassium bromide was finely ground for several minutes under an infrared lamp and was then pressed into a disc. The spectroscopy of each sample was recorded using a Fourier transform infrared spectrometer (FTIR) from 4000 cm^{-1} to 400 cm^{-1} at a resolution of 2 cm^{-1} (Nicolet DosX, Nicolet, America).

The AT powder was dispersed in deionized water under ultrasonic vibration for approximately 30 min and was then deposited on a copper grid. The morphology of the samples was observed using transmission electron microscopy (TEM) measurements (JEM-2100, JEOL, Japan).

The AT powder was scanned from $2\theta = 5^\circ$ to 70° at a rate of $2^\circ/\text{min}$ using an X-ray diffractometer (XRD) (X'Pert PRO, PANalytical, Holland) with $\text{Cu K}\alpha$ radiation ($\lambda = 0.15415 \text{ nm}$) operating under a tube voltage of 45 kV and a tube current of 40 mA.

TABLE 2: Formulations of the rubber compounds.

Ingredients	(phr)
NR	100
HSt	1
ZnO	5
Accelerator M	1.2
Accelerator DM	0.3
Accelerator TMTD	0.2
Antiaging agent D	1
PAT, PAT-450, or PAT-850	0.5, 1, 3, 5, 7, 10
S	2.5

The specific surface area of AT was determined by obtaining the nitrogen adsorption-desorption isotherms at 77 K using a conventional high volumetric system consisting of a TriStar 3000 surface area analyzer (Micromeritics, USA). The Brunauer-Emmett-Teller (BET) method was used for the corresponding calculations.

Tensile tests of the nanocomposites were performed at room temperature using computer-controlled universal testing machines (GT-TCS-2000, Gotech, Taiwan). The tensile speed was 500 mm·min⁻¹. The test samples were prepared in a standard dumbbell shape, and all measurements were repeated five times until a median value was obtained.

The abrasion resistance of the vulcanized rubber nanocomposites was determined using an Akron machine (GT-7012-A, Gotech, Taiwan). The abrasion volume is equal to the sample loss weight divided by the sample's density.

Swelling tests were conducted by using 0.5 g vulcanized nanocomposites, which were immersed in an excess of toluene solution in brown glass bottles until equilibrium was achieved. The swelling indices of the nanocomposites were calculated using the ratio of the weight changes in the samples.

The fracture surfaces of tensile specimens were sprayed with Au to make them conductive. SEM (S-2150, Hitachi, Japan) was used to determine the morphology of the fracture surfaces.

The thermal stability of the nanocomposites was determined using thermogravimetric analysis (TGA, PT1000, Linseis, Germany). The tests were performed at 20°C·min⁻¹ under nitrogen (flow rate, 5 × 10⁻⁷ m³·s⁻¹). The samples were then placed in open silica pans.

3. Results and Discussion

3.1. Fourier Transforms Infrared Spectroscopy. Figure 1 shows the FTIR spectra of AT, PAT, PAT-450, and PAT-850. The spectra show three significant changes. Four hydroxyl-stretching frequencies of natural AT were observed at 3614, 3581, 3552, and 3419 cm⁻¹. The band at 3614 cm⁻¹ is attributed to hydroxyls coordinated with the magnesium [33]. Bands at 3581 and 3552 cm⁻¹ are attributed to the symmetric and anti-symmetric stretching modes of molecular water coordinated with the magnesium at the edges of the channels [33]. The

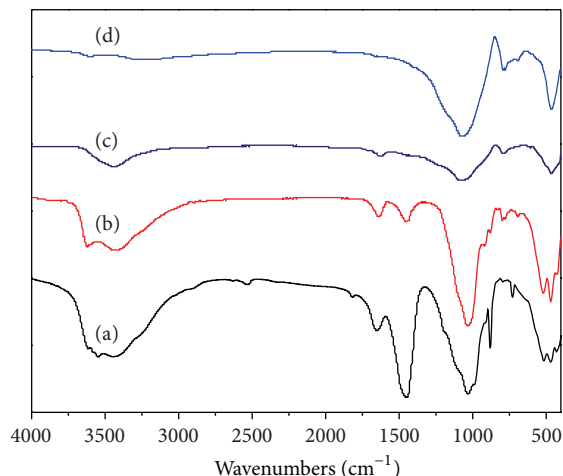


FIGURE 1: Fourier transforms infrared (FTIR) spectra of (a) AT, (b) PAT, (c) PAT-450, and (d) PAT-850.

band at 3419 cm⁻¹ is due to the water in the AT structure [34]. The hydroxyl stretching vibrations of absorbed water is at 1650 cm⁻¹ [37]. The band at 1450 cm⁻¹ is due to the stretching vibration of magnesium oxygen. The bands from 986 cm⁻¹ to 692 cm⁻¹ are due to hydroxyl deformation [37].

Compared with that of pristine AT, the FTIR spectrum of PAT did not change except that the intensity of the band at 1450 cm⁻¹ was weaker and at 1819 cm⁻¹ was disappeared. It might be attributed to impurities which were presented in natural attapulgite.

The intensities of the AT bands at 3614, 3581, 3552, 1650, 1450, and 922 cm⁻¹ to 692 cm⁻¹ decreased, even some bands disappeared when the treatment temperature was set at 450°C [38]. The dehydration of AT is followed by the loss of the peak intensity of the hydroxyl bands of water. Dehydroxylation is followed by the decrease in the peak intensity of the band 3419 cm⁻¹.

The FTIR spectra of the hydroxyl stretching bands of AT disappeared when the temperature was set at 850°C. The figure clearly shows the decrease in the intensity of these bands as the temperature increases. However, the band at 1034 cm⁻¹ remains prominent and is attributed to Si–O stretching even at 850°C [39]. The intensities of the 692 and 465 cm⁻¹ bands are also maintained. These two bands are not lost because they are associated with the OH translation peak and O–Si–O bend vibration peak, respectively [40].

3.2. Transmission Electron Microscopy. Figure 2 shows the TEM images of AT, PAT, PAT-450, and PAT-850. Numerous impurities are present in natural AT, which exhibits a fibrous structure. However, some fibers agglomerate to form AT rods (Figure 2(a)). After purification (Figure 2(b)), the TEM micrograph shows that the AT particles are highly dispersed as individual rod-like structures with an average diameter of 20 nm and a length of 500 nm to 1000 nm, without any aggregation. But the AT structure was changed with the treatment at higher temperature. There were two morphologies

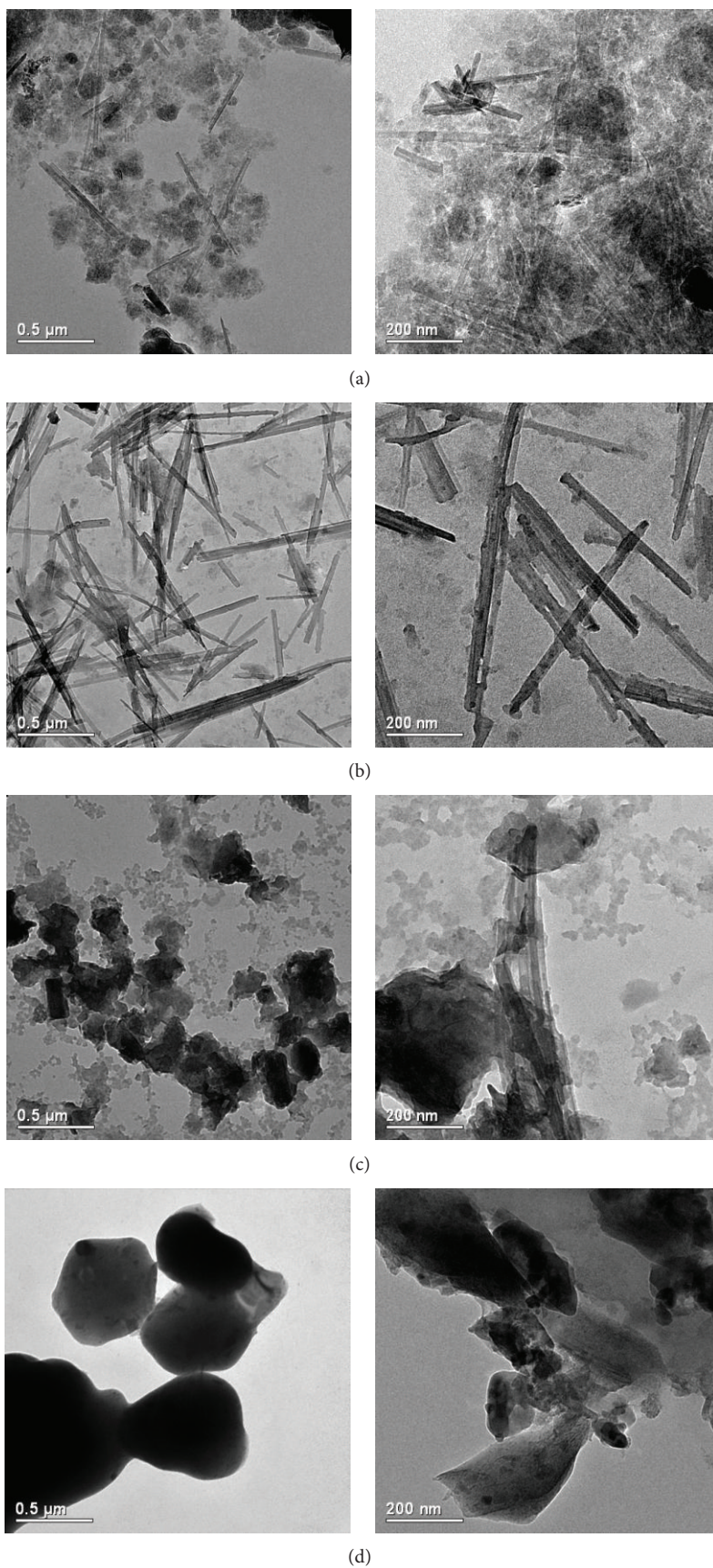


FIGURE 2: Transmission electron microscopy (TEM) images of (a) AT, (b) PAT, (c) PAT-450, and (d) PAT-850.

that included fibrous and agglomerated $\text{Mg}_8\text{Si}_{12}\text{O}_{30}(\text{OH})_4$ particles from TEM (Figure 2(c)) when the treatment temperature was set at 450°C . The structures of some AT particles changed from fibrous to agglomerated $\text{Mg}_8\text{Si}_{12}\text{O}_{30}(\text{OH})_4$ particles because of AT decomposition which caused some holes to disappear and destroyed a part of the microstructure of AT [36]. When the temperature reached 850°C , the fibrous structure was not found, and the amount of agglomerated particles gradually increased (Figure 2(d)). The heat-treated attapulgite powders decomposed into silica and magnesium silicate at 850°C [31, 35]. The results showed that the sintering phenomenon was formed entirely by heating for 2 h at 850°C [36].

3.3. X-Ray Diffraction (XRD). The XRD patterns of AT, PAT, PAT-450, and PAT-850 are shown in Figure 3. The peaks at $2\theta = 8.5^\circ, 13.93^\circ, 19.70^\circ,$ and 26.5° correspond to the primary diffraction of the (110), (200), (040), and (400) planes of AT, respectively [35, 41]. Meanwhile, the characteristic peaks of the four planes of AT and PAT showed no change. Melo et al. [42] reported that treatment at 450°C had little effect on the crystal structure of AT. However, there were two morphologies of PAT-450 that included fibrous and agglomerated $\text{Mg}_8\text{Si}_{12}\text{O}_{30}(\text{OH})_4$ particles. The intensity of peak at $2\theta = 8.5^\circ$ was weaker compared with PAT and PAT-450 which due to some holes in PAT-450 disappeared. But the other characteristic peaks of PAT-450 were not obviously changed. This phenomenon might be the characteristic diffraction peaks between $\text{Mg}_8\text{Si}_{12}\text{O}_{30}(\text{OH})_4$ and attapulgite that were overlapped. The crystal structure of AT was destroyed at 850°C . The characteristic diffraction peaks of attapulgite at 8.5° and 19.7° disappeared, indicating the change in the crystal structure of AT as well as the disappearance of its interlayer space [38]. The reflection at $2\theta = 26.7^\circ$ was due to the formation of amorphous silica [29]. This result is consistent with the TEM image of PAT-850.

3.4. BET Specific Surface Areas. The specific surface areas (calculated using the BET equation) of the different AT samples are shown in Table 3. Before and after the purification treatment, the surface areas of the AT were 143 and $126\text{ m}^2/\text{g}$, respectively. The surface area of PAT was reduced compared with the original AT. Some impurities in AT may have adsorbed nitrogen. After purification, they were removed from AT, which resulted in the significant decrease in the surface area of PAT. Specific surface area of AT decreased as the temperature increased. When the temperature was set at 450°C , the surface area of PAT-450 further decreased to $80\text{ m}^2/\text{g}$. The reason for such manifestation is that some AT particles changed from fibrous to agglomerated $\text{Mg}_8\text{Si}_{12}\text{O}_{30}(\text{OH})_4$ particles produced from AT decomposed, which caused some holes to disappear and destroy the microstructure of AT. As a result, the specific surface areas were reduced.

The surface area of PAT-850 rapidly decreased to $0.6\text{ m}^2/\text{g}$ at 850°C . This decrease can be explained in two ways. One is that the PAT-850 structure was entirely destroyed and the holes completely disappeared. At higher temperatures,

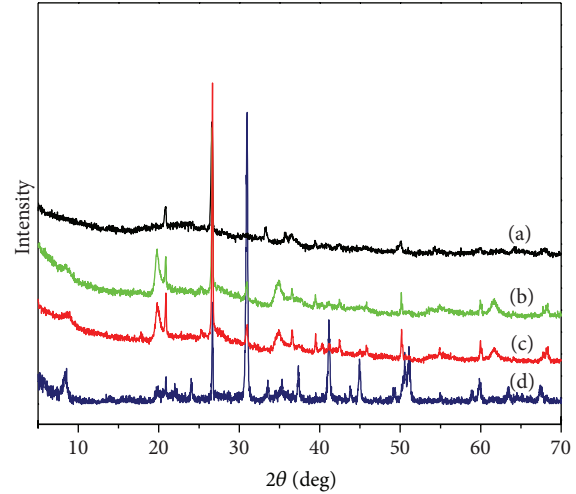


FIGURE 3: X-ray diffraction (XRD) patterns of (a) PAT-850, (b) PAT-450, (c) PAT, and (d) AT.

TABLE 3: Specific surface areas of AT, PAT, PAT-450, and PAT-850.

Sample	AT	PAT	PAT-450	PAT-850
Specific surface area (m^2/g)	143	126	80	0.6

fibers became shrunken and curled, intra- and interparticles sintered, and the structure folded and pores were blocked resulting from decomposing and collapsing of the layers of the attapulgite [33]. Another factor was that the aggregation of the PAT-850 particles dramatically increased.

3.5. Rheometric Characteristics of NR/PAT Nanocomposites. The rheometric characteristics of the different NR nanocomposites are shown in Table 4, where M_L , M_H , t_{s2} , and t_{90} were minimum torque, maximum torque, scorch time, and optimum cure time, respectively. The results showed that each nanocomposite exhibited different cure characteristics due to different properties of the fillers. The ΔM was the rough measurement of the cross-linking degree of rubber during vulcanization which could be used as an indirect indication of the cross-link density of the rubber compound [43, 44]. Nanocomposites loading different AT caused a significant decrease in t_{90} and t_{s2} and increased in M_L and M_H compared with pristine natural rubber. It was revealed that AT increase curing process of natural rubber.

Table 4 indicated that the values of M_L , M_H , and ΔM increase continuously with PAT content increase. The increment in the torque with PAT content was due to the presence of more fibres structure which imparted more restriction to the deformation and consequently increased the NR/PAT composites stiffness. The larger the surface area is, the greater the interaction between the filler and rubber matrix is [45]. The structure of the PAT-450 particles contains fibers and $\text{Mg}_8\text{Si}_{12}\text{O}_{30}(\text{OH})_4$ particles, which promoted particle dispersion in rubber. This dispersal showed that the interfacial interaction between PAT-450 and the NR matrix as well as the cross-linking density of the composite increased. The

TABLE 4: Curing properties of the NR/PAT nanocomposites.

Sample	t_{s_2} (s)	t_{90} (s)	M_L (N·m)	M_H (N·m)	$\Delta M = M_H - M_L$ (N·m)
NR	91 ± 3	207 ± 5	0.01 ± 0.00	0.53 ± 0.02	0.52 ± 0.02
NR/PAT-0.5%	46 ± 2	76 ± 3	0.02 ± 0.01	0.56 ± 0.03	0.54 ± 0.04
NR/PAT-1%	56 ± 3	105 ± 3	0.03 ± 0.01	0.61 ± 0.02	0.57 ± 0.03
NR/PAT-3%	58 ± 2	113 ± 2	0.03 ± 0.01	0.63 ± 0.03	0.60 ± 0.04
NR/PAT-5%	69 ± 3	115 ± 2	0.03 ± 0.01	0.64 ± 0.03	0.61 ± 0.04
NR/PAT-10%	75 ± 4	116 ± 4	0.04 ± 0.01	0.75 ± 0.02	0.71 ± 0.03
NR/PAT-450-0.5%	43 ± 2	72 ± 4	0.02 ± 0.01	0.58 ± 0.03	0.56 ± 0.04
NR/PAT-450-1%	51 ± 3	74 ± 3	0.03 ± 0.01	0.62 ± 0.02	0.60 ± 0.03
NR/PAT-450-3%	52 ± 3	74 ± 2	0.03 ± 0.01	0.63 ± 0.03	0.60 ± 0.04
NR/PAT-450-5%	56 ± 2	105 ± 4	0.03 ± 0.01	0.69 ± 0.02	0.66 ± 0.03
NR/PAT-450-10%	56 ± 3	106 ± 3	0.04 ± 0.01	0.74 ± 0.02	0.70 ± 0.03
NR/PAT-850-0.5%	45 ± 2	68 ± 3	0.02 ± 0.01	0.64 ± 0.03	0.62 ± 0.04
NR/PAT-850-1%	46 ± 3	69 ± 2	0.03 ± 0.01	0.65 ± 0.02	0.62 ± 0.03
NR/PAT-850-3%	50 ± 3	69 ± 4	0.03 ± 0.01	0.67 ± 0.03	0.64 ± 0.04
NR/PAT-850-5%	52 ± 2	75 ± 3	0.03 ± 0.01	0.70 ± 0.02	0.67 ± 0.03
NR/PAT-850-10%	54 ± 3	111 ± 5	0.04 ± 0.01	0.73 ± 0.02	0.69 ± 0.03

TABLE 5: Mechanical properties of the NR/PAT nanocomposites.

Sample	Stress at 300% (MPa)	Elongation at break (%)	Tensile strength (MPa)	Shore hardness (SHA)	Abrasion volume (cm ³)
NR	1.60 ± 0.04	592 ± 18	15.45 ± 0.51	46 ± 1	1.155 ± 0.013
NR/PAT-0.5%	1.64 ± 0.05	415 ± 15	19.34 ± 0.56	46 ± 1	0.723 ± 0.015
NR/PAT-1%	2.07 ± 0.07	432 ± 15	23.27 ± 0.45	50 ± 2	0.659 ± 0.014
NR/PAT-3%	1.59 ± 0.07	431 ± 16	21.23 ± 0.52	47 ± 1	0.765 ± 0.015
NR/PAT-5%	1.68 ± 0.05	427 ± 17	20.40 ± 0.63	50 ± 1	0.812 ± 0.016
NR/PAT-10%	1.39 ± 0.06	425 ± 14	16.69 ± 0.46	46 ± 2	1.061 ± 0.017
NR/PAT-450-0.5%	2.44 ± 0.07	397 ± 16	24.45 ± 0.45	52 ± 2	0.235 ± 0.012
NR/PAT-450-1%	2.53 ± 0.08	418 ± 14	29.69 ± 0.41	54 ± 1	0.043 ± 0.009
NR/PAT-450-3%	2.84 ± 0.07	397 ± 18	26.60 ± 0.33	54 ± 1	0.333 ± 0.012
NR/PAT-450-5%	3.86 ± 0.08	356 ± 14	25.03 ± 0.57	58 ± 2	0.336 ± 0.011
NR/PAT-450-10%	3.15 ± 0.08	354 ± 17	23.27 ± 0.64	54 ± 2	0.340 ± 0.012
NR/PAT-850-0.5%	1.85 ± 0.05	466 ± 18	23.45 ± 0.53	50 ± 1	0.324 ± 0.013
NR/PAT-850-1%	2.03 ± 0.05	481 ± 13	28.63 ± 0.47	51 ± 2	0.135 ± 0.012
NR/PAT-850-3%	1.96 ± 0.05	452 ± 17	25.21 ± 0.66	51 ± 1	0.429 ± 0.014
NR/PAT-850-5%	2.20 ± 0.07	434 ± 18	24.04 ± 0.35	52 ± 2	0.438 ± 0.013
NR/PAT-850-10%	1.33 ± 0.07	412 ± 15	19.93 ± 0.57	47 ± 1	0.954 ± 0.015

larger ΔM of NR/PAT-850 showed the stronger interactions between SiO₂ particles and natural rubber which were abundant –OH groups on the surface of the SiO₂.

It could be found that the scorch time and optimum cure time of nanocomposites increased with increasing filler loading. At a similar filler loading, PAT exhibited longer t_{s_2} and t_{90} than PAT-450 and PAT-850. One reason was that the high specific surface areas and the charges on the lattice allowed the AT to adsorb the vulcanizing and curing agents easily. The adsorption increased as the AT content varied from 0.5% to 10%. Accordingly, contrary to the reduction of accelerator concentration which may be imagined to result in longer scorch time. The other reason was that AT contained

a large number of bound water and hydroxyl groups on the surface of attapulgite; they could adsorb the curatives and also caused delay of the t_{s_2} and t_{90} of rubber compound. The scorch time and optimum cure time of NR/PAT-850 were increased possibly due to amorphous silica containing hydroxyl groups (–OH) [46] which absorbs the curative agents and thus reduce the active sulphurating agent.

3.6. Mechanical Properties of the NR/PAT Nanocomposites. The mechanical properties of the AT-filled systems are shown in Table 5. Mechanical properties of NR/PAT nanocomposites like tensile strength and elongation at break increased

with the increase in filler loading up to 1 phr, thereafter these properties marginally fall when loading is increased to 10 phr. However, the abrasion volume showed an opposite tendency to that of the nanocomposite tensile properties. Lower amounts of AT can easily disperse in the nanocomposites. This may be attributed to a significant improvement in the filler matrix-interfacial bonding, better dispersion of the filler in the blend, which leads to an increased in the efficiency of stress transfer from the matrix to the filler phases. With increasing AT concentration, the tensile properties decreased. This means that addition of more AT concentration seems to cause agglomeration and interruption filler-matrix bonding. The optimum loading of AT appears to be one per one hundred rubber. The results also show that thermally-treated AT exhibited an improved dispersion and enhanced the chemical interfacial adhesion with the matrix, which exhibited “nanometer effect” and “physical cross-link” of attapulgite [47].

NR/PAT-450 had a positive effect on the nanocomposite tensile properties, which reached 29.69 MPa when 1 wt% filler was added to NR. This result indicates a 100% improvement compared with pure NR. It also can be found that PAT-850 had a good reinforce filler for natural rubber. Such improvement is attributed to PAT decomposing into amorphous silica at 850°C. Silica is one of the reinforcing fillers widely used in rubber compounds [48, 49].

3.7. Swelling Ratio of NR/PAT Nanocomposites. The swelling ratio of the NR/PAT nanocomposites in toluene was investigated; the results are shown in Figure 4. The first section of the swelling ratio curves revealed the high swelling rate because of the large concentration gradients, and the samples are under severe solvent stress, whereas the second section indicated a reduced swelling rate due to a decrease in concentration gradient, and the swelling process almost reached equilibrium.

The swelling test results indicate some type of relationship with the tensile properties of the NR composites. The NR/PAT nanocomposites exhibited significantly lower swelling ratios compared with NR in the absence of filler. In particular, the nanocomposite with PAT-450 content of 1 wt% exhibited the lowest swelling ratio, which indicated that penetration of toluene solvent into rubber compound was restricted. The nanocomposites filled with PAT, PAT-450, and PAT-850 reached the swelling equilibrium after 24 h, whereas the NR required 50 h to reach the same state. As a result, PAT could provide a barrier system against toluene solvent. This may be attributed to the uniform dispersion of PAT particles in natural rubber matrix, thus contributing to better rubber-filler interaction [50, 51].

3.8. SEM Analysis. The morphologies of the fracture surface of the NR/PAT nanocomposites were examined by SEM. Figure 5(a) showed the SEM micrograph of pristine NR. The fractured section of pristine NR was smooth, while those of NR/PAT nanocomposites showed many irregularities (Figures 5(b), 5(c), and 5(d)). The morphology of the fracture surface of NR/PAT-1% nanocomposite was showed

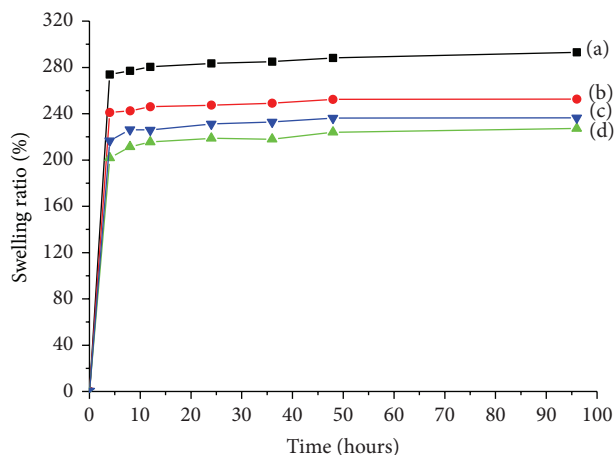


FIGURE 4: Swelling of various nanocomposites with the variations in the modified AT (a) NR, (b) NR/PAT-1%, (c) NR/PAT-450-1%, and (d) NR/PAT-850-1%.

in Figure 5(b). The NR matrix was in gray, the attapulgite was in white, and the attapulgite fibers were dispersed uniformly in NR. The nanocomposite exhibited fibrous morphology, and a great deal of attapulgite fibers congregate into bundles. Most PAT fibrils were fractured and only a few fibrils were pulled out from the NR matrix [21]. This implies that the adhesion between PAT and the NR matrix is good [47].

The morphology of the fracture surface of NR/PAT-450-1% and NR/PAT-850-1% nanocomposite was showed in Figures 5(c) and 5(d), respectively. When Figures 5(b), 5(c), and 5(d) were compared, the results demonstrated that the fracture surface of NR/PAT450-1% was the roughest with deeper tearing lines and angular cracking. In addition, the interface between PAT-450 and the natural rubber matrix was not so clear. Similarly, the fracture surface of NR/PAT450-1% nanocomposite was a few smaller holes, which indicated that the interfacial adhesion was still strong. Higher crack propagation energy was required to fracture this nanocomposite.

It also could be clearly seen that there were some big microcracks in the fracture surface of NR/PAT-850-1%, which is due to PAT decomposing into amorphous silica at 850°C. The interfacial bonding between silica and the rubber matrix was strong, thus resulting in higher values of tensile properties [52].

3.9. Thermogravimetric Analysis of the NR/PAT Nanocomposites. The thermal behavior of the nanocomposites was investigated using TG; the results are shown in Figure 6. The temperatures of $T_{5\%}$ and T_{\max} values of nanocomposites were listed in Table 6. These TG curves indicated single-stage degradation with well defined initial and final degradation temperatures and might have been a result of a random chain scission process [53]. The nanocomposites filled with PAT, PAT-450, and PAT-850 displayed better thermal resistance than that of the pristine NR. $T_{5\%}$ and T_{\max} values for NR, NR/PAT-1%, NR/PAT-450-1%, and NR/PAT-850-1% were found to occur at 215, 285, 309, and 338°C and 374, 393, 391, and 395°C, respectively. Table 6 showed a 70–113°C

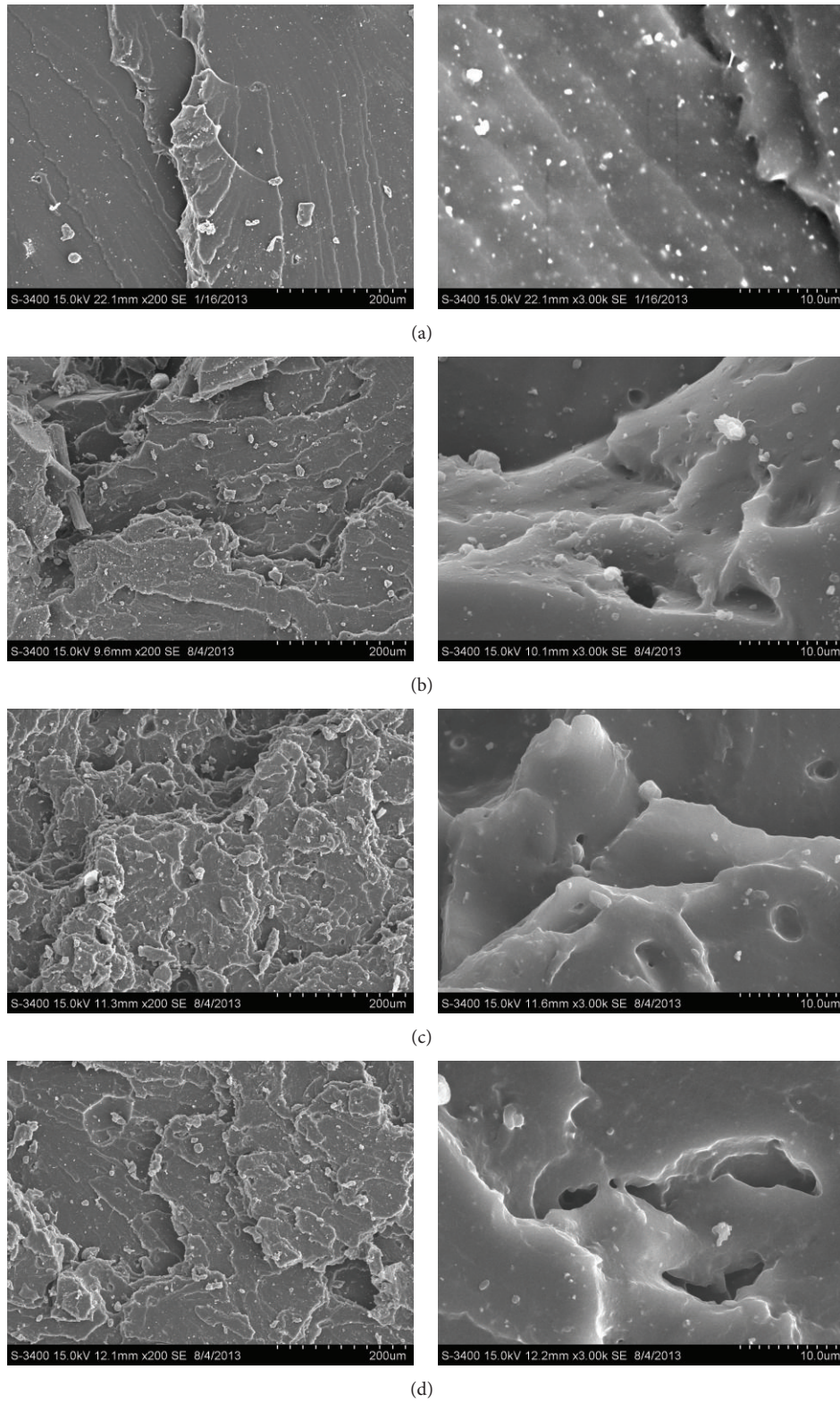


FIGURE 5: Fractographs of various nanocomposites with the variations in the modified AT (a) NR, (b) NR/PAT-1%, (c) NR/PAT-450-1%, and (d) NR/PAT-850-1%.

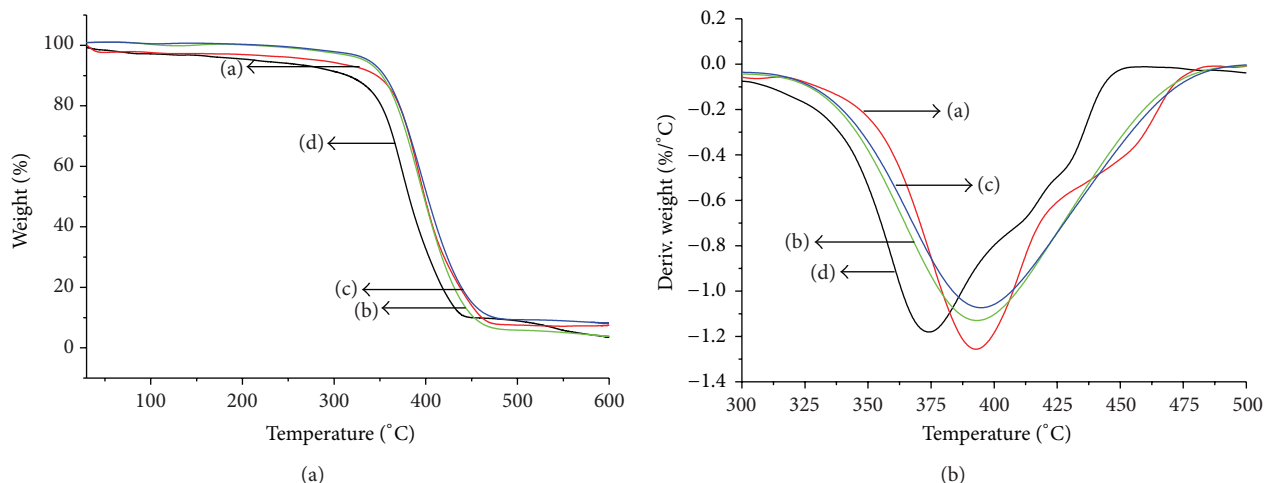


FIGURE 6: Thermograms of NR and NR/AT nanocomposites: (a) NR/PAT-1%, (b) NR/PAT-450-1%, (c) NR/PAT-850-1%, and (d) NR.

TABLE 6: Thermal degradation of the NR/PAT nanocomposites.

Sample	Initial degradation temperature (°C) $T_{5\%}$	Degradation temperature (°C) T_{max}	Residue mass at 600°C (%)
NR	215	374	3.58
NR/PAT-1%	285	393	7.43
NR/PAT-450-1%	309	391	7.57
NR/PAT-850-1%	338	395	8.13

increase in the initial degradation temperature and a 17–21°C increase in the degradation temperature of nanocomposites filled with PAT, PAT-450, and PAT-850. Attapulgite particles retarded the motion of the polymer chains, acted as insulators, and massed transport barriers to volatile products produced during thermal degrading which could enhance the thermal stability of polymer [47, 54]. Four different types of hydroxyl group are present in PAT. Meanwhile, zeolitic and coordinated water are found in PAT-450. As the temperature increased, the moisture was gradually volatilized. The heat conduction coefficients of the nanocomposites increased, whereas the heat transfer speed decreased. At the same time, the heat of the nanocomposites dissipated during moisture evaporation. PAT-850 improved the molecular interaction between AT and rubber and contributed in preventing the thermal degradation of rubber.

4. Conclusions

Pristine attapulgite was purified and modified attapulgite, which was treated at 450°C and 850°C for two hours. The structures and morphology of heated attapulgite was changed. NR nanocomposites reinforced with different AT were prepared using a direct melt-compounding method. A comparative study was performed to evaluate the effects of rheometric characteristics and mechanical properties of the

NR/AT nanocomposites. The t_{90} , ts_2 , M_L , M_H , and ΔM of the nanocomposites increased with increasing AT content. The tensile strength, abrasion resistance, and solvent resistance properties of the nanocomposites were significantly improved by the addition of PAT, PAT-450, or PAT-850. SEM results show that the filler is located at the interface among the natural rubber. TGA results show that the significantly improved thermal stability of nanocomposites.

Conflict of Interests

The authors declare that there is no conflict of interests regarding the publication of this paper.

Acknowledgments

This work was financially supported by the Science and Technology Development Foundation of Shanghai University of Engineering Science (2011XY23), Shanghai Municipality Science and Technology Commission Foundation (11490501500), and Shanghai Municipal Education Commission Foundation (11XK18B and XKCZ1205).

References

- [1] K. W. Stöckelhuber, A. Das, R. Jurk, and G. Heinrich, "Contribution of physico-chemical properties of interfaces on dispersibility, adhesion and flocculation of filler particles in rubber," *Polymer*, vol. 51, no. 9, pp. 1954–1963, 2010.
- [2] Y. Merckel, J. Diani, M. Brieu, and J. Caillard, "Effects of the amount of fillers and of the crosslink density on the mechanical behavior of carbon-black filled styrene butadiene rubbers," *Journal of Applied Polymer Science*, vol. 129, no. 4, pp. 2086–2091, 2013.
- [3] H. Nabil, H. Ismail, and A. R. Azura, "Compounding, mechanical and morphological properties of carbon-black-filled natural rubber/recycled ethylene-propylene-diene-monomer (NR/R-EPDM) blends," *Polymer Testing*, vol. 32, no. 2, pp. 385–393, 2013.

- [4] S. Agnelli, G. Ramorino, S. Passera, J. Karger-Kocsis, and T. Ricco, "Fracture resistance of rubbers with MWCNT, organoclay, silica and carbon black fillers as assessed by the J-integral: effects of rubber type and filler concentration," *Express Polymer Letters*, vol. 6, no. 7, pp. 581–587, 2012.
- [5] Z. Peng, L. X. Kong, S.-D. Li, Y. Chen, and M. F. Huang, "Self-assembled natural rubber/silica nanocomposites: its preparation and characterization," *Composites Science and Technology*, vol. 67, no. 15–16, pp. 3130–3139, 2007.
- [6] C. A. Rezende, F. C. Bragança, T. R. Doi, L.-T. Lee, F. Galembeck, and F. Boué, "Natural rubber-clay nanocomposites: mechanical and structural properties," *Polymer*, vol. 51, no. 16, pp. 3644–3652, 2010.
- [7] M. N. Qureshi and H. Qammar, "Mill processing and properties of rubber-clay nanocomposites," *Materials Science and Engineering C*, vol. 30, no. 4, pp. 590–596, 2010.
- [8] A. Lagazzo, S. Lenzi, R. Botter, P. Cirillo, F. Demicheli, and D. T. Beruto, "A rheological method for selecting nano-kaolin powder as filler in SBR rubber," *Particuology*, vol. 8, no. 3, pp. 245–250, 2010.
- [9] Y. Zhang, Q. Liu, Q. Zhang, and Y. Lu, "Gas barrier properties of natural rubber/kaolin composites prepared by melt blending," *Applied Clay Science*, vol. 50, no. 2, pp. 255–259, 2010.
- [10] S. L'aliková, M. Pajtášová, M. Chromčíková et al., "Investigation of natural rubber composites with addition of montmorillonite fillers using thermal analysis," *Journal of Thermal Analysis and Calorimetry*, vol. 104, no. 3, pp. 969–973, 2011.
- [11] Z. M. Jia, S. J. Chen, and J. Zhang, "RTV silicone rubber filled with surface modified montmorillonite," *Journal of Macromolecular Science B*, no. 51, pp. 2449–2461, 2012.
- [12] Q. Fu, L. Chen, K. Liu, F. Chen, and T. X. Jin, "Rod like attapulgite/poly(ethylene terephthalate) nanocomposites with chemical bonding between the polymer chain and the filler," *EXPRESS Polymer Letters*, vol. 6, no. 8, pp. 629–638, 2012.
- [13] N. A. Azahari, N. Othman, and H. Ismail, "Effect of attapulgite clay on biodegradability and tensile properties of polyvinyl alcohol/corn starch blend film international," *Journal of Polymeric Materials*, no. 61, pp. 1065–1078, 2012.
- [14] J. Shi, X. Yang, Q. Han, X. Wang, and L. Lu, "Polyurethane grafted attapulgite as novel fillers for nylon 6 nanocomposites," *Journal Wuhan University of Technology, Materials Science Edition*, vol. 26, no. 4, pp. 615–619, 2011.
- [15] R. M. B. Fernandes, L. L. Y. Visconte, and R. C. R. Nunes, "Characteristics of acrylic rubber composites with mica and carbon black," *Journal of Elastomers and Plastics*, vol. 42, no. 1, pp. 65–74, 2010.
- [16] W. F. Bradley, "The structural scheme of attapulgite," *American Mineralogist*, vol. 25, no. 6, pp. 405–410, 1940.
- [17] P. Liu and T. Wang, "Adsorption properties of hyperbranched aliphatic polyester grafted attapulgite towards heavy metal ions," *Journal of Hazardous Materials*, vol. 149, no. 1, pp. 75–79, 2007.
- [18] J. Zhang, Q. Wang, and A. Wang, "Synthesis and characterization of chitosan-g-poly(acrylic acid)/attapulgite superabsorbent composites," *Carbohydrate Polymers*, vol. 68, no. 2, pp. 367–374, 2007.
- [19] C. H. Chen, "Effect of attapulgite on the crystallization behavior and mechanical properties of poly(butylene succinate) nanocomposites," *Journal of Physics and Chemistry of Solids*, vol. 69, no. 5–6, pp. 1411–1414, 2008.
- [20] Y. Chen, Y. Zhao, S. Zhou, X. Chu, L. Yang, and W. Xing, "Preparation and characterization of polyacrylamide/palygorskite," *Applied Clay Science*, vol. 46, no. 2, pp. 148–152, 2009.
- [21] M. Tian, W. Liang, G. Rao, L. Zhang, and C. Guo, "Surface modification of fibrillar silicate and its reinforcing mechanism on FS/rubber composites," *Composites Science and Technology*, vol. 65, no. 7–8, pp. 1129–1138, 2005.
- [22] J. Huang, Y. Liu, and X. Wang, "Influence of differently modified palygorskites in the immobilization of a lipase," *Journal of Molecular Catalysis B*, vol. 55, no. 1–2, pp. 49–54, 2008.
- [23] J. Zhang, H. Chen, and A. Wang, "Study on superabsorbent composite. III. Swelling behaviors of polyacrylamide/attapulgite composite based on acidified attapulgite and organo-attapulgite," *European Polymer Journal*, vol. 41, no. 10, pp. 2434–2442, 2005.
- [24] Y. I. Jin, J. Chen, and Y. H. Qian, "The methodology and mechanism analysis of stearic acid-modified attapulgite reinforcing polyurethane leather," *Journal of Wuhan University of Technology*, vol. 27, no. 12, pp. 9–13, 2005.
- [25] Y. Xiang, Z. Peng, and D. Chen, "A new polymer/clay nanocomposite hydrogel with improved response rate and tensile mechanical properties," *European Polymer Journal*, vol. 42, no. 9, pp. 2125–2132, 2006.
- [26] Y. Liu, P. Liu, Z. Su, F. Li, and F. Wen, "Attapulgite-Fe₃O₄ magnetic nanoparticles via co-precipitation technique," *Applied Surface Science*, vol. 255, no. 5, pp. 2020–2025, 2008.
- [27] Y. Liu, P. Liu, and Z. Su, "Core-shell attapulgite@polyaniline composite particles via in situ oxidative polymerization," *Synthetic Metals*, vol. 157, no. 13–15, pp. 585–591, 2007.
- [28] S. Q. Lai, T. S. Li, X. J. Liu, R. G. Lv, and L. Yue, "The tribological properties of PTFE filled with thermally treated nano-attapulgite," *Tribology International*, vol. 39, no. 6, pp. 541–547, 2006.
- [29] S. Lai, L. Yue, X. Zhao, and L. Gao, "Preparation of silica powder with high whiteness from palygorskite," *Applied Clay Science*, vol. 50, no. 3, pp. 432–437, 2010.
- [30] F. Gan, J. Zhou, H. Wang, C. Du, and X. Chen, "Removal of phosphate from aqueous solution by thermally treated natural palygorskite," *Water Research*, vol. 43, no. 11, pp. 2907–2915, 2009.
- [31] V. Vágvölgyi, L. M. Daniel, C. Pinto, J. Kristóf, R. L. Frost, and E. Horváth, "Dynamic and controlled rate thermal analysis of attapulgite," *Journal of Thermal Analysis and Calorimetry*, vol. 92, no. 2, pp. 589–594, 2008.
- [32] S. Lokanatha, B. K. Mathur, B. K. Samantaray, and S. Bhattacharjee, "Dehydration and phase transformation in attapulgite (palygorskite)—an R.D.F. study," *Journal of Materials Science Letters*, vol. 3, no. 12, pp. 1105–1108, 1984.
- [33] R. L. Frost, G. A. Cash, and J. T. Klopogge, "Rocky Mountain leather, sepiolite and attapulgite—an infrared emission spectroscopic study," *Vibrational Spectroscopy*, vol. 16, no. 2–3, pp. 173–184, 1998.
- [34] R. L. Frost, O. B. Locos, H. Ruan, and J. T. Klopogge, "Near-infrared and mid-infrared spectroscopic study of sepiolites and palygorskites," *Vibrational Spectroscopy*, vol. 27, no. 1, pp. 1–13, 2001.
- [35] G. Tartaglione, D. Tabuani, and G. Camino, "Thermal and morphological characterisation of organically modified sepiolite," *Microporous and Mesoporous Materials*, vol. 107, no. 1–2, pp. 161–168, 2008.

- [36] T. Chen, J. Wang, C. Qing, S. Peng, Y. Song, and Y. Guo, "Effect of heat treatment on structure, morphology and surface properties of palygorskite," *Journal of the Chinese Ceramic Society*, vol. 34, no. 11, pp. 1406–1410, 2006.
- [37] B. Xu, W. M. Huang, Y. T. Pei et al., "Mechanical properties of attapulgite clay reinforced polyurethane shape-memory nanocomposites," *European Polymer Journal*, vol. 45, no. 7, pp. 1904–1911, 2009.
- [38] J. H. Huang, Y. F. Liu, Q. Z. Jin, and X. G. Wang, "Spectra study on the influence of drying process on palygorskite structure," *Spectroscopy and Spectral Analysis*, vol. 27, no. 2, pp. 408–410, 2007.
- [39] J. Madejová, "FTIR techniques in clay mineral studies," *Vibrational Spectroscopy*, vol. 31, no. 1, pp. 1–10, 2003.
- [40] R. L. Frost and Z. Ding, "Controlled rate thermal analysis and differential scanning calorimetry of sepiolites and palygorskites," *Thermochimica Acta*, vol. 397, no. 1-2, pp. 119–128, 2003.
- [41] D. M. Araújo Melo, J. A. C. Ruiz, M. A. F. Melo, E. V. Sobrinho, and A. E. Martinelli, "Preparation and characterization of lanthanum palygorskite clays as acid catalysts," *Journal of Alloys and Compounds*, vol. 344, no. 1-2, pp. 352–355, 2002.
- [42] D. M. A. Melo, J. A. C. Ruiz, M. A. F. Melo, E. V. Sobrinho, and M. Schmall, "Preparation and characterization of terbium palygorskite clay as acid catalyst," *Microporous and Mesoporous Materials*, vol. 38, no. 2-3, pp. 345–349, 2000.
- [43] M. M. Saatchi and A. Shojaei, "Effect of carbon-based nanoparticles on the cure characteristics and network structure of styrene-butadiene rubber vulcanizate," *Polymer International*, vol. 61, no. 4, pp. 664–672, 2012.
- [44] J. Vojislav, S. J. Suzana, B. S. Jaroslava, M. Gordana, and M. C. Milena, "Composites based on carbon black reinforced NBR/EPDM rubber blends," *Composites Part B*, vol. 45, no. 1, pp. 333–340, 2013.
- [45] H. Ismail, H. D. Rozman, R. M. Jaffri, and Z. A. Mohd Ishak, "Oil palm wood flour reinforced epoxidized natural rubber composites: the effect of filler content and size," *European Polymer Journal*, vol. 33, no. 10–12, pp. 1627–1632, 1997.
- [46] H. Ismail, H. Osman, and A. Ariffin, "A comparative study on curing characteristics, mechanical properties, swelling behavior, thermal stability, and morphology of feldspar and silica in SMR L vulcanizates," *Polymer*, vol. 43, no. 5, pp. 1323–1344, 2004.
- [47] H. Chen, M. Zheng, H. Sun, and Q. Jia, "Characterization and properties of sepiolite/polyurethane nanocomposites," *Materials Science and Engineering A*, vol. 445–446, pp. 725–730, 2007.
- [48] S. Prasertsri and N. Rattanasom, "Fumed and precipitated silica reinforced natural rubber composites prepared from latex system: mechanical and dynamic properties," *Polymer Testing*, vol. 31, no. 5, pp. 593–605, 2012.
- [49] K. Sahakaro and S. Beraheng, "Reinforcement of maleated natural rubber by precipitated silica," *Journal of Applied Polymer Science*, vol. 109, no. 6, pp. 3839–3848, 2008.
- [50] Z. X. Ooi, H. Ismail, and A. A. Bakar, "Synergistic effect of oil palm ash filled natural rubber compound at low filler loading," *Polymer Testing*, vol. 32, no. 1, pp. 38–44, 2013.
- [51] T. Pojanavaraphan, D. A. Schiraldi, and R. Magaraphan, "Mechanical, rheological, and swelling behavior of natural rubber/montmorillonite aerogels prepared by freeze-drying," *Applied Clay Science*, vol. 50, no. 2, pp. 271–279, 2010.
- [52] D. Fragiadakis, L. Bokobza, and P. Pissis, "Dynamics near the filler surface in natural rubber-silica nanocomposites," *Polymer*, vol. 52, no. 14, pp. 3175–3182, 2011.
- [53] J. P. Rath, T. K. Chaki, and D. Khastgir, "Development of natural rubber-fibrous nano clay attapulgite composites: the effect of chemical treatment of filler on mechanical and dynamic mechanical properties of composites," *Procedia Chemistry*, vol. 4, pp. 131–137, 2012.
- [54] N. Volle, F. Giulieri, A. Burr, S. Pagnotta, and A. M. Chaze, "Controlled interactions between silanol groups at the surface of sepiolite and an acrylate matrix: consequences on the thermal and mechanical properties," *Materials Chemistry and Physics*, vol. 134, no. 1, pp. 417–424, 2012.

Research Article

Ultrasonication Technique: A Method for Dispersing Nanoclay in Wood Adhesives

Alireza Kaboorani, Bernard Riedl, and Pierre Blanchet

Département des Sciences du Bois et de la Forêt, Faculté de Foresterie, de Géographie et de Géomatique, Université Laval, 2425 Rue de la Terrasse, QC, Canada G1V 0A6

Correspondence should be addressed to Bernard Riedl; bernard.riedl@sf.ulaval.ca

Received 7 May 2013; Revised 19 July 2013; Accepted 1 August 2013

Academic Editor: Gaurav Mago

Copyright © 2013 Alireza Kaboorani et al. This is an open access article distributed under the Creative Commons Attribution License, which permits unrestricted use, distribution, and reproduction in any medium, provided the original work is properly cited.

The efficiency of ultrasonication technique to disperse nanoclay in polyvinyl acetate (PVA) was examined. A hydrophilic nanoclay was added to PVA, and its effects on bond strength of wood joints were determined. The results of bond strength measured on block shear tests showed that nanoclay increased the bond strength of wood joints, especially in humid conditions. Atomic force microscopy (AFM) proved that it can be used to examine the quality of nanoclay dispersion in a matrix very precisely. The results of this study showed that ultrasonication technique is efficient in mixing nanoclay with the PVA matrix.

1. Introduction

Adhesives are among some of the most widely used components in structural materials due to the wide range of formulations that can be realized, providing a range of properties under conditions that other joining techniques cannot offer. Commercialization of wood adhesives in the mid 1950s generated a momentum for wood industries to diversify their products and enter into wider markets. Construction field was one of the markets which became more accessible to wood industries. Using adhesives allowed the manufacturers to fabricate wood composites with different sizes and shapes for the construction while maximizing resource utilization.

The price of wood adhesives covers an important part of production cost of wood products. As like any other industries, wood industries wish to bring down production costs in order to maximize profits. One of the means to cut the cost is to use low-cost adhesives in fabrication of the products. Low-cost adhesives usually have inferior properties. One of the examples of low-cost adhesives is polyvinyl acetate (PVA) which has been traditionally used for furniture assembly. As a wood adhesive, PVA has many advantages: nontoxic, with low negative impact on the environment, easy to use, and with low volatile organic compounds (VOCs) emissions. However,

PVA has low performance towards water ingress and high temperatures as well as low creep resistance. The vulnerability stems from the fact that PVA is a linear amorphous polymer with weak polar interaction among the molecular chains, which results in a relatively low glass-transition temperature (T_g), near 28°C.

Low-cost and simplicity of the application of PVA have convinced some wood products manufacturers to use PVA as an adhesive in the production of wood components for structures, despite the fact that PVA is not a heat-resistant adhesive. Using PVA as a structural adhesive puts the safety of home owners and fire fighters at risk as there is a higher probability of creep and sudden collapse of wood structures at high temperatures. In the past research, water resistance of PVA was mostly addressed, and little work has been done about heat resistance of PVA. Researchers have proposed some solutions to improve the properties of PVA. The solutions can be divided to two groups: (1) copolymerizing PVA with more hydrophobic or functional monomers [1–3] and (2) blending PVA with other adhesives or hardeners [4–11].

Introduction of nanotechnology has opened a new opportunity to develop new generation of adhesives with properties that cannot be gained by conventional methods. The

incorporation of nanoparticles into a polymer matrix can lead to a simultaneous improvement of different material properties [12, 13]. The development of nanoparticles-reinforced adhesive materials is presently one of the most explored areas in materials science and engineering. The exceptional properties of nanoparticles have led to widespread research in this area. Nanofillers provide many advantages over classical microreinforcements for adhesive materials; for example, they allow thin bond lines and consequently lower the risk of embrittlement within the bulk adhesive material, resulting in improved adhesive tensile strength [14].

Nanocomposites, with dispersed nanoparticles, have been studied extensively due to their capability to improve mechanical, physical, thermal, and barrier properties with very low nanoparticles loading of 1–5 wt% [15–17]. For such composites, montmorillonite (MMT) and other clay nanoparticles have been used by many researchers [18–25]. With a structure of stacked platelets and one dimension of the platelet in the nanometer scale, MMT has a high aspect ratio and specific surface when exfoliated. If the platelets are dispersed properly, its nanosize can provide a significant amount of interface between the clay and the matrix resin with only a small weight percentage of MMT, thus contributing to the excellent mechanical and physical properties of the nanocomposites.

Exfoliating the layered structure of the MMT within a given matrix is crucial to improving the properties of a polymer. Usually dispersing the layered structure of the MMT is a challenge. Nanocomposite formation involves the migration or diffusion of the polymer into the interlayer galleries of the layered silicate which push apart or swell the silicate layers. There are some techniques to disperse MMT into polymers. For thermosetting polymer, mechanical mixing is the most common of the techniques to disperse MMT to a matrix, while heating is excluded. Mechanical technique includes several methods such as mechanical mixing, shear mixing, and ultrasonic mixing.

Ultrasonic irradiation, as a new technology, has been widely used in chemical reactions. When ultrasonic waves pass through a liquid medium, a large number of microbubbles form, grow, and collapse in very short times, about a few microseconds. Ultrasonication generates alternating low-pressure and high-pressure waves in liquids, leading to the formation and violent collapse of small vacuum bubbles. This phenomenon is termed cavitation and causes high-speed impinging liquid jets and strong hydrodynamic shear-forces. These effects are used for the deagglomeration of nanometer-size materials. In this aspect, ultrasonication is an alternative to high-speed mixers and agitator bead mills. Ultrasonication has been used as a technique to disperse nanomaterials in different matrices [26–33].

In this study, ultrasonication was used to disperse the layered structures of MMT and develop MMT-reinforced PVA adhesives. Such reinforced adhesives can have improved properties. The main objective of this research is to study the feasibility of using ultrasonication as a technique to delaminate MMT layers and use delaminated, that is, exfoliated, MMT as nanoreinforcing filler for PVA. The bond strength of joints glued with newly formulated adhesives was examined

under different conditions. Also structures of MMT/PVA composites (film) were evaluated as well.

2. Experimental

2.1. Materials. A commercial polyvinyl acetate (PVA) was received in liquid form. Nanoclay which is low-cost and the most widely studied nanofiller was used as nanofiller in this study. A hydrophilic nanoclay, namely, Lit. G-105 (polymer-grade (PG) montmorillonite) was supplied by Nanocor, Inc., Arlington Heights, IL, USA. The specific gravity and cation-exchange capacity (CEC) of the nanoclay were 2.6 and 145 (meq/100 g), respectively. This commercial brand of nanoclay was chosen as nanoparticles because the past experience [34] has shown that dispersing this type of nanoclay by the high shear mixer in PVA is difficult and did not result in good dispersion. Black spruce (*Picea mariana*) obtained from trees grown in Québec province was used as a substrate for wood joints.

2.2. Preparation of Nanoclay/PVA Nanocomposites. Dispersion of nanoclay was conducted by a high-intensity ultrasonic horn (60 kHz, maximum amplitude 100 nm from tip to tip, Branson PG). One-gram nanoclay was added to 20 grams of water, and then the solution was ultrasonicated for 3–5 min. The temperature of the solution was kept below 50°C to ensure high temperatures due to ultrasonication does not interfere with the results. To maintain the temperature of the mixture below 50°C, the vessel with the mixture was cooled by means of recirculating ethylene glycol bath. Sonication experiments were carried out with 50% amplitude and a volume of 20 mL of the nanoparticle-water mixture. During ultrasonication, the sonication power was gradually raised while maintaining the temperature of the mixture below 50°C. A certain amount of the ultrasonicated solution was added to PVA, depending on the percentage of nanoclay in PVA. Percentage of nanoclay in PVA (ranging from 0% to 4%) was based on solid mass of PVA. The mixtures of PVA with nanoclay were mixed for 30 min. For X-ray diffraction (XRD), vapor sorption test, atomic force microscopy (AFM), and transmission electron microscopy (TEM), samples of nanocomposites were prepared by casting the PVA/nanoclay composites on Teflon sheets. Prior to further analyses, the sheets of nanocomposites were allowed to dry at room temperature for two weeks.

2.3. Fabrications and Tests of Wood Joints. Mixed solutions of PVA and nanoclay were used to bond wood samples. A wood species, black spruce, was used as substrate. Prior to gluing, the moisture content of wood was fixed at 12% by conditioning wood to 20°C and 60% relative humidity for two months. After applying glue on the surface of wood, the samples were pressed in an MTS hydraulic test machine with 50 kN capacity at 2.46 kg/cm² pressure for two hours. Before testing, glued samples were conditioned to 20°C and 60% relative humidity (RH) for two weeks. Twenty samples were tested for each set of formulation.

To evaluate the impact of nanoclay on performance of wood joints, the shear strength of wood joints was measured in dry and wet states, and at an elevated temperature. An MTS hydraulic test machine with 50 kN capacity was used for load application, and the data were acquired by a computer. Wood failure and maximum load were recorded for each test. Bond strength of adhesive in dry-state was studied on wood joints made of black spruce. The block shear tests were carried out according to ASTM D905-98. The sizes of samples for “wet-state” tests were the same as those for dry-state tests. For “wet-state” tests, the samples were taken directly out of the water after being immersed in water for 24 hours. Before the tests, excess water was wiped off from the samples. During the water immersion period, temperature of water was maintained at $23 \pm 1^\circ\text{C}$.

Block shear tests at the elevated temperature were carried out according to ASTM 7247-07. Samples made of black spruce were heated in an oven, having a temperature controller with an integral and derivative (PID) control algorithm, until the temperature in the middle of samples reached 100°C . On average, it took 30 min to reach 100°C in the middle of samples. After reaching 100°C in the middle of samples, the samples were kept at 100°C for 15 min more, followed by immediate block shear tests. The shear strength of samples was measured by an MTS hydraulic test machine.

2.4. Characterization of the Nanoclay/PVA Nanocomposites

2.4.1. Water-Vapor Sorption Analysis. One of main drawbacks of PVA as a wood adhesive is its vulnerability towards water and high humidity. PVA has low resistance towards water because of two reasons. First reason is the formation of hydrophilic hydroxyl and carboxyl groups during emulsion polymerization. PVA is usually partially hydrolyzed at the polymer branches to form hydrophilic hydroxyl and carboxyl groups appended to the polymer backbone. Second reason for the poor water resistance is the microscopic pores and water-soluble surfactant molecules which remain in the film allowing water-vapor to penetrate into the adhesive film easily [7]. Any decrease in water-vapor absorption of PVA by adding nanoclay results in more durable PVA adhesives. In order to find out the effect of adding nanoclay on response of nanoclay/PVA composites to humid environment, films of pure PVA and its composites were exposed to various humidity levels, and weight gain was monitored. The vapor sorption measurements were carried out at 25°C with a VTI-SA symmetrical vapor sorption analyzer, TA Instruments. The vapor sorption test was conducted in several steps. Between 7 and 10 mg of sample was placed in the chamber. First, the samples dried at 0% humidity and 25°C . As the sample weight equilibrated, the sample was exposed to 60%, 70%, 80%, 90%, and 95% RH, in a stepwise fashion, as the sample reached its maximum weight in each humidity level. Overall, the process took about 20 hrs.

2.4.2. X-Ray Diffraction (XRD). Small-angle X-ray scattering was used to examine efficiency of the ultrasonication technique to increase the distance between the nanoclay

platelets. XRD experiments were conducted by an X-ray diffractometer (Siemens/Bruker) (40 kV, 40 mA) using Cu ($\lambda = 1.5406 \text{ \AA}$) as the radiation source. The instrument consists of a Kristalloflex 760 generator, a 3-circle goniometer, and a Hi-Star area detector, and it was equipped with GADDs software. To measure the distance between nanoclay platelets before blending with PVA (powder form), the nanoclay powder was inserted in thin-walled (0.01 mm) glass capillary tubes (1.0 mm diameter). Increasing interlayer spacing is identified by a shift of the diffraction peak to lower angles, according to Bragg's law ($n\lambda = 2d \sin \theta$), leading eventually to featureless patterns (exfoliated structures).

2.4.3. Transmission Electron Microscopy (TEM). Transmission electron microscopy (TEM) allows a qualitative understanding of the internal structure, spatial distribution and dispersion of the nanoparticles within the polymer matrix, and views of the defect structure through direct visualization. Analyses were performed on a JEOL JEM-1230, transmission electron microscope at 80 kV. TEM specimens, having 50–70 nm thickness, were prepared by ultramicrotoming the nanocomposite samples encapsulated in an epoxy matrix.

2.4.4. Atomic Force Microscopy (AFM). Atomic force microscopy (AFM) observations were carried out using a NanoScope IIIa, an atomic force microscope (Veeco Instruments, Inc.). AFM measurements were done under ambient air conditions in tapping mode. The sensitivity of the tip deviation and the scanner resolution was 0.1 nm. The resolution was set to 512 lines by 512 pixels for all observations. Two topographic and phase images were obtained within each sample for scan areas of $10 \mu\text{m} \times 10 \mu\text{m}$ and $50 \mu\text{m} \times 50 \mu\text{m}$. Surface roughness was calculated in $50 \mu\text{m} \times 50 \mu\text{m}$ scan areas, using the classical mean surface roughness parameters R_a and R_q (RMS). The parameters were calculated by the NanoScope 5.30r3sr3 software as follows:

$$R_a = \frac{1}{n} \sum_{i=1}^n |Z_i - Z_{\text{ave}}|, \quad (1)$$

$$R_q = \text{RMS} = \sqrt{\frac{\sum (Z_i - Z_{\text{ave}})^2}{n}},$$

where R_a is the mean roughness, the arithmetic average of the absolute values of the surface height deviations, and R_q is the root mean square of the height, and in both equations Z_i is the current Z value, Z_{ave} is the average of the Z values within the given area, and n is the number of points within the given area.

2.5. Statistical Analyses. A one-way analysis of variance model was used to study the effect of nanoclay content on shear strength of wood joints. The general linear model (GLM) procedure of the SAS program was used, and pairwise comparisons were then made using the protected Fisher LSD (least significant difference).

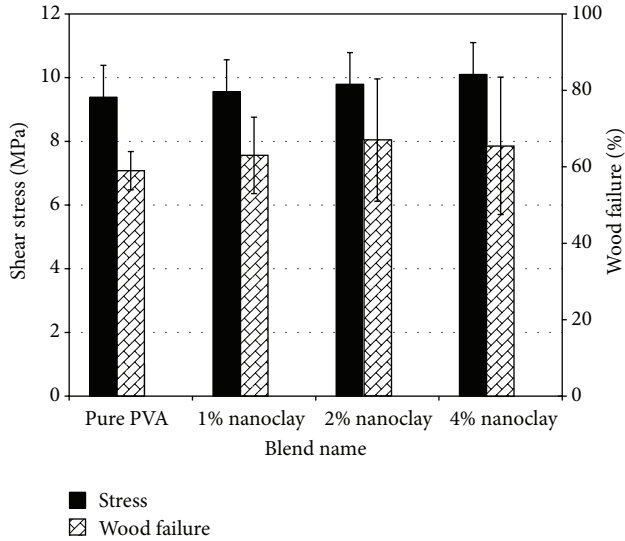


FIGURE 1: Bond strength for PVA and its nanocomposites in dry-state at room temperature. Twenty samples were tested for each data point.

TABLE 1: Tabular summary of wood joints tests at various conditions*.

Samples	Pure PVA	PVA and 1% nanoclay	PVA and 2% nanoclay	PVA and 4% nanoclay
Dry	9.38 (8%)	10.06 (5%)	10.77 (8%)	10.91 (8%)
Wet	2.82 (20%)	4.62 (12%)	5.22 (10%)	5.28 (10%)
The elevated temperature	1.33 (26%)	2.60 (14%)	2.76 (22%)	2.52 (19%)

*The values given in the brackets are coefficient variations (%).

3. Results

3.1. Bond Strength. Results of measuring shear strength of wood joints in dry tests are shown in Figure 1 and Table 1. Although fluctuations caused by varying loading of nanoclay on bond strength were not found significant, all joints with nanoclay in their formulations had improved shear strength. The increase in wood joints strength was between 2% and 7%. The strength of joints showed improvements as nanoclay content increased in the matrix. An increase in bond strength of wood joints could be measured not only in terms of shear strength but also in terms of wood failure under shear load. Inclusion of nanoclay to PVA increased wood failure of wood joints under shear load (Figure 1). Higher wood failure in joints having nanoclay in their adhesives means that nanoclay increased the strength of glue line to a level that the strength of glue line surpassed the strength of wood. It has been reported that nanoclay improves the mechanical properties of polymers by optimizing the number of available reinforcing elements for carrying an applied load and deflecting cracks. Also the coupling between the tremendous surface area of the clay and the polymer matrix facilitates stress transfer to

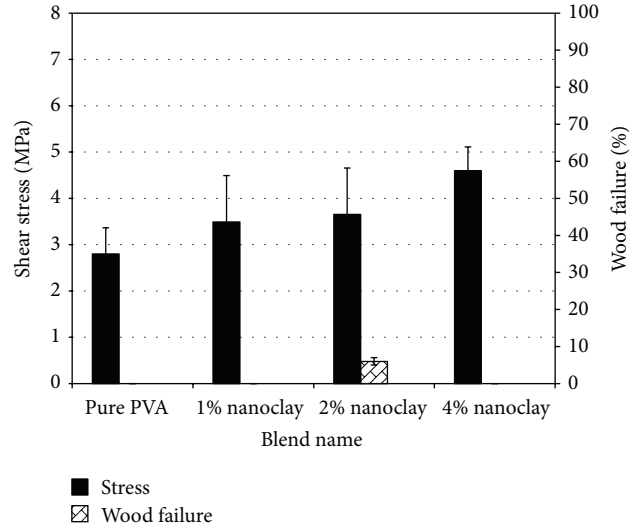


FIGURE 2: Shear strength of wood joints bonded by PVA and its nanocomposites after 24-hour water exposure. Twenty samples were tested for each data point.

the reinforcement phase, allowing for mechanical property improvements [35–39].

Figure 2 and Table 1 give the values of shear strength after 24-hour exposure of wood joints to water. Water exposure decreased the shear strength of wood joints. The shear strength of joints made of pure PVA decreased drastically, dropping down to one-sixth of dry-state. Adding nanoclay to PVA improved the resistance of glue line towards water. The extent of improvement was between 25% and 64%. Any increase in nanoclay loading in the matrix gave a boost to water resistance of wood joints (at all levels of loading). Positive effects of nanoclay on water resistance can be attributed to better barrier properties of glue line.

Past research shows that nanomaterials can improve the barrier properties of polymers [40–48]. The better barrier properties are associated to the fact that permeate molecules are forced to follow tortuous pathways, reducing the diffusion coefficients [39, 40]. In addition, the inclusion of nanoclay with layered structures and their adhesion to the polymer generate additional free volume, more likely affecting the polymeric chains located near interfacial regions [45–47]. Wood failure of joints was affected by adding nanoclay as well. Wood joints bonded with PVA and 2% nanoclay showed small percentage of wood failure under the shear load. The wood failure could be related to good dispersion of nanoclay in PVA matrix.

Values of shear strength of wood joints at 100°C are given in Figure 3 and Table 1. Nanoclay had a positive effect on heat resistance of wood joints. The effects were more pronounced at 1% loading (resulting in 96% increase in shear strength at 100°C). As nanoclay content in the PVA matrix increased, shear strength of wood joints improved at the elevated temperature. The extent of improvement was very significant at 4% nanoclay loading. The PVA with 4% nanoclay had 1.40 times higher shear strength. In our past

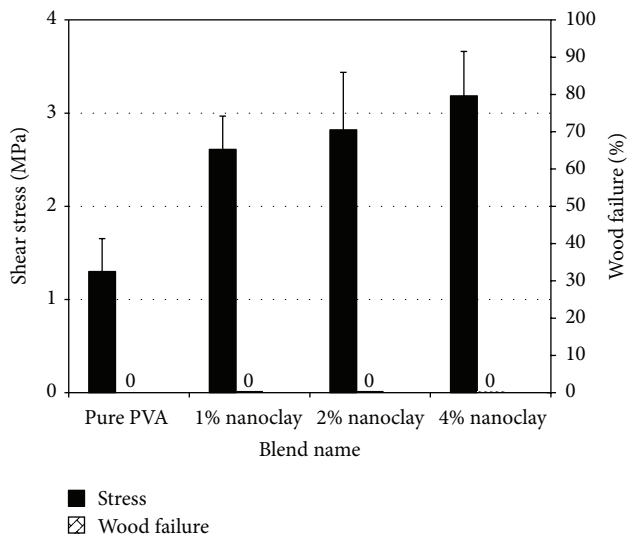


FIGURE 3: Shear strength of wood joints at the elevated temperature (100°C). Twenty samples were tested for each data point.

experience [34] with a high shear mixer, a decrease in shear strength of wood occurred at 4% nanoclay loading because of poor dispersion of nanoclay in the PVA matrix. Such a reduction did not occur in this study where an ultrasonic technique was used to disperse nanoclay particles in PVA. Thus, the results showed that using ultrasonic technique to disperse nanoclay particles in the matrix can enhance the effectiveness of nanoclay particles in the matrix.

Confinement of polymer chains in nanoclay galleries, restricting the mobility of polymer chains, and the ability of nanostructure materials to redistribute the deforming action over the volume of the materials have prominent impacts on improving the bond strength at high temperatures [49–51]. No wood failure was observed in the joints at the elevated temperature.

3.2. Water-Vapor Sorption. Results of vapor sorption tests are given in Figure 4. The negative values of vapor sorption at the beginning of the tests were related to the fact that the samples lost weight as they were conditioned at 0% RH in the first step of the tests. Such a conditioning continued until the mass loss of samples leveled off. The same procedure was applied to other RH levels. The final values of vapor sorption at 95% RH in which the samples reached saturation points were used to compare the samples performance in the vapor sorption tests. As nanoclay was introduced to the formulation, values of vapor sorption decreased. The extent of decrease in vapor sorption was proportional to nanoclay loading, as the lowest value of vapor sorption was observed at a formulation with 4% nanoclay. The results of vapor sorption tests can explain the water resistance of nanoclay/PVA composites when used a wood adhesive.

3.3. X-Ray Diffraction (XRD). Generally, the crystalline structure of nanoparticles has typically been established using X-ray diffraction (XRD) analysis and transmission

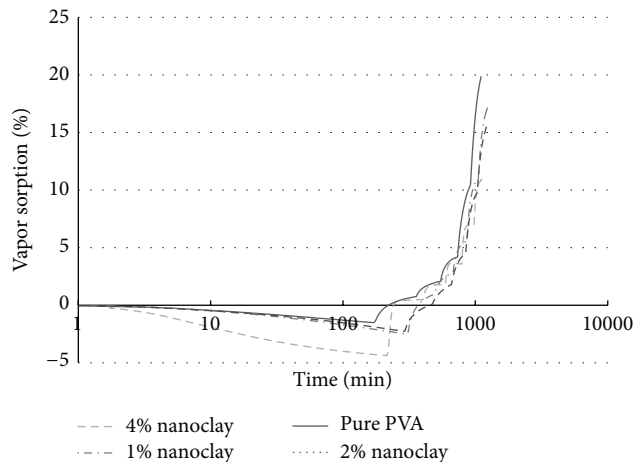


FIGURE 4: Vapor sorption of PVA/nanoclay composite film at different RH levels.

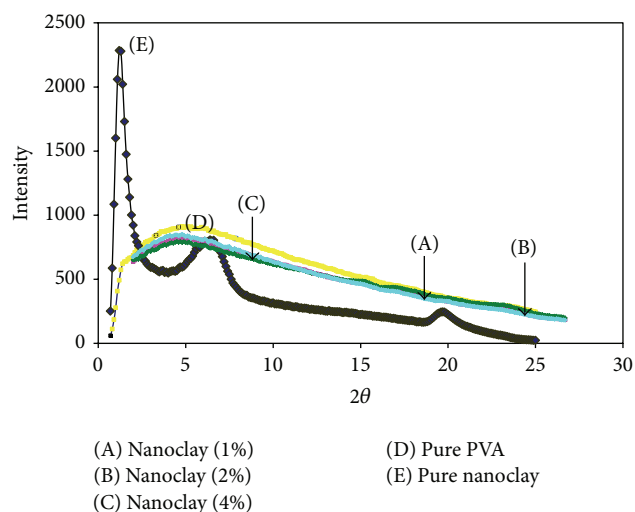


FIGURE 5: X-ray diffraction (XRD) patterns of pure PVA, pure nanoclay, and their nanocomposites.

electron microscopy (TEM). Due to its relative easiness and availability, XRD is most commonly used to probe the nanocomposite structure and occasionally to study the kinetics of the polymer melt intercalation. XRD is used to probe alterations in the order of silicates by monitoring the position, shape, and intensity of their basal reflections. For an intercalated structure, the (0 0 1) characteristic peak tends to shift to lower-angle regime due to the expansion of the basal spacing. Although the layer spacing increases, there still exists an attractive force between the silicate layers to stack them in an ordered structure. In contrast, no peaks are observed in the XRD pattern of exfoliated polymer nanocomposites due to loss of the structural registry of the layers.

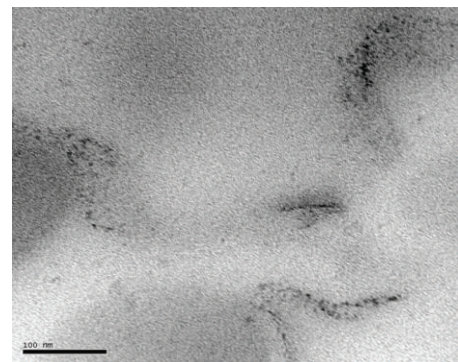
Figure 5 presents the X-ray diffraction profiles of pure PVA, pure nanoclay, and their nanocomposites prepared at different nanoclay loadings. Bragg's equation was used to calculate basal spacings of nanoclay from the XRD peak position. Nanoclay in pure forms had two peaks at 1.2° and

6.7°. The intensity of peak at 1.2° is higher than the other. According to Bragg's equation, the distances between clay platelets were 7.36 nm and 1.32 nm. After mixing nanoclay with PVA at different loadings, both peaks disappeared. In fact, X-ray diffraction profiles of PVA nanocomposites with different amounts of nanoclay are like those of pure PVA. According to the definition of exfoliated structure, exfoliation is achieved when the individual montmorillonite platelets no longer exhibit an XRD deflection; it can be concluded that an exfoliated structure was achieved in all studied cases. It should be noted that it is very hard to draw any conclusion on structures of nanocomposites solely according to the results of XRD as some layered silicates initially do not exhibit well-defined basal reflections. Thus, peak broadening and intensity decreases are very difficult to study systematically. Therefore, conclusions concerning the mechanism of nanocomposites formation and their structure based solely on XRD patterns are only tentative. On the other hand, TEM allows a qualitative understanding of the internal structure, spatial distribution and dispersion of the nanoparticles within the polymer matrix, and views of the defect structure through direct visualization.

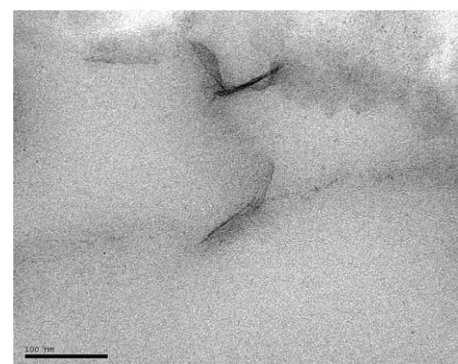
3.4. Transmission Electron Microscopy (TEM). Figure 6 shows the TEM images for nanocomposites containing nanoclay. Adding nanoclay at 1% and 2% loadings led to good dispersion of nanoclay in matrix. The distance between nanoclay platelets was increased, and the polymer chains entered between the platelets space. This nanostructure is referred to as exfoliated structure, giving superior properties to nanocomposites. As can be seen in Figure 6(c), nanocomposite with 4% is composed mostly of intercalated structure with very large aggregates or tactoids in the order of several tens of silicate layers. Intercalated structure is not considered an ideal structure for a nanocomposite, and it does not grant the nanocomposites with superior properties as exfoliated structure does. As observed in measuring bond strength (in dry condition and at the elevated temperature), adding nanoclay at 1% and 2% loadings gave a significant boost to the properties, but improvement of the properties at 4% content was not much different than with nanocomposites with 1% and 2% nanoclays. This phenomenon should be related to difficulty of dispersing nanoclay in matrix at high loadings.

Past research has shown that there is a direct linkage between properties of nanocomposites and quality of nanoclay dispersion [52–57]. In fact, the extent of improvement, as result of adding nanoclay, cannot be solely proportional to nanoclay loading because of difficulty in obtaining good dispersion at high loading.

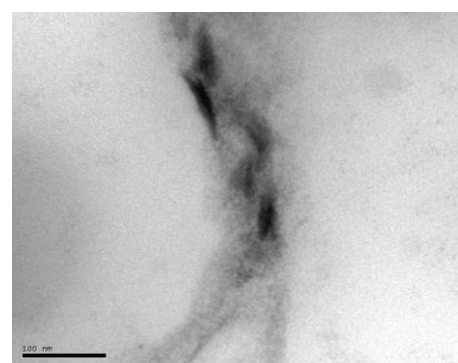
3.5. Atomic Force Microscopy (AFM). Although XRD and TEM are used to study the quality of nanoclay dispersion in the polymer, problems involving XRD measurements (for example, some layered silicates initially do not exhibit well-defined basal reflections) and subjectivity of TEM observations raise some questions regarding the results obtained by XRD and TEM. In order to draw a firm conclusion on structure of nanocomposites, a quantitative technique should



(a)



(b)



(c)

FIGURE 6: Images of PVA/nanoclay composites with different nanoclay loadings ((a) 1%, (b) 2%, and (c) 4%). Scale bar is 100 nm.

be used. In this study, atomic force microscopy (AFM) was used to determine the effects of adding nanoclay on PVA surface structure. The AFM images for pure PVA and its composites are presented in Figure 7. Pure PVA had a smooth surface as it had low roughness values. As nanoclay was added to the matrix, a reorganized surface was observed. The reorganization became more notable as nanoclay loading in the matrix increased. At 4% nanoclay loading, the surface of PVA film totally reorganized as a big increase in roughness values was detected although this roughness is still too small to be detected by human eye or resulted in light diffusion.

The results of this study show that the ultrasonication technique is an effective way to disperse nanoclay in the

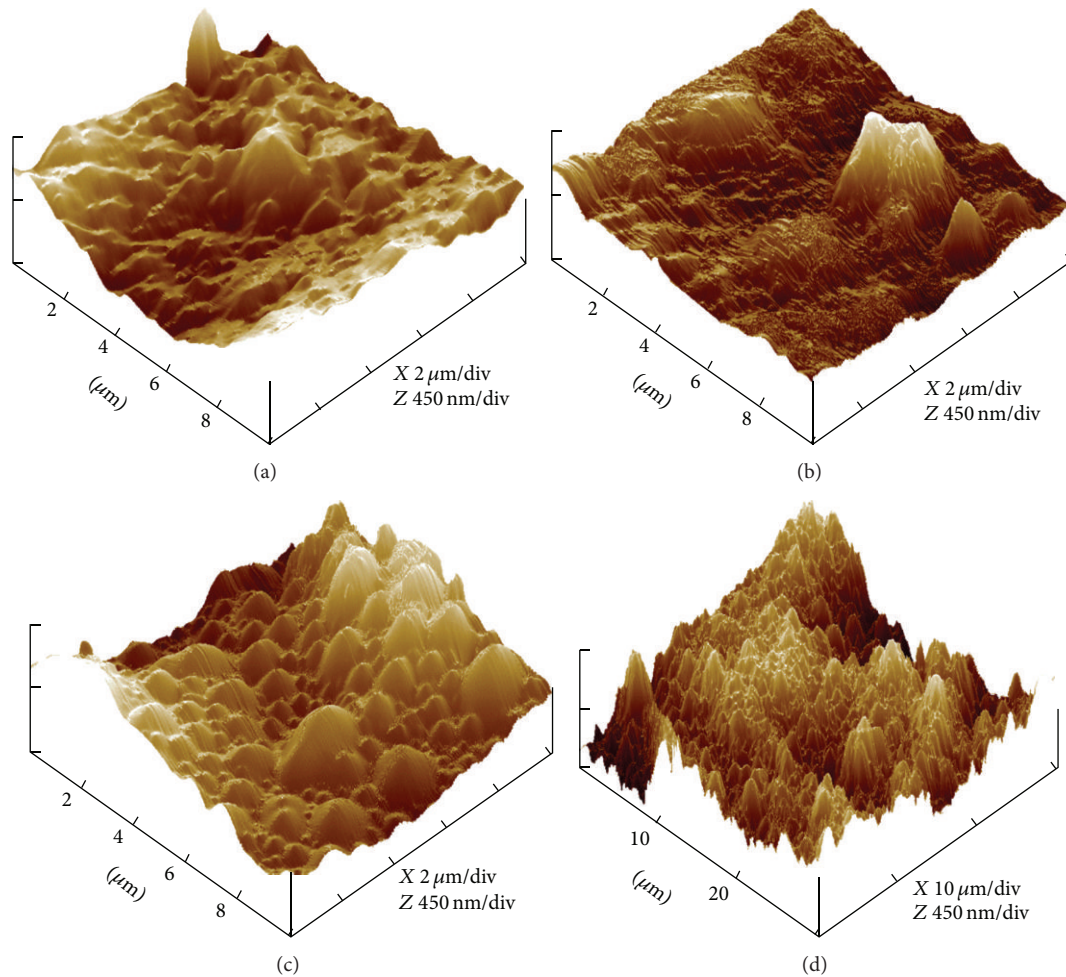


FIGURE 7: AFM images of pure PVA and its composites with different nanoclay loadings: (a) pure PVA, (b) 1% nanoclay, (c) 2% nanoclay, and (d) 4% nanoclay.

PVA matrix. The extent of improvement on PVA performance as a wood adhesive was superior or at least similar to that obtained by high-speed mixing [34]. When a high-speed mixer was used to disperse nanoclay at a high loading (4%) in the matrix, a remarkable reduction was observed in the improvement gained by adding nanoclay. Such a reduction was not observed in the case of ultrasonic technique. Although adding 4% nanoclay to the PVA matrix resulted in an intercalated structure, nanoclay did increase the shear strength of wood joints in humid conditions and at the elevated temperature. The results show that ultrasonic technique is very efficient in dispersing nanoclay especially at high loadings, contrary to the high shear speed mixer. High-speed mixing could disperse nanoclay in the PVA only at low loadings and increased bond strength of PVA in different conditions. High-speed mixing has some disadvantages: possible damage to PVA emulsion (because of strong shear force used during the mixing), high cost, and high energy consumption. By contrast, ultrasonication technique has minimum negative impact on PVA emulsion. Moreover, ultrasonication technique is economical as ultrasonic mixing could take place before production of PVA and the solution containing

nanoclay can be added to PVA during the production process. By considering the results obtained from this paper and our previous work [34] and by considering the advantages of ultrasonication technique over high-speed mixing, adding nanoclay to PVA in an industrial scale seems feasible and can be recommended to wood adhesive manufacturers.

4. Conclusions

The results of this study showed that ultrasonication technique is efficient in dispersing nanoclay in PVA at low (1% and 2%) and high (4%) loadings. Bond strength of newly formulated adhesives measured on block shear samples increased in wet conditions and at the elevated temperature. In dry-state, the positive effects of nanoclay on strength of glue line could be observed in terms of wood failure percentage. The strength of glue line was so high that some failure occurred in wood rather than in glue line. Improved barrier properties strengthened the resistance of glue line towards water, and subsequently significant increase was observed in bond strength in the wet-state. Contrary to the results obtained from dry condition, the extent of improvement

on bond strength in wet-state was proportional to nanoclay loading. Bond strength of PVA at the elevated temperature was also affected by adding nanoclay. As nanoclay loading in the PVA matrix increased, the shear strength of wood joints at the elevated temperature improved, despite the fact that the biggest gain in the shear strength was observed at 1% nanoclay loading. Vapor sorption tests displayed that nanoclay reduced vapor sorption of the matrix, explaining higher water resistance of glue line having nanoclay in their formulations. The morphological studies of nanocomposites revealed that the fluctuations observed in bond strength tests were related to dispersion quality of nanoclay in the matrix (PVA). AFM proved that it is a credible technique to examine the quality of dispersion as the results of AFM fully conformed to the TEM observations. At low loadings (1% and 2%), an exfoliated structure is achieved, causing a significant improvement on PVA properties. At high loading (4%), a coexistence of exfoliation and intercalation was observed, and so improvements on the shear strength of wood joints were achieved to a lesser extent.

Acknowledgments

The authors acknowledge the financial support from Natural Sciences and Engineering Research Council of Canada. Thanks are also extended to FPInnovations for their assistance.

References

- [1] H. Zhou, "Research on the improvement of water resistance of polyvinyl acetate emulsion," *Nianjie*, vol. 12, no. 4, pp. 11–12, 1991.
- [2] Y. Cai, "Synthesis of melamine-formaldehyde resin modified poly (VAc-MMA) emulsion," *China Adhesives*, vol. 6, no. 2, pp. 43–45, 1997.
- [3] Y. Chen, "Researches of wood adhesives with high strength, water and creep resistance," *Nianjie*, vol. 17, no. 1, pp. 25–27, 1996.
- [4] G. Lu, "Improvement of polyvinyl acetate emulsions," *Huagong Shikan*, vol. 10, no. 6, p. 17, 1996.
- [5] J. Comyn, *Adhesion Science*, The Royal Society of Chemistry, London, UK, 1997.
- [6] J. Wang, "Study on improving properties of polyvinyl acetate emulsion," *Zhanjie*, vol. 20, no. 3, pp. 16–19, 1999.
- [7] L. Qiao, A. J. Easteal, C. J. Bolt, P. K. Coveny, and R. A. Franich, "Improvement of the water resistance of poly(vinyl acetate) emulsion wood adhesive," *Pigment and Resin Technology*, vol. 29, no. 3, pp. 152–158, 2000.
- [8] M. Huang, S. Kuo, H. Wu, F. Chang, and S. Fang, "Miscibility and hydrogen bonding in blends of poly(vinyl acetate) with phenolic resin," *Polymer*, vol. 43, no. 8, pp. 2479–2487, 2002.
- [9] F. López-Suevos and C. E. Frazier, "Fracture cleavage analysis of PVAc latex adhesives: influence of phenolic additives," *Holz-forschung*, vol. 60, no. 3, pp. 313–317, 2006.
- [10] S. Kim and H. Kim, "Thermal stability and viscoelastic properties of MF/PVAc hybrid resins on the adhesion for engineered flooring in under heating system; ONDOL," *Thermochimica Acta*, vol. 444, no. 2, pp. 134–140, 2006.
- [11] S. Kim and H. Kim, "Effect of addition of polyvinyl acetate to melamine-formaldehyde resin on the adhesion and formaldehyde emission in engineered flooring," *International Journal of Adhesion and Adhesives*, vol. 25, no. 5, pp. 456–461, 2005.
- [12] B. Wetzel, F. Hauptert, and M. Q. Zhang, "Epoxy nanocomposites with high mechanical and tribological performance," *Composites Science and Technology*, vol. 63, no. 14, pp. 2055–2067, 2003.
- [13] J. Cho, M. S. Joshi, and C. T. Sun, "Effect of inclusion size on mechanical properties of polymeric composites with micro and nano particles," *Composites Science and Technology*, vol. 66, no. 13, pp. 1941–1952, 2006.
- [14] O. Jacobs, W. Xu, B. Schädel, and W. Wu, "Wear behaviour of carbon nanotube reinforced epoxy resin composites," *Tribology Letters*, vol. 23, no. 1, pp. 65–75, 2006.
- [15] X. L. Ji, J. E. Hampsey, Q. Y. Hu, J. B. He, Z. Z. Yang, and Y. F. Lu, "Mesoporous silica-reinforced polymer nanocomposites," *Chemistry of Materials*, vol. 15, no. 19, pp. 3656–3662, 2003.
- [16] Q. Zhang and L. A. Archer, "Optical polarimetry and mechanical rheometry of poly(ethylene oxide)—silica dispersions," *Macromolecules*, vol. 37, no. 5, pp. 1928–1936, 2004.
- [17] B. J. Ash, R. W. Siegel, and L. S. Schadler, "Mechanical behavior of alumina/poly(methyl methacrylate) nanocomposites," *Macromolecules*, vol. 37, no. 4, pp. 1358–1369, 2004.
- [18] A. Pegoretti, J. Kolarik, C. Peroni, and C. Migliaresi, "Recycled poly(ethylene terephthalate)/layered silicate nanocomposites: morphology and tensile mechanical properties," *Polymer*, vol. 45, no. 8, pp. 2751–2759, 2004.
- [19] K. M. Lee and C. D. Han, "Linear dynamic viscoelastic properties of functionalized block copolymer/organoclay nanocomposites," *Macromolecules*, vol. 36, no. 3, pp. 804–815, 2003.
- [20] J. H. Chang, B. S. Seo, and D. H. Hwang, "An exfoliation of organoclay in thermotropic liquid crystalline polyester nanocomposites," *Polymer*, vol. 43, no. 10, pp. 2969–2974, 2002.
- [21] J. Ma, P. Xiang, Y. W. Mai, and L. Q. Zhang, "A novel approach to high performance elastomer by using clay," *Macromolecular Rapid Communications*, vol. 25, no. 19, pp. 1692–1696, 2004.
- [22] T. D. Fornes and D. R. Paul, "Structure and properties of nanocomposites based on nylon-11 and -12 compared with those based on nylon-6," *Macromolecules*, vol. 37, no. 20, pp. 7698–7709, 2004.
- [23] F. Bensadoun, N. Kchit, C. Billotte, F. Trochu, and E. Ruiz, "A comparative study of dispersion techniques for nanocomposite made with nanoclays and an unsaturated polyester resin," *Journal of Nanomaterials*, vol. 2011, Article ID 406087, 12 pages, 2011.
- [24] J. W. Gilman, T. Kashiwagi, and J. D. Lichtenhan, "Nanocomposites: a revolutionary new flame retardant approach," *SAMPE Journal*, vol. 33, no. 4, pp. 40–46, 1997.
- [25] B. M. Le, C. Wilkie, S. Bourbigot, and S. Duquesne, *Fire Retardancy of Polymers: The Use of Micro- and Nano-Sized Mineral Fillers*, R.S.C., Cambridge, UK, 2004.
- [26] S. D. Burnside and E. P. Giannelis, "Synthesis and properties of new poly(dimethylsiloxane) nanocomposites," *Chemistry of Materials*, vol. 7, no. 9, pp. 1597–1600, 1995.
- [27] S. S. Park, N. Bernet, S. de la Roche, and H. T. Hahn, "Processing of iron oxide-epoxy vinyl ester nanocomposites," *Journal of Composite Materials*, vol. 37, no. 5, pp. 465–476, 2003.
- [28] R. D. West and V. M. Malhotra, "Rupture of nanoparticle agglomerates and formulation of Al₂O₃-epoxy nanocomposites using ultrasonic cavitation approach: effects on the structural

- and mechanical properties," *Polymer Engineering and Science*, vol. 46, no. 4, pp. 426–430, 2006.
- [29] H. Mahfuz, M. F. Uddin, V. K. Rangari, M. C. Saha, S. Zainuddin, and S. Jeelani, "High strain rate response of sandwich composites with nanophased cores," *Applied Composite Materials*, vol. 12, no. 3–4, pp. 193–211, 2005.
- [30] H. Xia and Q. Wang, "Preparation of conductive polyaniline/nanosilica particle composites through ultrasonic irradiation," *Journal of Applied Polymer Science*, vol. 87, no. 11, pp. 1811–1817, 2003.
- [31] A. Yasmin, J. J. Luo, and I. M. Daniel, "Processing of expanded graphite reinforced polymer nanocomposites," *Composites Science and Technology*, vol. 66, no. 9, pp. 1182–1189, 2006.
- [32] B. Bittmann, F. Hauptert, and A. K. Schlarb, "Ultrasonic dispersion of inorganic nanoparticles in epoxy resin," *Ultrasonics Sonochemistry*, vol. 16, no. 5, pp. 622–628, 2009.
- [33] B. Bittmann, *Ultraschalldispargierung von Anorganischen Nanopartikeln in Epoxidharz und Charakterisierung der Resultierenden Werkstoffe [Ph.D. thesis]*, Institut für Verbundwerkstoffe, Kaiserslautern, Germany, 2009.
- [34] A. Kaboorani and B. Riedl, "Effects of adding nano-clay on performance of polyvinyl acetate (PVA) as a wood adhesive," *Composites A*, vol. 42, no. 8, pp. 1031–1039, 2011.
- [35] E. P. Giannelis, "Polymer layered silicate nanocomposites," *Advanced Materials*, vol. 8, no. 1, pp. 29–35, 1996.
- [36] M. Alexandre and P. Dubois, "Polymer-layered silicate nanocomposites: preparation, properties and uses of a new class of materials," *Materials Science and Engineering R*, vol. 28, no. 1, pp. 1–63, 2000.
- [37] T. J. Pinnavaia and G. W. Beall, *Polymer-Clay Nanocomposites*, John Wiley & Sons, New York, NY, USA, 2001.
- [38] S. S. Ray and M. Okamoto, "Polymer/layered silicate nanocomposites: a review from preparation to processing," *Progress in Polymer Science*, vol. 28, no. 11, pp. 1539–1641, 2003.
- [39] H. Fischer, "Polymer nanocomposites: from fundamental research to specific applications," *Materials Science and Engineering C*, vol. 23, no. 6–8, pp. 763–772, 2003.
- [40] L. Nielsen, "Models for the permeability of filled polymer systems," *Journal of Macromolecular Science A*, vol. 1, no. 5, pp. 929–942, 1967.
- [41] R. K. Bharadwaj, "Modeling the barrier properties of polymer-layered silicate nanocomposites," *Macromolecules*, vol. 34, no. 26, pp. 9189–9192, 2001.
- [42] W. R. Falla, M. Mulski, and E. L. Cussler, "Estimating diffusion through flake-filled membranes," *Journal of Membrane Science*, vol. 119, no. 1, pp. 129–138, 1996.
- [43] N. A. Plate and Y. P. Yampol'skii, "Relationship between structure and transport properties for high free volume polymeric materials," in *Polymeric Gas Separation Membranes*, D. R. Paul and Y. P. Yampol'skii, Eds., chapter 5, pp. 155–207, CRC Press, Boca Raton, Fla, USA, 1994.
- [44] A. Thran, G. Kroll, and F. Faupel, "Correlation between fractional free volume and diffusivity of gas molecules in glassy polymers," *Journal of Polymer Science B*, vol. 37, no. 23, pp. 3344–3358, 1999.
- [45] R. A. Pethrick, "Positron annihilation—a probe for nanoscale voids and free volume?" *Progress in Polymer Science*, vol. 22, no. 1, pp. 1–47, 1997.
- [46] Y. Q. Wang, Y. P. Wu, H. F. Zhang, L. Q. Zhang, B. Wang, and Z. F. Wang, "Free volume of montmorillonite/styrene-butadiene rubber nanocomposites estimated by positron annihilation lifetime spectroscopy," *Macromolecular Rapid Communications*, vol. 25, no. 23, pp. 1973–1978, 2004.
- [47] O. Becker, Y. B. Cheng, R. J. Varley, and G. P. Simon, "Layered silicate nanocomposites based on various high-functionality epoxy resins: the influence of cure temperature on morphology, mechanical properties, and free volume," *Macromolecules*, vol. 36, no. 5, pp. 1616–1625, 2003.
- [48] P. Winberg, M. Eldrup, N. J. Pedersen, M. A. van Es, and F. H. J. Maurer, "Free volume sizes in intercalated polyamide 6/clay nanocomposites," *Polymer*, vol. 46, no. 19, pp. 8239–8249, 2005.
- [49] A. Laachachi, E. Leroy, M. Cochez, M. Ferriol, and J. M. L. Cuesta, "Use of oxide nanoparticles and organoclays to improve thermal stability and fire retardancy of poly(methyl methacrylate)," *Polymer Degradation and Stability*, vol. 89, no. 2, pp. 344–352, 2005.
- [50] F. Yang and G. L. Nelson, "Polymer/silica nanocomposites prepared via extrusion," *Polymers for Advanced Technologies*, vol. 17, no. 4, pp. 320–326, 2006.
- [51] B. N. Dudkin, G. G. Zainullin, P. V. Krivoschapkin, E. F. Krivoschapkina, and M. A. Ryazanov, "Influence of nanoparticles and nanofibers of aluminum oxide on the properties of epoxy composites," *Glass Physics and Chemistry*, vol. 34, no. 2, pp. 187–191, 2008.
- [52] T. G. Macia-Agullo, J. C. Fernandez-Garcia, A. Torro-Palau, A. C. Orgiles-Barcelo, and J. M. Martin-Martinez, "Addition of silica to polyurethane adhesives," *Journal of Adhesives*, vol. 38, no. 1–2, pp. 31–53, 1992.
- [53] T. V. González, C. G. Salazar, J. R. de la Rosa, and V. González, "Nylon 6/organoclay nanocomposites by extrusion," *Journal of Applied Polymer Science*, vol. 108, no. 5, pp. 2923–2933, 2008.
- [54] M. Mirzataheri, M. Atai, and A. R. Mahdavian, "Physical and mechanical properties of nanocomposite barrier film containing encapsulated nanoclay," *Journal of Applied Polymer Science*, vol. 118, no. 6, pp. 3284–3291, 2010.
- [55] C. Zilg, R. Mülhaupt, and J. Finter, "Morphology and toughness/stiffness balance of nanocomposites based upon anhydride-cured epoxy resins and layered silicates," *Macromolecular Chemistry and Physics*, vol. 200, no. 3, pp. 661–670, 1999.
- [56] A. Ranade, N. A. D'Souza, and B. Gnade, "Exfoliated and intercalated polyamide-imide nanocomposites with montmorillonite," *Polymer*, vol. 43, no. 13, pp. 3759–3766, 2002.
- [57] X. Fu and S. Qutubuddin, "Polymer-clay nanocomposites: exfoliation of organophilic montmorillonite nanolayers in polystyrene," *Polymer*, vol. 42, no. 2, pp. 807–813, 2001.

Research Article

Polyethylene/Clay Nanocomposites Produced by *In Situ* Polymerization with Zirconocene/MAO Catalyst

Pimpatima Panupakorn,¹ Ekrachan Chaichana,²
Piyasan Prasertdam,¹ and Bunjerd Jongsomjit¹

¹ Center of Excellence on Catalysis and Catalytic Reaction Engineering, Department of Chemical Engineering, Faculty of Engineering, Chulalongkorn University, Bangkok 10330, Thailand

² Chemistry Program, Faculty of Science and Technology, Nakhon Pathom Rajabhat University, Nakhon Pathom 73000, Thailand

Correspondence should be addressed to Bunjerd Jongsomjit; bunjerd.j@chula.ac.th

Received 14 June 2013; Revised 25 July 2013; Accepted 25 July 2013

Academic Editor: Shanfeng Wang

Copyright © 2013 Pimpatima Panupakorn et al. This is an open access article distributed under the Creative Commons Attribution License, which permits unrestricted use, distribution, and reproduction in any medium, provided the original work is properly cited.

Two commercial nanoclays were used here as catalytic fillers for production of polyethylene (PE) and linear low-density polyethylene (LLDPE) nanocomposites via *in situ* polymerization with zirconocene/MAO catalyst. It was found that both types of nanoclays designated as clay A and clay B can improve thermal stability to the host polymers as observed from a thermal gravimetric analysis (TGA). The distribution of the clays inside the polymer matrices appeared good due to the *in situ* polymerization system into which the clays were introduced during the polymer forming reaction. Upon investigating the clays by X-ray diffractometer (XRD) and Fourier transform infrared spectroscopy (FTIR), it was observed that the crucial differences between the two clays are the crystallite sizes ($A < B$) and the amounts of amine group ($A < B$). The higher amount of amine group in clay B was supposed to be a major reason for the lower catalytic activity of the polymerization systems compared to clay A resulting from its deactivating effect on zirconocene catalyst. However, for both clays, increasing their contents in the polymerization systems reduced the catalytic activity due to the higher steric hindrance occurring.

1. Introduction

During the growth of polyolefin production, polyethylene (PE) is considered as one of the most widely used synthetic polymer with the annual production approximately 80 million metric tons [1]. This is due to its unique properties such as light weight, high chemical resistance, and low dielectric constant. However, the polyethylene properties have some restrictions on its use. It does not have enough stiffness, has low gas permeability, and can easily catch fire. Therefore, improving the polyethylene properties is important. Addition of additives or fillers can improve polyethylene properties such as mechanical property, thermal property, barrier property, and flame resistant. Due to the advantage of nanotechnology nowadays, nanoscale materials have been used as fillers instead of conventional microscale materials and also provide better properties. The polymers with the addition of nanofiller can be designated as polymer nanocomposites. The final properties of polymer nanocomposites depend strongly

on the properties of the filler. Different types of nanofillers have been used in the production of polymer nanocomposites including organic nanofiller such as cellulose and inorganic nanofiller such as carbon nanotube (CNT) [2, 3], silica (SiO_2) [4], alumina (Al_2O_3) [5], and clay [6, 7]. Using nanoclay as a filler is of interest for nanocomposite production due to ready availability and low cost. Zhao et al. [6] studied the properties of PE/clay nanocomposites, which were prepared by melt mixing and found that the mechanical and flammability properties of the polymers improved with the clay addition. Huang et al. [7] studied the thermal stability and fire behavior of LDPE/clay nanocomposites, which were prepared by melt mixing, and observed the improved thermal stability and flame retardant. Besides the nature of fillers and their content in the product, the adhesion between matrix and filler and the aspect ratio of the filler are also the key factors in the improvement of the polymer final properties [8]. The platelet nanoclay is one of the high aspect ratio fillers, therefore receiving considerable attention. For enhancing the adhesion between

two phases, modification of nanoclay with appropriate agent is usually used for this purpose. Hakim et al. [9] investigated clay nanoplatelets treated (modified) with ammonia and dodecylamine at different conditions in the *in situ* ethylene polymerization system with metallocene catalyst (Cp_2ZrCl_2). It was found that the treated clays provided the higher catalytic activity than the untreated clays. However, the modifiers sometimes deteriorate the polymerization systems particularly for the *in situ* polymerization systems into which the modified fillers were introduced during the polymer growing process [10].

In this study, the two commercial nanoclays completely modified with different amounts of amine group were investigated to compare their roles in the *in situ* polymerization with MAO/metallocene catalysts for the production of PE/clay composite and LLDPE/clay composite. The nature of both clays was characterized using Fourier transform infrared spectroscopy (FTIR) and X-ray diffraction analysis (XRD). The effect of clay natures and loadings on the nanocomposite properties and the catalytic activity of polymerization systems were studied by nuclear magnetic resonance (^{13}C NMR), scanning electron microscopy (SEM), and so forth.

2. Experimental

2.1. Materials. All chemicals and polymerization were performed under an argon atmosphere using a glove box and/or Schlenk techniques. Nanoclays (montmorillonite, MMT containing different amounts of amine group) were donated by Thai Nippon Chemical Industry Co., Ltd., Thailand. Toluene was dried over dehydrated CaCl_2 and distilled over sodium/benzophenone before use. The *rac*-ethylenebis(indenyl) zirconium dichloride (*rac*-Et[Ind] $_2$ ZrCl $_2$) was obtained from Aldrich Chemical Company, Inc. Methylaluminoxane (MAO) in hexane was donated by Tosoh (Akzo, Japan). Ultrahigh purity argon was purchased from Thai Industrial Gas Co., Ltd. And was further purified by passing it through columns that were packed with BASF catalyst R3-11G (molecular-sieved to 3 Å), sodium hydroxide (NaOH), and phosphorus pentoxide (P_2O_5) to remove traces of oxygen and moisture. Ethylene gas (99.96%) was donated by the National Petrochemical Co., Ltd., Thailand. 1-Hexene (99%, $d = 0.673$ g/mL) and hydrochloric acid (HCl, fuming 36.7%) were purchased from Aldrich Chemical Company, Inc. Methanol (commercial grade) was purchased from SR Lab Co., Ltd.

2.2. Treatment of Nanoclay. The nanoclay (clay A or clay B) was heated at 150°C for 2 h and then heated at 150°C for 2 h under argon atmosphere.

2.3. Preparation of Catalyst. In the glove box, *rac*-Et(Ind) $_2$ ZrCl $_2$ 0.0083 g (1.98×10^{-5} moles) was added in 20 mL of toluene solution and stirred at room temperature at least 30 min or until giving yellow transparent solution.

2.4. In Situ Polymerization. *In situ* polymerization was conducted under argon atmosphere using Schlenk techniques

and/or glove box. It was carried out in a 100 mL semibatch stainless steel autoclave reactor equipped with a magnetic stirrer. The desired amount of nanoclay (5, 10, 20, and 40 wt%) as support and methylaluminoxane (MAO) 1.1 mL ($[\text{Al}]_{\text{MAO}}/[\text{Zr}] = 1135$) were mixed and stirred for 30 min aging at room temperature. Then, catalyst solution 1.5 mL [$\text{Et}(\text{Ind})_2\text{ZrCl}_2$ 5×10^{-5} M] along with toluene (to make total volume of 30 mL) was put into the reactor. Then, ethylene was fed into the reactor equipped with pressure gauge. After all ethylene was consumed (6 psi from pressure gauge), the reaction was terminated by addition of acidic methanol and stirred overnight. After filtration and dried at room temperature, polyethylene/clay nanocomposite is obtained. For copolymerization, 1-hexene as comonomer (1:0.5 of ethylene:1-hexene ratio) was also put into the reactor.

2.5. Characterization

2.5.1. Characterization of Nanoclay

X-Ray Diffraction Analysis (XRD). The crystallite structure of nanoclay was investigated by X-ray diffractometer SIEMENS D-5000 with Cu K_α ($\lambda = 1.54439$ Å). The range of detection $2\theta = 10$ – 80° .

Thermal Gravimetric Analysis (TGA). TGA was used to determine the thermal stability of clay in terms of weight loss. The sample was analyzed by TGA, PerkinElmer Thermal Analysis Diamond TG/DTA. The analysis was preceded under nitrogen atmosphere at gas flow rate of 100 mL/min. The sample was heated from 25°C to 300°C at a constant rate of 10°C/min and then cooled naturally.

Fourier Transform Infrared Spectroscopy (FTIR). FTIR was used to identify specific structural characteristics (e.g., functional group or molecular structure) of nanoclay using Nicolet 6700 FTIR.

2.5.2. Characterization of Nanocomposites

Small Angle X-Ray Diffraction Analysis (SAXRD). SAXRD was used to identify the sample by comparison with reference sample and to determine the interlayer spacing of nanoclay in polymer matrix. XRD patterns of polyethylene/clay nanocomposites were observed using Bruker AXS Model D8 Discover X-ray diffractometer with VANTEC-1 Detector (Super Speed Detector) 46 connected to a personal computer for full control of the XRD analyzer. The observation was preceded by using Cu radiation measurement, 2θ range of detection is 1–10 degree, and increment is 0.02 degree/step.

Thermal Gravimetric Analysis (TGA). TGA was used to determine the thermal stability in terms of weight percent in the sample as a function of temperature. PE/clay nanocomposites were analyzed by TGA, PerkinElmer Thermal Analysis Diamond TG/DTA. The analysis was performed under nitrogen atmosphere at gas flow rate of 100 mL/min. The sample was heated from 50°C to 600°C at a constant rate of 10°C/min and then cooled naturally.

Differential Scanning Calorimetry (DSC). The melting temperature (T_m) was determined by a Perkin-Elmer diamond DSC. The analysis was proceeded at the heating rate of 20°C/min in the temperature range of 50–150°C under N₂ atmosphere. The heating cycle was run twice. In the first scan, the samples were heated and then cooled to room temperature. In the second scan, the samples were reheated at the same rate, but only the results of the second scan were reported because the first scan was influenced by the mechanical and thermal history of the samples.

Nuclear Magnetic Resonance (¹³C NMR). ¹³C NMR was used to evaluate the percent insertion of comonomer in the copolymer. For sample preparation, LLDPE/clay nanocomposite was dissolved in the mixture of 1,2,4-trichlorobenzene and chloroform-d (internal locking solvent) and then heated until it became a clear solution. The ¹³C NMR spectra were recorded at 110°C using JEOL JNM-A500 operating at 125 MHz.

Scanning Electron Microscopy (SEM). SEM was used to observe the morphology of polymer nanocomposites. The sample was analyzed by JEOL JSM-6400 scanning electron microscopy. The nanocomposite samples were mounted on a stub with double-sided adhesive tape and coated with a thin layer of gold prior to observation.

3. Results and Discussion

3.1. Characterization of Nanoclay

3.1.1. Size and Composition. Figure 1 shows the XRD patterns of nanoclay. The sizes of nanoclay were investigated by X-ray diffraction (XRD). From Debye-Scherrer formula [6], it was confirmed that the average crystallite sizes of clay A and clay B are ca. 4 and 7 nm (using the XRD peak at 22°), respectively.

Both clay XRD patterns present the peaks in the positions (2θ) of 20, 22, 26.5, and 36°, corresponding to montmorillonite (MMT) crystalline structure [11]. The position at 10.1° corresponds to illite clay mineral, which is a phyllosilicate or layered aluminosilicate. This indicates that these nanoclays are mixed-layer montmorillonite/illite, which is composed of two discrete species: one is montmorillonite having low interlayer charge with hydrated interlayers by at least two layers of water molecules; the second species is illite with dehydrated interlayers.

3.1.2. Functional Group. The functional groups of two types of nanoclay were compared by FTIR spectra. The FTIR spectra are shown in Figure 2. It was found that the wavenumbers of obtained peaks are not different and the absorbances are also rather equal. FTIR spectra show the main peaks at 1000, 2850, and 2900 cm⁻¹ wavenumbers, which are corresponding to alkene (=C–H bending), CH stretching vibrations (CH₂), and alkane (C–H stretch), respectively, [12]. The peak between 3,300 and 3,500 cm⁻¹ was considered as amine (N–H stretch) [12]. The absorbance peak of clay A is lower than clay B. This indicates that amine compound in clay A is less than clay B. It may be due to the different amounts of amine salts

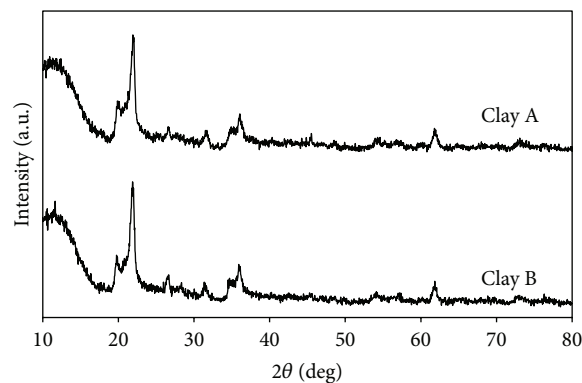


FIGURE 1: XRD patterns of nanoclay.

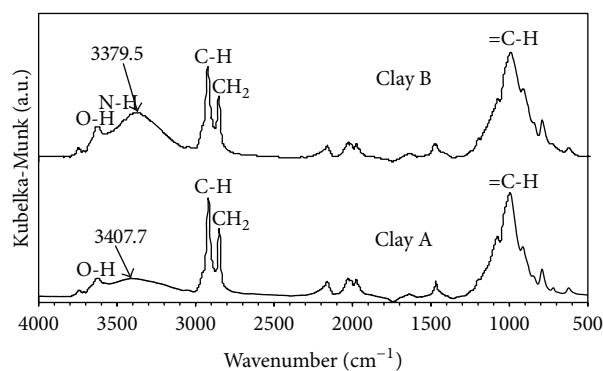


FIGURE 2: FTIR spectra of clay A and clay B.

in the surface of the clay. Moreover, it was possible that clay A and clay B were modified by the different kinds of amine salts, which include primary, secondary, or tertiary amine salt.

3.1.3. Thermal Stability. Thermal stability of nanoclay in nitrogen atmosphere can be observed from Figure 3, which indicates that clay A is more stable than clay B at a temperature lower 300°C. The thermal stabilities were evaluated in terms of 10% weight-loss temperatures (T_{d10}). T_{d10} of clay A is higher than clay B, which are 273 and 227°C, respectively. This difference in thermal stability was due to different compositions of these nanoclays. In general, the unmodified clay (such as Na⁺-Montmorillonite) has weight loss at ca. 100°C due to the presence of moisture in the interlayer between clay platelets. However, for clay A, the weight loss at ca. 100°C was not observed. This indicates that the surface of the clay platelets had been modified with an organic modifier (alkyl ammonium salt), conveying hydrophobic properties to the hydrophilic clay. From 200°C, the weight loss was observed on clay A due to the decomposition of the alkyl amine salt [13]. In clay B, the first weight loss was observed at 90°C. It is attributed to the decomposition of the remaining moisture in this clay. Above 200°C, clay B exhibited lower stability than clay A. The alteration of thermal stability may be derived from the various kinds and amounts of amine salts between the two clays.

TABLE I: Catalytic activities of polymerization systems with various fillers.

Run	Polymer	Amount of clay (wt%)		Yield ^a (g)	Activity ^b (kg pol./mol Zr·h)
		Clay A	Clay B		
1		—	—	1.3643	17,588
2		5	—	0.6622	12,851
3		10	—	0.7083	8,730
4	PE	20	—	0.5894	6,869
5		40	—	0	0
6		—	10	0.7937	8,007
7		—	20	0.2906	5,440
8		—	40	0	0
9		—	—	1.3087	35,534
10	LLDPE	5	—	1.1045	20,036
11		10	—	1.2241	12,143
12		20	—	0.3998	5,578
13		40	—	0	0

^aThe polymer yield was limited by the amount of ethylene fed (0.018 mol). The molar ratio of ethylene: comonomer was 2:1.

^bActivities were measured at polymerization temperature of 70°C, [ethylene] = 0.018 mol, $[Al]_{MAO}/[Zr]_{cat} = 1135$ in toluene with total volume = 30 mL, $[Zr]_{cat} = 5 \times 10^{-5}$ molar and mixing time of MAO and nanoclay was 30 min.

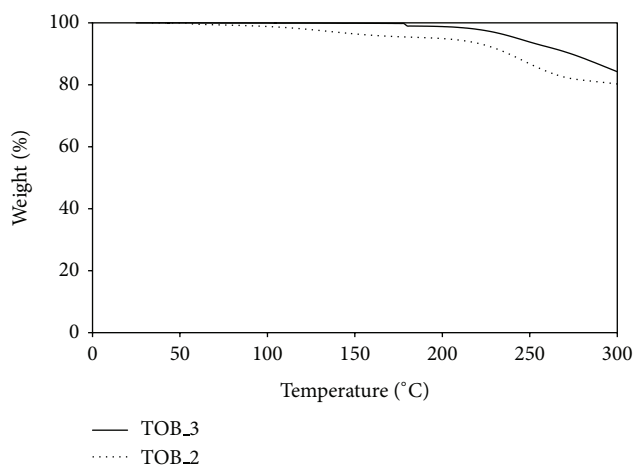


FIGURE 3: TGA curves of nanoclays (clay A: TOB.3 and clay B: TOB.2).

3.2. Ethylene Polymerization. The effect of the types of nanoclay on the activity of metallocene catalyst as shown in Table I indicates that the polymerization system with clay A exhibits higher catalytic activity than that with clay B at the same loading. This is consistent with the higher amount of amine group in clay B, which may deactivate zirconocene catalyst [10, 14]. Therefore, clay A is more appropriate to use as nanofiller for catalytic aspect. It is also observed that the catalytic activity of the homogeneous systems (runs 1 and 9) is higher than that of the heterogeneous (with clays) systems (runs 2–8 and 10–13). The reduction of the catalytic activity for the heterogeneous systems can be attributed to (1) the generation of catalyst active sites with lower propagation rates due to interactions with the clay surface, and (2) restrictions of the monomer access to the catalyst active sites due to the presence of the clays, hindering the chain propagation

[15]. In addition, the catalytic activity tended to decrease with the increase of the nanoclay content. This is because the drawbacks of the heterogeneous system as mentioned above were more pronounced when the higher amounts of nanoclay were present in the systems. The deactivating effect of the amine group on the zirconocene catalyst is also another reason for the decrease of catalytic activity. When increasing the amount of nanoclay to 40 wt%, it did not even produce polyethylene due to the more adverse effect from the nanoclays.

3.3. Characterization of Nanocomposites. It was because clay A provided the higher catalytic activity than clay B, thus it was more appropriate to be used as the catalytic filler. Therefore, in this characterization of nanocomposites, only clay A-filled nanocomposites were investigated and compared with the pure polymers.

3.3.1. Dispersion of Nanoclay. The small angle X-ray diffraction (SAXRD) patterns of nanoclay (clay A), pure PE, and PE/clay nanocomposites are shown in Figure 4. The SAXRD patterns for clay A provide diffraction peaks at $2\theta = 2.3$ and 4.7° , whereas the pure PE did not exhibit the diffraction peak at $2\theta = 1-10^\circ$ range. The diffraction peaks of all nanocomposites were also not observed. The peaks at about $2\theta = 2.3$ and 4.7° of clay were not in the nanocomposites suggesting that high dispersion of nanoclay throughout polyethylene matrix was obtained [16]. This exfoliated degree dispersion of nanoclay may be due to direct mixing process. The methylaluminoxane (MAO) added during the clay treatment step is expected to react with hydroxyl group on clay surface. After that, the zirconocene catalyst added during catalyst supported step was intercalated between the clay platelets, where the zirconocene catalyst was reacted with MAO-treated clay and modifier, creating covalent bond that helps to avoid catalyst leaching during the polymerization. Thus, it is the cause

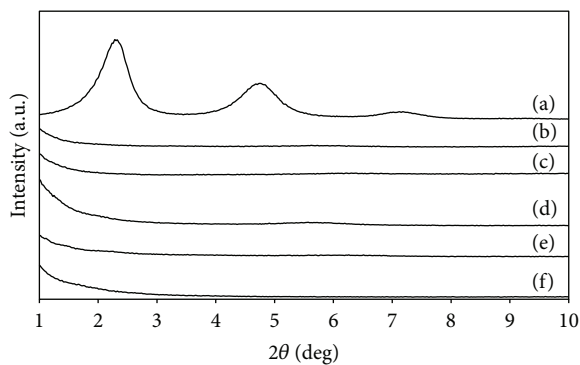


FIGURE 4: SAXRD patterns of (a) clay A, (b) LLDPE/clay 10 wt%, (c) LLDPE/clay 5 wt%, (d) PE/clay 10 wt%, (e) PE/clay 5 wt%, and (f) pure PE.

of well dispersion of nanoclay in the polyethylene matrix [17]. Exfoliation became possible through a strong interaction between the polyethylene chains and the clay surface [18].

3.3.2. Thermal Stability. Figure 5 shows TGA and DTG curves of pure PE and PE/clay nanocomposites. It is used to describe thermal stability of PE/clay nanocomposites. At temperature range between 200 and 350°C, PE/clay nanocomposite degraded slower than pure PE observed from the lower weight loss percentage, whereas the nanocomposite with 20 wt% of clay loading exhibited faster degradation. The weight loss at this temperature range is related mainly to the organic surface modifier degradation and also the degradation of remained MAO that cannot participate in the polymerizations [9]. In effect, the nanocomposite with 20 wt% of clay loading, which naturally has the highest content of the organic surface modifiers among all the samples and also has the highest content of the remained inactive MAO due to the lowest catalytic activity, thus degraded fastest in this temperature range. For the nanocomposites with 5% and 10 wt% of clay loadings, they degraded slower than the pure polymer due to the major effect of barrier properties induced by the nanoclays that hindered heat transfer throughout the nanocomposites [19]. At the temperature above 400°C, the weight loss of the polymer contributes to polymeric chain degradation. It was found that the nanocomposite with 5 wt% of clay loading still exhibited better thermal stability than the pure polymer and other nanocomposite samples. The lower thermal stabilities of the nanocomposites with the higher loadings (10 and 20 wt%) compared to the pure polymer are attributed to the presence of more acidic sites originating from the Hoffman degradation of the organic surface modifiers, which catalyze the polymer chain degradation [20, 21]. Therefore, it can be concluded from the TGA result that the introduction of clay into the polymers not exceeding 5 wt% can enhance their thermal stability, but the excess of clay (from 10 wt%) can reduce the thermal stability of the polymer. For DTG curve, the maximum decomposition temperatures were observed. The maximum decomposition temperatures of pure PE, PE/clay 5, PE/clay 10, and PE/clay 20 are 463, 481, 452, and 449°C,

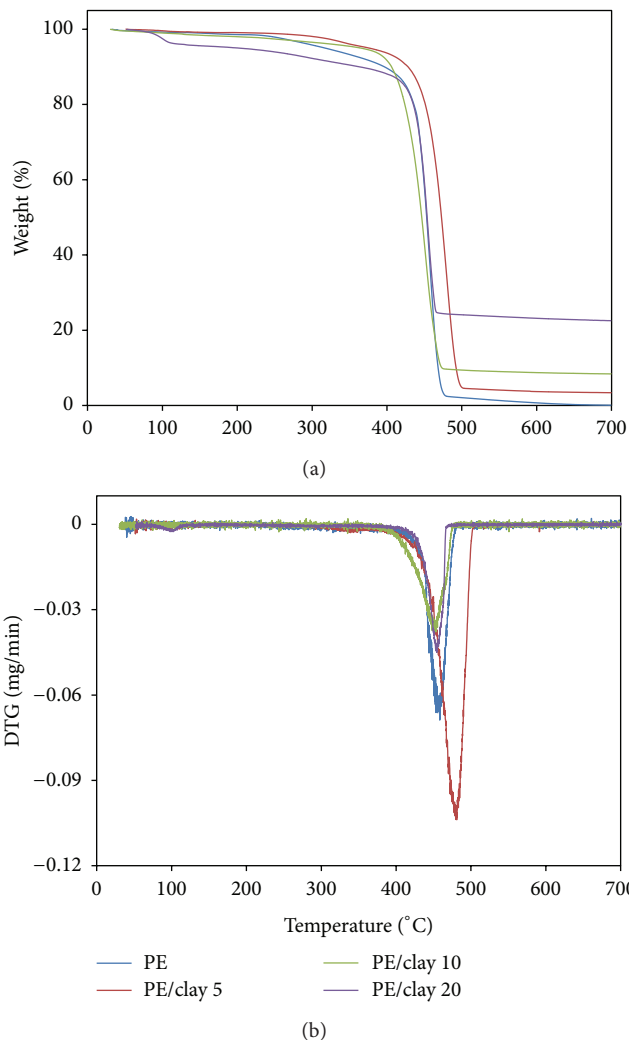


FIGURE 5: TGA and DTG curves of PE and PE/clay nanocomposites.

respectively. It can be observed that from 10 wt% to 20 wt% of clay content, the maximum decomposition temperatures of the nanocomposites decreased with increasing the clay content. This result is attributed to an increase of the acidic sites with increasing the organic surface modifiers (from clays), which accelerated the polymer degradation.

The thermal properties of LLDPE and its nanocomposites investigated by TGA and DTG are shown in Figure 6. It was found that the maximum decomposition temperatures of pure LLDPE, LLDPE/clay 5, LLDPE/clay 10, and LLDPE/clay 20 are 463, 463, 465, and 442°C, respectively. This thermal behavior of LLDPE slightly differed from that of PE probably due to the difference in molecular structure and crystallinity between two polymers, then being affected by the clay differently.

3.3.3. Crystallization Behavior. Table 2 shows the melting temperature, crystallinity, and 1-hexene insertion (obtained from ^{13}C NMR spectrum as shown in Figure 7) of pure PE, pure LLDPE, and the nanocomposites. It can be observed that

TABLE 2: Melting temperature, crystallinity, and 1-hexene (comonomer) insertion of the polymers and polymer nanocomposites.

Run	Polymer	Amount of clay A (wt%)	T_m^a ($^{\circ}\text{C}$)	X_c^b (%)	1-Hexene insertion ^c (%)
1		—	134	51	—
2	PE	5	134	57	—
3		10	132	51	—
4		20	132	44	—
9		—	114	3	32.2
10	LLDPE	5	n/a ^d	n/a	29.6
11		10	132	28	15.8
12		20	108	23	5.2

^aMelting temperature (T_m) was obtained from DSC measurement.

^bCrystallinity (X_c) was calculated based on DSC results.

^c1-Hexene insertion was obtained from ^{13}C -NMR spectrum equalling to [HHH] + [HHE] + [EHE].

^dNot detected.

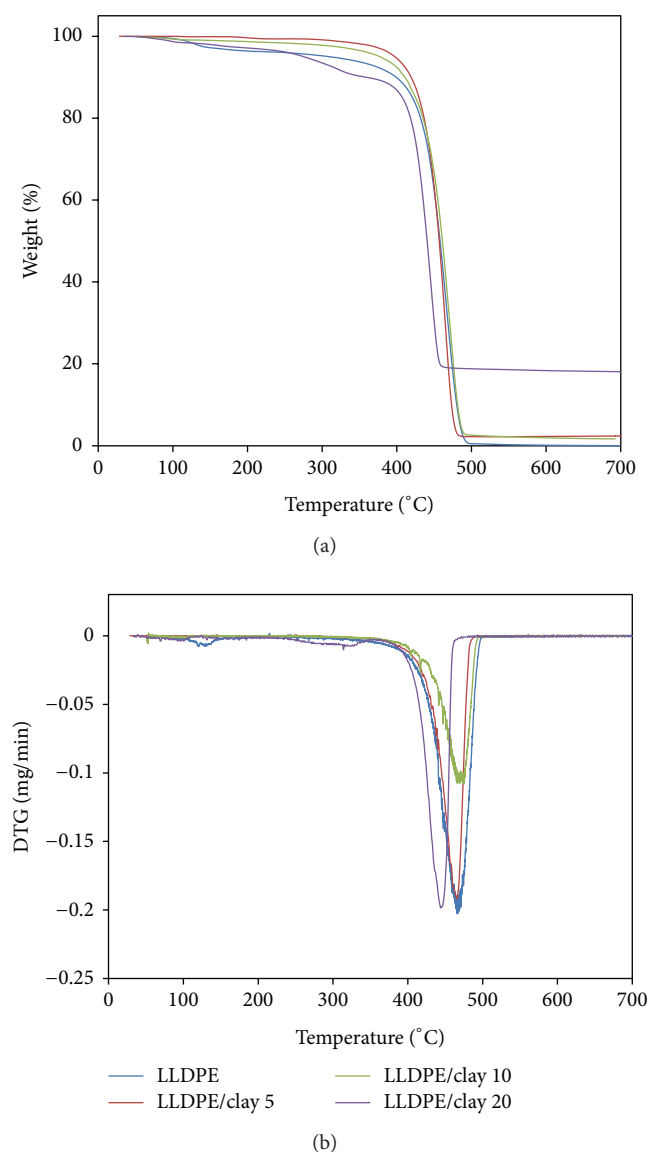


FIGURE 6: TGA and DTG curves of LLDPE and LLDPE/clay nanocomposites.

there was no significant change in the melting temperature of PE with the addition of nanoclay in homopolymerization system. However, it is seen that PE/clay nanocomposites with various clay loadings are different in the crystallinity. Adding 5 wt% of clay in the composite presents an increase in crystallinity. This suggests that small amount of clay acting as heterophase crystal nucleation agent in the polymer matrix [18]. However, the crystallinities of PE/clay nanocomposites decreased by increasing the amounts of nanoclay to 10 and 20 wt%. This may be due to large amounts of clay particles locating themselves in the interlamellar spaces, leaving a little room for additional crystallization. Thus, clay particle may hinder the formation of crystalline phase of PE and present a decrease in crystallinity [18]. For the copolymerization system in which 1-hexene was used as a comonomer, no melting temperature was found for LLDPE with 5 wt% of clay (run 9). It may be due to too much insertion of 1-hexene comonomer (over 30%), which poses the large molecular structure, and also the effect of clay that prevents the crystallization process inside the polymer. This contrasts with the pure LLDPE (run 8) which only the high comonomer insertion occurred without the presence of clay. Therefore, its crystallinity still appeared. The melting temperatures and the crystallinities were observed in the case of LLDPE with 10 and 20 wt% of clay (runs 11 and 12). It may be due to a decrease of comonomer insertion resulting from the higher content of clay that brought the crystallinity back to the nanocomposites. The higher content of the clay in the polymerization system could lead to less space for monomer (ethylene) or comonomer (1-hexene) attacking into the catalyst active sites. On account of this phenomenon, 1-hexene molecules which are larger than ethylene molecules then have the lower ability to attack the active sites when the clay content is higher. Therefore, the insertion of the 1-hexene decreased by increasing the amount of the clay.

3.3.4. *Morphology.* The SEM micrographs of the PE and PE/clay nanocomposites are shown in Figure 8. It can be seen that no agglomerated particles leaching out from the polymer matrix were clearly observed. This suggests good distribution

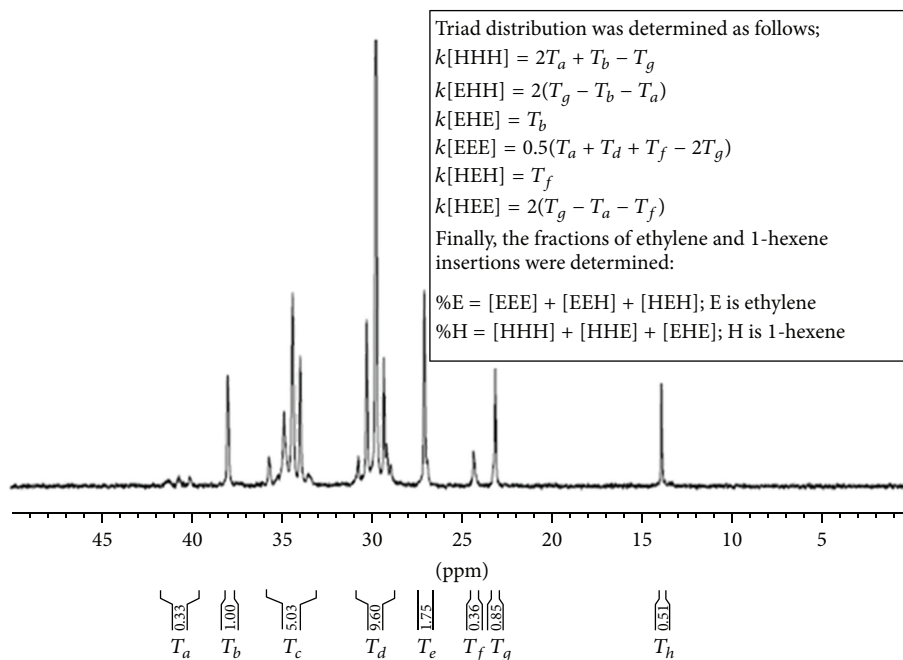
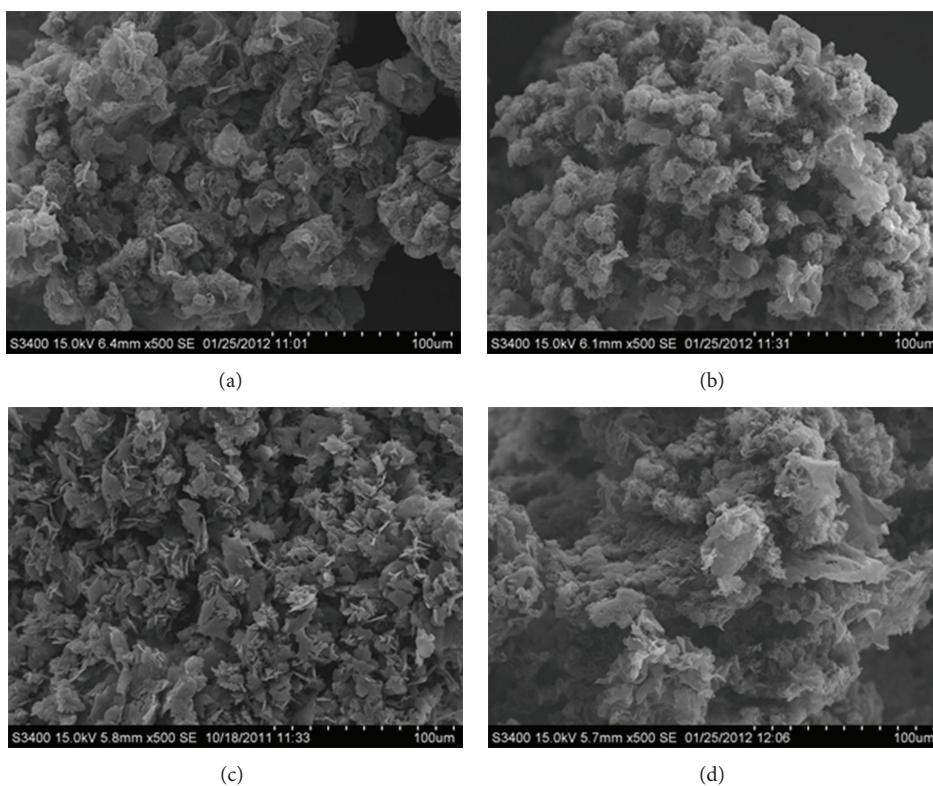
FIGURE 7: A typical ^{13}C NMR spectrum of LLDPE.

FIGURE 8: SEM images of PE samples. (a) PE, (b) PE/clay 5, (c) PE/clay 10, and (d) PE/clay 20.

of the clays, which reduces a tendency for the clays to agglomerate. In addition, the strong interaction between the clay surface and the polymer matrix may help reduce the leaching of the clays. These advantages would come from

the *in situ* polymerization, in which the catalyst covalently bound between the clay layers becomes the reaction center during the polymerization and was attacked and linked with the monomer; therefore, the strong interaction between

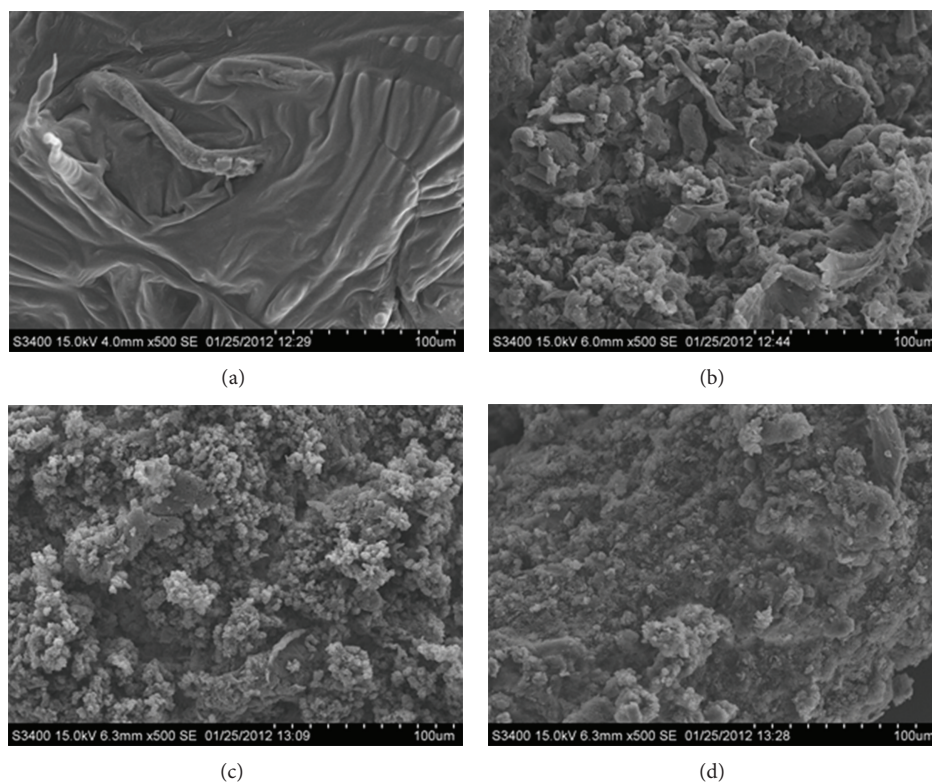


FIGURE 9: SEM images of LLDPE samples. (a) LLDPE, (b) LLDPE/clay 5, (c) LLDPE/clay 10, and (d) LLDPE/clay 20.

the clay and the polymer occurred. Moreover, when the polymer had been propagating it exfoliated the clay layers all over the polymer matrix, with the good distribution of the clays being obtained [22]. The morphologies of all PE/clay nanocomposites did not change upon various clay contents. This suggests that the good distribution of clay still occurs even the high clay content. From Figure 9, it is observed that the morphology of pure LLDPE differed considerably from the entire LLDPE/clay nanocomposites. The presence of clays improved greatly the morphology of LLDPE by providing the pellet-like structure, which is required for the polymer processing. The variation of clay content did not significantly affect the morphologies of LLDPE/clay nanocomposites.

4. Conclusions

The *in situ* polymerization in which catalyst was first immobilized onto the nanoclay, and then brought the nanoclays/catalyst into the polymerization process, appeared to be a good method for producing polymer nanocomposites with an excellent distribution of the nanoclays inside the polymer matrix. The distribution of the nanoclays can be proven by X-ray diffraction analysis (XRD), which no peak indicating to the nanoclays was observed suggesting high dispersion of nanoclay throughout the polymer matrix. Both clay A and clay B can improve thermal stability for the host polymers. However, clay B provided the lower catalytic activity to the polymerization system than clay A due to the higher amount of amine group, which could deactivate

the catalyst. The clay content adversely affected the catalytic activity for both PE and LLDPE and also affected the comonomer insertion in the case of LLPDE.

Acknowledgment

The authors thank “The Ratchadaphiseksomphot Endowment Fund of Chulalongkorn University (RES5605300086-AM)”.

References

- [1] O. G. Piringer and A. L. Baner, *Plastic Packaging: Interactions with Food and Pharmaceuticals*, Wiley-VCH, 2nd edition, 2008.
- [2] L. Chen, R. Ozisik, and L. S. Schadler, “The influence of carbon nanotube aspect ratio on the foam morphology of MWNT/PMMA nanocomposite foams,” *Polymer*, vol. 51, no. 11, pp. 2368–2375, 2010.
- [3] D. Zhang and T. Cui, “Tunable mechanical properties of layer-by-layer self-assembled carbon nanotube/polymer nanocomposite membranes for M/NEMS,” *Sensors and Actuators A*, vol. 185, pp. 101–108, 2012.
- [4] S. Barus, M. Zanetti, M. Lazzari, and L. Costa, “Preparation of polymeric hybrid nanocomposites based on PE and nanosilica,” *Polymer*, vol. 50, no. 12, pp. 2595–2600, 2009.
- [5] X. Huang, Z. Ma, Y. Wang, P. Jiang, Y. Yin, and Z. Li, “Polyethylene/aluminum nanocomposites: improvement of dielectric strength by nanoparticle surface modification,” *Journal of Applied Polymer Science*, vol. 113, no. 6, pp. 3577–3584, 2009.

- [6] C. Zhao, H. Qin, F. Gong, M. Feng, S. Zhang, and M. Yang, "Mechanical, thermal and flammability properties of polyethylene/clay nanocomposites," *Polymer Degradation and Stability*, vol. 87, no. 1, pp. 183–189, 2005.
- [7] G. Huang, B. Zhu, and H. Shi, "Combination effect of organics-modified montmorillonite with intumescent flame retardants on thermal stability and fire behavior of polyethylene nanocomposites," *Journal of Applied Polymer Science*, vol. 121, no. 3, pp. 1285–1291, 2011.
- [8] P. Meneghetti and S. Qutubuddin, "Synthesis, thermal properties and applications of polymer-clay nanocomposites," *Thermochimica Acta*, vol. 442, no. 1-2, pp. 74–77, 2006.
- [9] S. Hakim, M. Safajou-Jahankhanemlou, and M. Zeynali, "Polyethylene nanocomposite prepared by a metallocene catalyst supported on MMT using a new pretreatment method," *Journal of Polymer Research*, vol. 20, no. 5, pp. 1–10, 2013.
- [10] P. Zapata, R. Quijada, C. Covarrubias, E. Moncada, and J. Retuert, "Catalytic activity during the preparation of PE/clay nanocomposites by in situ polymerization with metallocene catalysts," *Journal of Applied Polymer Science*, vol. 113, no. 4, pp. 2368–2377, 2009.
- [11] S. O. Vilela, M. A. Soto-Oviedo, A. P. F. Albers, and R. Faez, "Polyaniline and mineral clay-based conductive composites," *Materials Research*, vol. 10, no. 3, pp. 297–300, 2007.
- [12] R. M. Silverstein, G. C. Bassler, and T. C. Morrill, *Spectrometric Identification of Organic Compounds*, John Wiley and Sons, New York, NY, USA, 1981.
- [13] F. Dietsche, Y. Thomann, R. Thomann, and R. Mülhaupt, "Translucent acrylic nanocomposites containing anisotropic laminated nanoparticles derived from intercalated layered silicates," *Journal of Applied Polymer Science*, vol. 75, no. 3, pp. 396–405, 2000.
- [14] S. K. Ackerman, A. K. Agapiou, M. L. DeChellis, and D. M. LaBorde, *Process for Deactivating Ziegler-Natta and Metallocene Catalysts*, Exxon Chemical Patents, 1994.
- [15] F. Silveira, G. P. Pires, C. F. Petry et al., "Effect of the silica texture on grafting metallocene catalysts," *Journal of Molecular Catalysis A*, vol. 265, no. 1-2, pp. 167–176, 2007.
- [16] Y. H. Lee, T. Kuboki, C. B. Park, M. Sain, and M. Kontopoulou, "The effects of clay dispersion on the mechanical, physical, and flame-retarding properties of wood fiber/polyethylene/clay nanocomposites," *Journal of Applied Polymer Science*, vol. 118, no. 1, pp. 452–461, 2010.
- [17] Y. Choi and J. B. P. Soares, "Supported single-site catalysts for slurry and gas-phase olefin polymerisation," *Canadian Journal of Chemical Engineering*, vol. 90, no. 3, pp. 646–671, 2012.
- [18] X. Wang, T. T. Fangfang, X. Gi et al., "Enhanced exfoliation of organoclay in partially end-Functionalized non-polar polymer," *Macromolecular Materials and Engineering*, vol. 294, no. 3, pp. 190–195, 2009.
- [19] S. M. Lomakin, L. A. Novokshonova, P. N. Brevnov, and A. N. Shchegolikhin, "Thermal properties of polyethylene/montmorillonite nanocomposites prepared by intercalative polymerization," *Journal of Materials Science*, vol. 43, no. 4, pp. 1340–1353, 2008.
- [20] M. Zanetti, P. Bracco, and L. Costa, "Thermal degradation behaviour of PE/clay nanocomposites," *Polymer Degradation and Stability*, vol. 85, no. 1, pp. 657–665, 2004.
- [21] G. Leone, F. Bertini, M. Canetti, L. Boggioni, P. Stagnaro, and I. Tritto, "In situ polymerization of ethylene using metallocene catalysts: effect of clay pretreatment on the properties of highly filled polyethylene nanocomposites," *Journal of Polymer Science A*, vol. 46, no. 16, pp. 5390–5403, 2008.
- [22] S.-Y. A. Shin, L. C. Simon, J. B. P. Soares, and G. Scholz, "Polyethylene-clay hybrid nanocomposites: in situ polymerization using bifunctional organic modifiers," *Polymer*, vol. 44, no. 18, pp. 5317–5321, 2003.

Research Article

Effects of Chitosan Alkali Pretreatment on the Preparation of Electrospun PCL/Chitosan Blend Nanofibrous Scaffolds for Tissue Engineering Application

Fatemeh Roozbahani,¹ Naznin Sultana,¹ Ahmad Fauzi Ismail,² and Hamed Noupavar³

¹ Faculty of Biosciences and Medical Engineering, Universiti Teknologi Malaysia (UTM), 81310 Skudai, Johor Bahru, Johor, Malaysia

² Advanced Membrane Technology Center, Universiti Teknologi Malaysia (UTM), 81310 Johor Bahru, Johor, Malaysia

³ Faculty of Chemical Engineering, Department of Polymer, Universiti Teknologi Malaysia (UTM), 81310 Johor Bahru, Johor, Malaysia

Correspondence should be addressed to Naznin Sultana; naznin@biomedical.utm.my

Received 19 March 2013; Revised 12 July 2013; Accepted 23 July 2013

Academic Editor: Jin Zhang

Copyright © 2013 Fatemeh Roozbahani et al. This is an open access article distributed under the Creative Commons Attribution License, which permits unrestricted use, distribution, and reproduction in any medium, provided the original work is properly cited.

Recently, nanofibrous scaffolds have been used in the field of biomedical engineering as wound dressings, tissue engineering scaffolds, and drug delivery applications. The electrospun nanofibrous scaffolds can be used as carriers for several types of drugs, genes, and growth factors. PCL is one of the most commonly applied synthetic polymers for medical use because of its biocompatibility and slow biodegradability. PCL is hydrophobic and has no cell recognition sites on its structure. Electrospinning of chitosan and PCL blend was investigated in formic acid/acetic acid as the solvent with different PCL/chitosan ratios. High viscosity of chitosan solutions makes difficulties in the electrospinning process. Strong hydrogen bonds in a 3D network in acidic condition prevent the movement of polymeric chains exposed to the electrical field. Consequently, the amount of chitosan in PCL/chitosan blend was limited and more challenging when the concentration of PCL increases. The treatment of chitosan in alkali condition under high temperature reduced its molecular weight. Longer treatment time further decreased the molecular weight of chitosan and hence its viscosity. Electrospinning of PCL/chitosan blend was possible at higher chitosan ratio, and SEM images showed a decrease in fiber diameter and narrower distribution with increase in the chitosan ratio.

1. Introduction

Electrospinning has received widespread attention as an easy and adaptable technique which leads to fabrication of fibers in nanometer size scale. Nanofibers provide remarkably high surface area for surface interchanges, a significantly improved interconnected pore architecture for diffusion and transportation of biological fluid, nutrient, and drugs for tissue engineering and drug delivery applications [1]. Utilizing electrospun fibers and nanofibrous meshes in tissue engineering applications often includes several considerations: selection of material, fiber orientation (aligned or random), porosity, and surface modification. Both natural and synthetic (biodegradable and nondegradable) materials as well as hybrid blends can be used depending on specified mechanical and biomimetic properties [2, 3]. Also by varying the processing and solution parameters, fiber orientation

and porosity/pore size of the electrospun scaffold can be controlled and optimized for each individual application.

In tissue engineering, the scaffold prepares a three-dimensional (3D) construct for cell attachment, proliferation, and formation of an extracellular matrix (ECM), as well as a carrier of growth factors or other biomolecular signals [4]. Scaffolds for tissue engineering should have good mechanical properties, suitable biodegradability, and most importantly good biocompatibility [4, 5]. Particularly, the surface properties of the material define the interactions between the cells and the material and, consequently, affect cell adhesion [6].

Poly(ϵ -caprolactone) (PCL) is one of the most commonly applied synthetic polymers for medical use because of its biocompatibility and slow biodegradability. PCL is hydrophobic, so presence of another component which embeds hydrophilicity and cell attachment is necessary in scaffold fabrication. Electrospinning of pure PCL has been

studied expansively [7–13]. Van der Schueren et al. [13] introduced an acetic acid/formic acid (AA/FA) solvent system for the electrospinning of PCL. Chitosan has been widely used in different biomedical areas because of its various advantages like biocompatibility, biodegradability, hydrophilicity, nonantigenicity, antimicrobial activity, nontoxicity, bioadherence, and cell affinity, which make it the ideal candidate for uses in a wide range of applications. It is a linear biopolymer and is usually obtained by alkaline deacetylation of chitin, the second most abundant biopolymer in nature after cellulose [14]. Chitosan is soluble in organic acids, such as aqueous acetic acid and formic acid. Free amino groups alongside chitosan chain become positively charged in acidic condition. Formation of hydrogen bonds in 3D network inhibits chain movement and limits the electrospinning. This drawback is a challenge for researchers and they have come up with different solutions which can be put in two categories: firstly using a suitable solvent system and secondly blending chitosan with another polymer. Ohkawa et al. [15] successfully prepared pure chitosan nanofibers using trifluoroacetic acid (TFA) as solvent. TFA can form salts with the amino groups of chitosan and thus prevent intermolecular interactions between chitosan chains in electrospinning process [16]. Spinnability of chitosan in aqueous solutions of acetic acid also has been investigated [15, 17, 18]. Formation of nanofibers and their morphology are highly influenced by acetic acid concentration and chitosan molecular weight and percentage.

The second polymer acts as an attenuating factor to limit the hydrogen bonds between chitosan chains and thus making the electrospinning of the polymer mixture possible. For example, polyethylene oxide (PEO) [19, 20] and polyvinyl alcohol (PVA) [21–23] have been investigated to improve the spinnability of chitosan. They reached to the point that the formation of nanofibers is highly dependent on the mass ratio of two polymers and higher mass ratio of chitosan is just possible in lower molecular weight of chitosan. Li and Hsieh [21] showed that the maximum ratio of PVA/chitosan was just 17/83 for chitosan with medium molecular weight; therefore, they introduced alkali pretreatment to decrease the molecular weight of chitosan. This also was approved by Homayoni et al. [23]; the molecular weight of chitosan decreased with an alkali pretreatment and led to good results in increasing the chitosan ratio in the blend.

Electrospinning of PCL/chitosan nanofibres has only recently been performed in some mix solvent systems [19, 24–29]. Recently, PCL/chitosan nanofiber was fabricated by electrospinning of PCL/chitosan polymeric blend in an acetic acid/formic acid (AA/FA) solvent mixture [28]. Electrospinning of solutions containing different polymer concentration performed at the voltage which assured a stable cone. Van der Schueren et al. [28] showed that adding chitosan below 13 wt% PCL improved the spinnability of PCL, but there is limitation in chitosan amount as for the least possible PCL this amount is around 1.8 wt% and for higher amount of PCL this amount decreases significantly. Limitation of electrospinning of PCL/chitosan blend is related to the polyelectrolyte properties of chitosan which limit its solubility in acidic solutions. For 8 wt% PCL the maximum wt% chitosan

is ≤ 1 . The limitations of solubility of medium molecular weight chitosan and chain entanglement problem in acidic condition affect its blend with PCL in new solvent system. So in this study alkali pretreatment of chitosan on spinnability, applicable portion of chitosan in PCL/Chitosan blend, and morphology of fabricated nanofibers were investigated.

2. Materials and Methods

2.1. Materials. Chitosan with medium molecular weight was purchased from Sigma-Aldrich. PCL with molecular weight 70,000–90,000 was supplied from same company. 98 v% formic acid was obtained from Sigma-Aldrich, 99.8 v% acetic acid from Merck, and sodium hydroxide pellet from QREC (Asia) SDN BHD Malaysia.

2.2. Methods

2.2.1. Reducing the Molecular Weight of Chitosan. To reduce the molecular weight of chitosan, the polymer powder was treated in a 50% NaOH with a chitosan/NaOH ratio of 1/25 (w/v) at the temperature of 95°C for 48 hours. Then, sample was strained and rinsed with distilled water, naturalized with acetic acid, and rinsed and dried at 60°C for 16 hours.

2.2.2. Preparation of the PCL/Chitosan Solutions. The electrospinning solutions were prepared by dissolving 2.5 wt% untreated chitosan, 7 wt% treated chitosan, and 8 wt% PCL individually in the solvent mixture acetic acid/formic acid (30/70). The solutions were magnetically stirred at room temperature for three hours, time needed for complete dissolution and finally mixed with PCL/chitosan solution ratio 30/70, 50/50 and 70/30 v/v% to study the effect of component ratio in electrospinning process.

2.2.3. Electrospinning. The polymer solution was pumped from a 5 mL syringe into a needle gauge 23. The voltage was in the range of 18–28 kV. Electrospinning was carried out at room temperature ($22 \pm 2^\circ\text{C}$) and at a relative humidity of $65 \pm 5\%$. The tip to collector distance was set at 12.5 cm. The flow rate was set at 0.5 mLh^{-1} and spinning was performed for 30 min.

2.2.4. Characterization. The morphology of electrospun PCL/chitosan fibers was observed with a scanning electron microscope (SEM). The diameter of the fiber was measured from the SEM micrographs using image analysis software (Image J, National Institutes of Health, USA).

Viscosities of solutions were measured by Brookfield Viscometer. FTIR spectroscopy was used to identify the changes of chitosan chemical bonds after treatment and to see the presence of component in blend. Samples with same dimensions were mixed with potassium bromide (KBr) to make pellets. FTIR spectra in the transmission mode were recorded using FTIR spectrometer (Perkin Elmer Series FTIR Spectrometer, USA), connected to a PC, and the data was analyzed by IR Solution software.

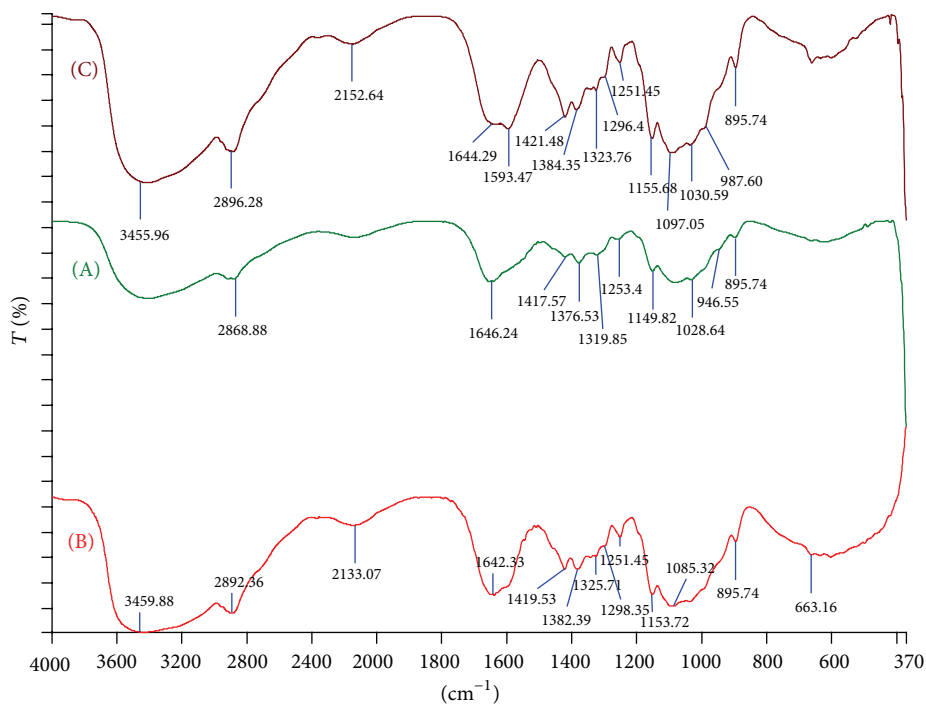


FIGURE 1: FTIR spectra of treated and untreated chitosan. (A) Untreated chitosan, (B) treated chitosan for 24 hours, and (C) treated chitosan for 48 hours.

3. Results and Discussions

3.1. Alkali Treatment. Alkali treatment decreases the molecular weight of chitosan by hydrolyzing the oxygen bonding the glucose amine groups. This effect on molecular weight depends on the treatment time. Chitosan treatment for 48 hours showed the best result regarding the spinnability of pure chitosan [30]. Hydrolyzing occurs more progressively by increasing treatment time. As after 5 hours molecular weight decreased from 1,094,804 to 1,043,791 and then by continuing the process for 16, 32, and 48 hours it changed to 645,023, 341,782, and finally 293,763 g/mol [12].

Alkali treatment does not change the chemical nature of chitosan. It was proved with Fourier transform infrared (FTIR). Spectra of untreated, 24 hours, and 48 hours treated chitosan polymers are demonstrated in Figure 1. All tree spectra show the same trend at distinctive wavelengths: C–OH groups at around 3450 cm^{-1} , N–H groups at 1650 cm^{-1} , and oxygen bonding at around 1150 cm^{-1} , 800 cm^{-1} . Physical changes because of molecular weight reduction lead to some small deviations in the positions of these peaks in the spectrum of the treated chitosan corroborate.

Figure 2 shows the FTIR spectra of pure PCL and PCL/chitosan blend nanofibers; the distinguished feature for PCL is the carbonyl stretching absorption at around 1730 cm^{-1} , and the spectra of PCL and chitosan blend in the form of untreated or even treated chitosan are very similar to the spectra of pure PCL except in some differences at around 3450 cm^{-1} , $1630\text{--}1670\text{ cm}^{-1}$, and 1100 cm^{-1} which contribute to chitosan groups as described in FTIR spectra of chitosan. In the area of 1700 cm^{-1} , there is a deeper absorbance in

PCL/chitosan both treated and untreated which is related to the hydrogen bond between carbonyl groups of PCL and chitosan. So this area is identically related to interaction between PCL and chitosan.

3.2. Electrospinning. PCL/chitosan blend nanofibres provide an excellent nanostructured material for biomedical use as their valuable properties are combined into one. The new solvent system leads to production of very fine and beadless nanofibres above 13 wt% PCL. The electrospinning of PCL/chitosan blends using 1,1,1,3,3,3-hexafluoro-2-propanol (HFIP), dimethylformamide/methylene chloride (DMF/MC), HFIP/TFA/DCM, acetone/formic acid, and acetic acid/formic acid were carried out before. Because of the toxicity and high price of most of these solvents, only the AA/FA solvent system seems applicable in PCL/chitosan electrospinning.

The main characteristic of a reproducible electrospinning process is a stable Taylor cone. Thus, voltage for all electrospinning processes has been adjusted for formation of utmost stable Taylor cone. Table 1 shows that for untreated chitosan, electrospinning of PCL/chitosan solution with the ratio of 70/30 was performed under 21 kV but increasing the portion of chitosan leads to polymer chain entanglement and inhibits nanofiber formation even at higher voltage. Alkali pretreatment decreases molecular weight of chitosan considerably; consequently, the viscosity of the same amounts of treated and untreated chitosan was not comparable, so for treated chitosan a solution of 7 wt% was prepared to make the result comparable with untreated chitosan concerning viscosities. Required voltage for polymeric blend with the ratio of 70/30

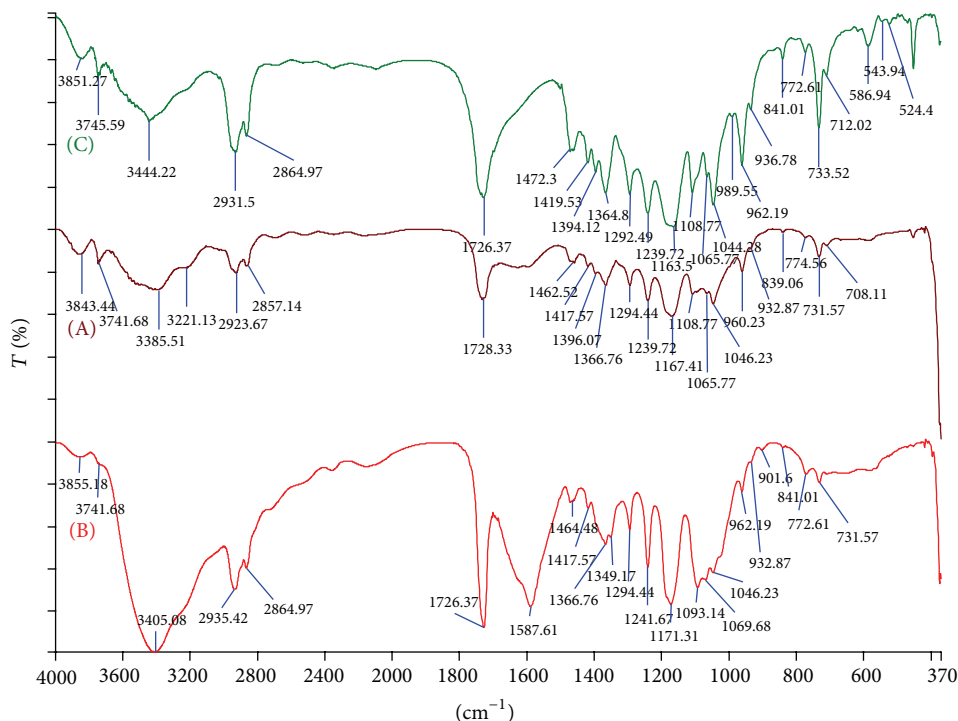


FIGURE 2: FTIR spectra of (A) 8 wt% PCL/2.5% untreated chitosan (70/30), (B) 8 wt% PCL/7% treated chitosan (70/30), and (C) pure PCL nanofibers.

TABLE 1: Electrospinning of PCL/chitosan blend and effect on required voltage.

PCL/chitosan blend	Applied voltage
8% PCL and 2.5% untreated chitosan (70/30)	21
8% PCL and 7% treated chitosan (70/30)	25
8% PCL and 2.5% untreated chitosan (50/50)	—
8% PCL and 7% treated chitosan (50/50)	28

PCL/treated chitosan was 25 kV, and for higher portion of chitosan with 50/50 of PCL/treated chitosan a higher voltage of 28 kV was needed.

Figures 3, 4, and 5 demonstrate the SEM images of nanofibers with the ratio of 70/30 PCL/untreated chitosan and 70/30, 50/50 PCL/treated chitosan, respectively. Table 2 shows the average diameter of nanofibers and the coefficient of variation of nanofibers. PCL/treated chitosan nanofibers with the ratio of 70/30 have lower average diameter of 205 nm compared to 356 nm for blend nanofiber fabricated by untreated chitosan. Both higher applied voltage and easier movement of polymer chains are the reasons for thinner fibers for treated chitosan and PCL blend. And additionally the narrower fiber distribution is due to the higher applied voltage. Increasing the portion of chitosan in PCL/treated chitosan sample caused fabricating thinner fibers with less variation which is related to higher required voltage for spinning in a stable condition.

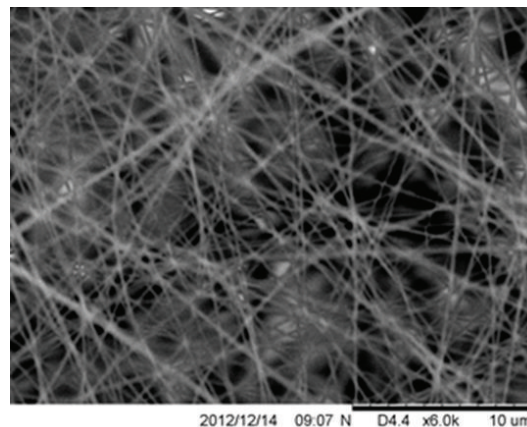


FIGURE 3: SEM image 8 wt% PCL/2.5% untreated chitosan (70/30).

4. Conclusions

In this study, the influence of the molecular weight of chitosan on spinnability of PCL/chitosan blends was investigated with an electrospinning technique. Alkali treatment has been introduced as a solution to decrease the molecular weight of medium molecular weight chitosan and, thus, reduction of hindering effect of positively charged amine group when spinning. This treatment does not change the chemical structure of chitosan. Treated chitosan in blend with PCL nanofibers caused fabrication of smaller diameter and narrower deviation compared to untreated chitosan. Smaller



FIGURE 4: SEM image 8 wt% PCL/7% treated chitosan (70/30).

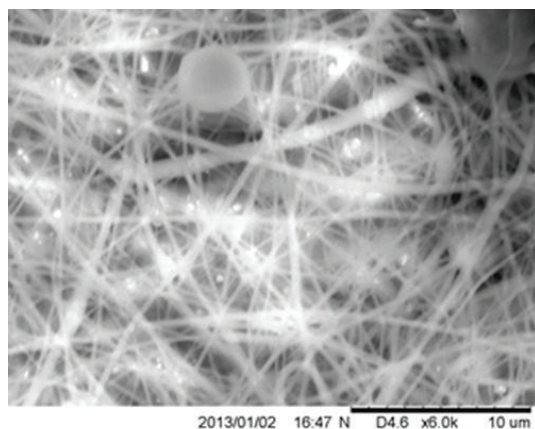


FIGURE 5: SEM image 8 wt% PCL/7% alkali treated chitosan (50/50).

TABLE 2: Average diameter, coefficient of variation, and surface porosity of chitosan blend.

PCL/chitosan blend	Average diameter (nm)	Coefficient of variation %
8% PCL and 2.5% untreated chitosan (70/30)	356.29	172.10
8% PCL and 7% treated chitosan (70/30)	204.81	83.92
8% PCL and 2.5% untreated chitosan (50/50)	—	—
8% PCL and 7% treated chitosan (50/50)	317.46	67.37

diameter is related to easier movement of chitosan polymer chains exposed to high voltage during electrospinning. Also increasing chitosan ratio in blend with PCL is possible to be considered for further studies in biomedical application.

Acknowledgments

F. Roozbahani would like to thank the University Teknologi Malaysia for International Doctoral Fellowship. The authors

also acknowledge MOHE, GUP Tier 1 Grants (Vot: 03H13, Vot: 05H07), FRGS (Vot: 4F126), MOHE, UTM, and RMC for financial support. Lab facilities of FBME are also acknowledged.

References

- [1] D. F. Stamatialis, B. J. Papenburg, M. Gironés et al., "Medical applications of membranes: drug delivery, artificial organs and tissue engineering," *Journal of Membrane Science*, vol. 308, no. 1-2, pp. 1-34, 2008.
- [2] N. Sultana and M. Wang, "PHBV/PLLA-based composite scaffolds fabricated using an emulsion freezing/freeze-drying technique for bone tissue engineering: surface modification and in vitro biological evaluation," *Biofabrication*, vol. 4, no. 1, Article ID 015003, 2012.
- [3] N. Sultana and T. H. Khan, "In vitro degradation of PHBV scaffolds and nHA/PHBV composite scaffolds containing hydroxyapatite nanoparticles for bone tissue engineering," *Journal of Nanomaterials*, vol. 2012, Article ID 190950, 12 pages, 2012.
- [4] I. Armentano, M. Dottori, E. Fortunati, S. Mattioli, and J. M. Kenny, "Biodegradable polymer matrix nanocomposites for tissue engineering: a review," *Polymer Degradation and Stability*, vol. 95, no. 11, pp. 2126-2146, 2010.
- [5] R. Ravichandran, S. Sundarajan, J. R. Venugopal, S. Mukherjee, and S. Ramakrishna, "Advances in polymeric systems for tissue engineering and biomedical applications," *Macromolecular Bioscience*, vol. 12, no. 3, pp. 286-311, 2012.
- [6] J. Dobkowski, R. Kołos, J. Kamiński, and H. M. Kowalczyńska, "Cell adhesion to polymeric surfaces: experimental study and simple theoretical approach," *Journal of Biomedical Materials Research*, vol. 47, no. 2, pp. 234-242, 1999.
- [7] H. Yoshimoto, Y. M. Shin, H. Terai, and J. P. Vacanti, "A biodegradable nanofiber scaffold by electrospinning and its potential for bone tissue engineering," *Biomaterials*, vol. 24, no. 12, pp. 2077-2082, 2003.
- [8] C. M. Vaz, S. van Tuijl, C. V. C. Bouten, and F. P. T. Baaijens, "Design of scaffolds for blood vessel tissue engineering using a multi-layering electrospinning technique," *Acta Biomaterialia*, vol. 1, no. 5, pp. 575-582, 2005.
- [9] F. Chen, C. N. Lee, and S. H. Teoh, "Nanofibrous modification on ultra-thin poly(ϵ -caprolactone) membrane via electrospinning," *Materials Science and Engineering C*, vol. 27, no. 2, pp. 325-332, 2007.
- [10] S.-C. Wong, A. Baji, and S. Leng, "Effect of fiber diameter on tensile properties of electrospun poly(ϵ -caprolactone)," *Polymer*, vol. 49, no. 21, pp. 4713-4722, 2008.
- [11] K. Ohkawa, H. Kim, K. Lee, and H. Yamamoto, "Electrospun non-woven fabrics of poly(ϵ -caprolactone) and their biodegradation by pure cultures of soil filamentous fungi," *Macromolecular Symposia*, vol. 216, no. 1, pp. 301-306, 2004.
- [12] A. K. Moghe, R. Hufenus, S. M. Hudson, and B. S. Gupta, "Effect of the addition of a fugitive salt on electrospinnability of poly(ϵ -caprolactone)," *Polymer*, vol. 50, no. 14, pp. 3311-3318, 2009.
- [13] L. van der Schueren, B. de Schoenmaker, Ö. I. Kalaoglu, and K. de Clerck, "An alternative solvent system for the steady state electrospinning of polycaprolactone," *European Polymer Journal*, vol. 47, no. 6, pp. 1256-1263, 2011.
- [14] C. Mahoney, M. B. McCullough, J. Sankar, and N. Bhattarai, "Nanofibrous structure of chitosan for biomedical applications," *Journal of Nanomedicine and Biotherapeutic Discovery*, vol. 2, no. 1, 2012.

- [15] K. Ohkawa, D. Cha, H. Kim, A. Nishida, and H. Yamamoto, "Electrospinning of chitosan," *Macromolecular Rapid Communications*, vol. 25, no. 18, pp. 1600–1605, 2004.
- [16] K. Sun and Z. H. Li, "Preparations, properties and applications of chitosan based nanofibers fabricated by electrospinning," *Express Polymer Letters*, vol. 5, no. 4, pp. 342–361, 2011.
- [17] X. Geng, O.-H. Kwon, and J. Jang, "Electrospinning of chitosan dissolved in concentrated acetic acid solution," *Biomaterials*, vol. 26, no. 27, pp. 5427–5432, 2005.
- [18] S. de Vrieze, P. Westbroek, T. van Camp, and L. van Langenhove, "Electrospinning of chitosan nanofibrous structures: feasibility study," *Journal of Materials Science*, vol. 42, no. 19, pp. 8029–8034, 2007.
- [19] N. Bhattarai, Z. Li, J. Gunn et al., "Natural-synthetic polyblend nanofibers for biomedical applications," *Advanced Materials*, vol. 21, no. 27, pp. 2792–2797, 2009.
- [20] K. Ziani, C. Henrist, C. Jérôme, A. Aqil, J. I. Maté, and R. Cloots, "Effect of nonionic surfactant and acidity on chitosan nanofibers with different molecular weights," *Carbohydrate Polymers*, vol. 83, no. 2, pp. 470–476, 2011.
- [21] L. Li and Y.-L. Hsieh, "Chitosan bicomponent nanofibers and nanoporous fibers," *Carbohydrate Research*, vol. 341, no. 3, pp. 374–381, 2006.
- [22] M. Ignatova, K. Starbova, N. Markova, N. Manolova, and I. Rashkov, "Electrospun nano-fibre mats with antibacterial properties from quaternised chitosan and poly(vinyl alcohol)," *Carbohydrate Research*, vol. 341, no. 12, pp. 2098–2107, 2006.
- [23] H. Homayoni, S. A. H. Ravandi, and M. Valizadeh, "Influence of the molecular weight of chitosan on the spinnability of chitosan/poly(vinyl alcohol) blend nanofibers," *Journal of Applied Polymer Science*, vol. 113, no. 4, pp. 2507–2513, 2009.
- [24] A. Cooper, N. Bhattarai, and M. Zhang, "Fabrication and cellular compatibility of aligned chitosan-PCL fibers for nerve tissue regeneration," *Carbohydrate Polymers*, vol. 85, no. 1, pp. 149–156, 2011.
- [25] S. Hong and G. Kim, "Fabrication of electrospun polycaprolactone biocomposites reinforced with chitosan for the proliferation of mesenchymal stem cells," *Carbohydrate Polymers*, vol. 83, no. 2, pp. 940–946, 2011.
- [26] M. P. Prabhakaran, J. R. Venugopal, T. T. Chyan et al., "Electrospun biocomposite nanofibrous scaffolds for neural tissue engineering," *Tissue Engineering A*, vol. 14, no. 11, pp. 1787–1797, 2008.
- [27] K. T. Shalumon, K. H. Anulekha, C. M. Girish, R. Prasanth, S. V. Nair, and R. Jayakumar, "Single step electrospinning of chitosan/poly(caprolactone) nanofibers using formic acid/acetone solvent mixture," *Carbohydrate Polymers*, vol. 80, no. 2, pp. 414–420, 2010.
- [28] L. van der Schueren, I. Steyaert, B. de Schoenmaker, and K. de Clerck, "Polycaprolactone/chitosan blend nanofibres electrospun from an acetic acid/formic acid solvent system," *Carbohydrate Polymers*, vol. 88, no. 4, pp. 1221–1226, 2012.
- [29] X. Yang, X. Chen, and H. Wang, "Acceleration of osteogenic differentiation of preosteoblastic cells by chitosan containing nanofibrous scaffolds," *Biomacromolecules*, vol. 10, no. 10, pp. 2772–2778, 2009.
- [30] H. Homayoni, S. A. H. Ravandi, and M. Valizadeh, "Electrospinning of chitosan nanofibers: processing optimization," *Carbohydrate Polymers*, vol. 77, no. 3, pp. 656–661, 2009.